Rijksuniversiteit Groningen

Master Thesis

Environmental influence of voids on dark matter halos

Author:
Jad Alexandru Mansour

Supervisor:
Rien van de Weygaert

Contents

1 Cosmic Voids **4**
- 1.1 Thesis objective . . . 4
- 1.2 Observations and numerical simulations . . . 5
- 1.3 Formation and Evolution . . . 7
- 1.4 Void Dynamics . . . 8
- 1.5 Tidal field influence on voids . . . 10
- 1.6 Void hierarchy . . . 12
- 1.7 Environmental influence of voids on dark matter halos and galaxies . . . 14

2 Cosmology and formation of the Large Scale Structure **16**
- 2.1 The concordance model: ΛCDM . . . 16
- 2.2 Emergence of the Large Scale Structure . . . 18
- 2.3 Linear Perturbation Theory . . . 19
- 2.4 Dark matter halos . . . 22
  - 2.4.1 Internal properties of Dark Matter Halos . . . 23
- 2.5 Cosmic Web . . . 26

3 Methodology **29**
- 3.1 Void identification: the Watershed Void Finder . . . 29
- 3.2 Cosmological N-body simulations . . . 34
  - 3.2.1 Governing principles . . . 34
  - 3.2.2 GADGET-2 . . . 34
  - 3.2.3 Gravitational algorithms . . . 35
  - 3.2.4 Simulation parameters . . . 37
- 3.3 Simulation processing: DTFE . . . 38
- 3.4 Simulation processing: Halo identification . . . 41
  - 3.4.1 Halo Finders . . . 42
  - 3.4.2 Rockstar Halo Finder . . . 43
  - 3.4.3 Identifying halos in voids: the convex hull algorithm . . . 45

4 Void population **50**
- 4.1 Void abundance . . . 50
- 4.2 Void center . . . 52
- 4.3 Voids sizes . . . 52
- 4.4 Voids shapes . . . 55
- 4.5 Density profiles . . . 58
- 4.6 Dynamics . . . 60

5 Void Halos **65**
5.1 Halo population 65
5.2 Halo Mass Function 65
5.3 Halo Shape and Spin 68

6 Conclusions **76**

Chapter 1

Cosmic Voids

The matter distribution at the large scale in the Universe resembles a cosmic web. In this web, voids - the underdense regions - represent an essential feature. To begin with, they are the most voluminous components of the cosmic web, occupying between 70% - 95% of the total volume (van de Weygaert and Platen 2011; Cautun, van de Weygaert, Jones, and Frenk 2014; P. Ganeshaiah Veena et al. 2019; Hellwing, Cautun, et al. 2021). They span sizes between 20-50 h^{-1} Mpc and behave as an organising element at the large scale (van de Weygaert 1991; Sheth and van de Weygaert 2004; Aragon-Calvo and Szalay 2013).

Furthermore, voids provide important clues regarding cosmological scenarios and their parameters. Such clues may be found in the velocity outflows (Dekel and Rees 1994) and the redshift space distorsions (Ryden and Melott 1996). The geometry and substructure of voids is dependent on cosmology, including dark energy (Park and Lee 2007; Platen, van de Weygaert, and Jones 2008; Bos et al. 2012; Lavaux and Wandelt 2012; Pollina et al. 2016; Verza et al. 2019). More recently, voids have also been used to constrain the neutrino mass (Villaescusa-Navarro et al. 2013; Massara et al. 2015; Schuster et al. 2019; Bayer et al. 2021; Kreisch et al. 2021).

In this work, we focus on the fact that voids offer a pristine and ideal environment in which the formation and evolution of dark matter halos and, subsequently, galaxies can be investigated (Hahn et al. 2007; Kreckel, Platen, Aragón-Calvo, et al. 2012; Ricciardelli et al. 2014; Metuki, Libeskind, and Hoffman 2016; Ganeshaiah Veena et al. 2018; Habouzit et al. 2020; Hellwing, Cautun, et al. 2021).

In this first chapter, we begin by stating the objective of the thesis followed by a short historical summary of void observations and simulations. Next, we focus on the formation and evolution of voids and their dynamics. Subsequently, we will show how voids interact with one another and with neighbouring structures, leading to a void hierarchy. Finally, we show what are the known effects of the void environment on the development of dark matter halos and galaxies.

1.1 Thesis objective

The main goal of this thesis is to investigate the environmental effects that voids have - through their underdense interiors - on the properties of dark matter halos. Concretely, we wish to first describe the void environment - size, shape, density and velocity profiles - and then to identify halos within voids. Once we have our sample of void halos, we wish to compare their properties (i.e abundance, halo mass function, spin and shape) with the properties of the overall halo population. We also investigate how these properties vary as a function of distance from the void boundaries. The differences that appear between the general halo population and the void halos should be linked with the properties of the void environment.

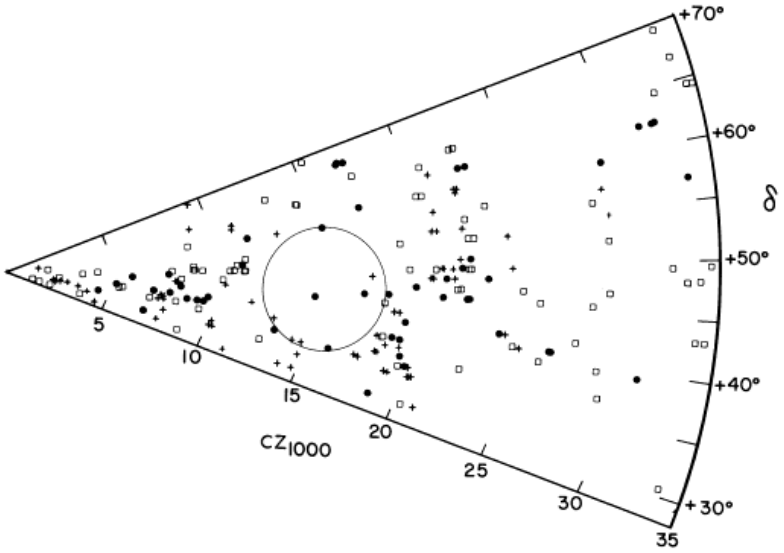

Figure 1.1: Galaxy distribution in the velocity-declination space. Circled area marks the Bootes void. Figure from (Kirshner et al. 1987).

To achieve this, we make use of a GADGET-2 simulation on which we apply the Watershed Void Finder algorithm in order to identify voids. For the identification of halos in the particle distribution, we use the ROCKSTAR Halo Finder algorithm while for the concrete identification of void halos, we make use of the convex hull.

1.2 Observations and numerical simulations

Gaps present in the galaxy distribution have been observed ever since the first galaxy surveys were developed (Chincarini and Rood 1975; Gregory and Thompson 1978; Einasto, Joeveer, and Saar 1980). Most notably is the discovery (Kirshner et al. 1981; Kirshner et al. 1987) of the Bootes void: a large, nearly empty region spanning a radius of ≈ 60 Mpc (Fig. 1.1). Following this discovery, the CfA (de Lapparent, Geller, and Huchra 1986) is the first survey to hint at the imposing presence that voids have at the large scale structure. Almost 20 years later, the redshift maps provided by the 2dFGRS and SDSS surveys have cemented the idea that voids are a fundamental and prominent component of the cosmic web (Colless et al. 2003; Hoyle and Vogeley 2004; Tegmark et al. 2004). An example map by the SDSS can be seen in Fig. 1.2. Voids of various sizes and shapes are visibly populating the galaxy distribution. At the time of this writing, the DESI survey (DESI Collaboration et al. 2016) has released their results which are expected to drastically increase the number of voids detected.

An indirect way in which voids have been identified is through observations of the peculiar velocity field in the large scale structure (Faber and Burstein 1988; Dekel 1994; Branchini et al. 1999). This field is a manifestation of matter being pushed from the underdense regions within voids towards the filaments and clusters situated at the voids boundaries. Remarkably, Tully et al. 2014 showed that the Local Void, an underdense region covering at least 23 Mpc, has a significant push on the Local Group. Concretely, they found that the void is responsible for $\approx 41\%$ of the group's peculiar velocity with respect to the CMB (see Fig. 1.3[1]).

The next step in investigating voids is keeping an account of their number and characteristics

[1] http://irfu.cea.fr/laniakea

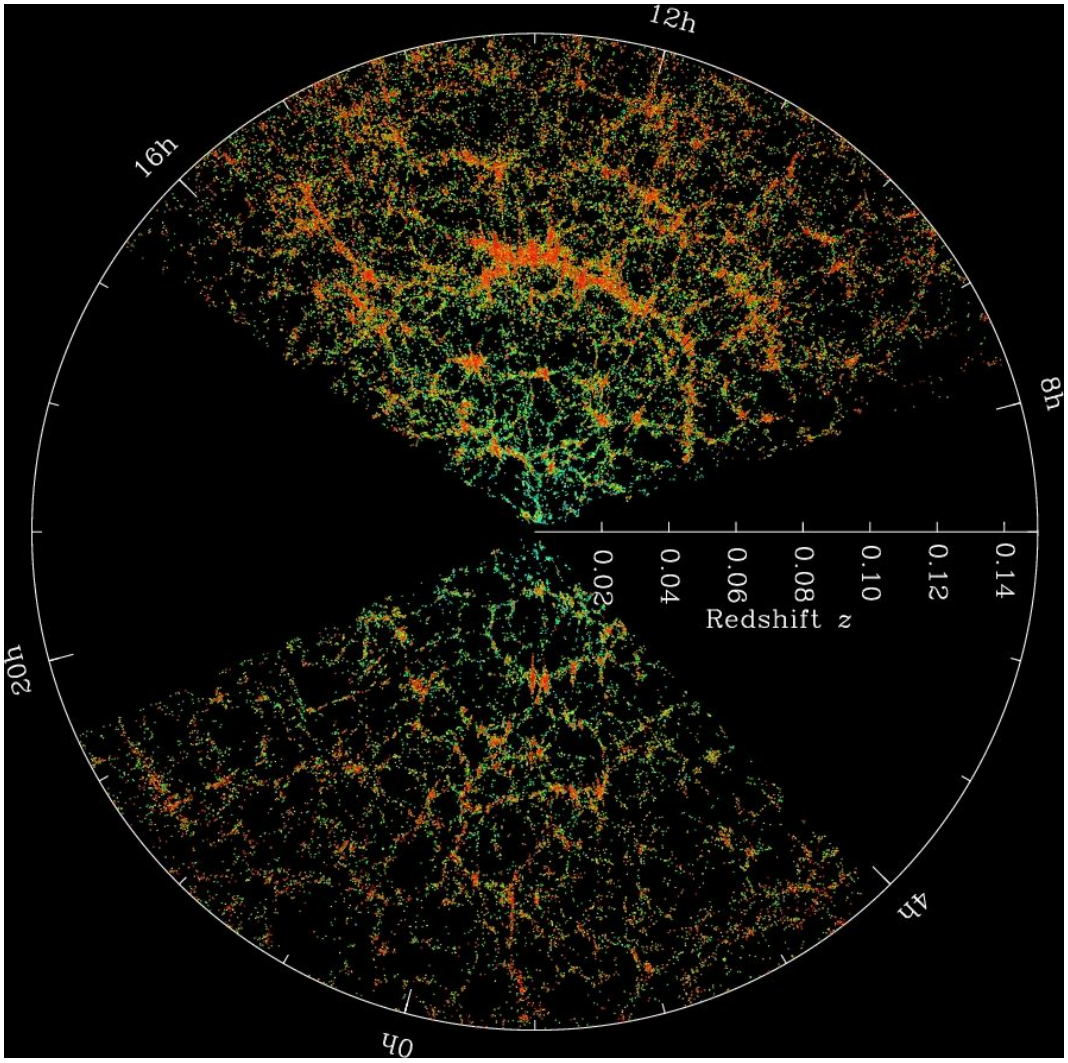

Figure 1.2: SDSS galaxy distribution map. Each point in the image corresponds to a galaxy. The dark areas between the galaxies represent voids. Image courtesy: M. Blanton and SDSS.

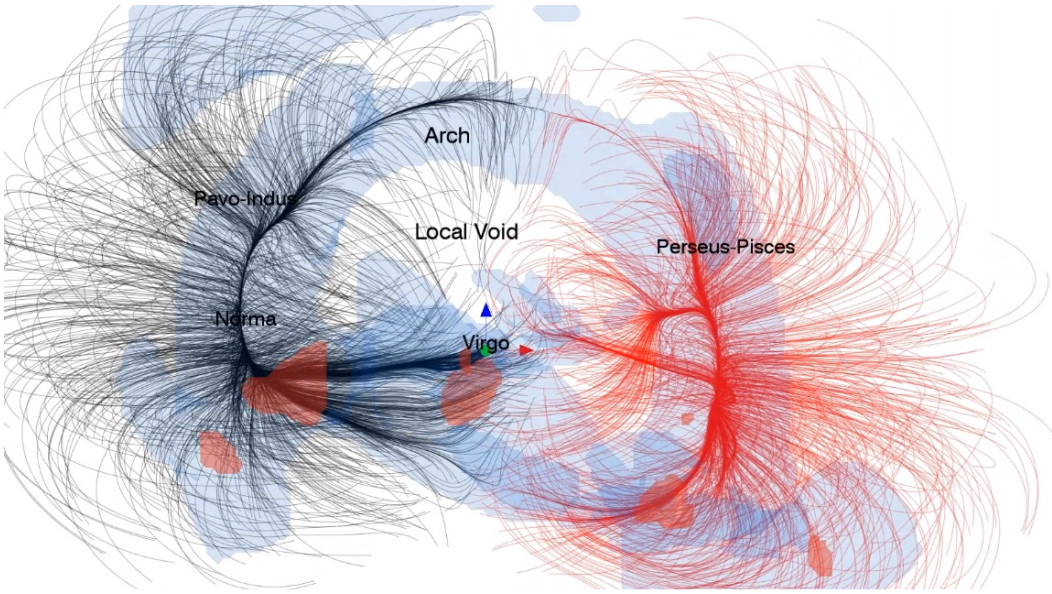

Figure 1.3: Velocity outflow in the Local Universe. The origin point of the three colored vectors indicate the location of our galaxy. Figure from (Tully et al. 2014).

through catalogues. Such a catalogue was compiled by Pan et al. 2012 who used the SDSS DR7 in order to study the distribution and properties of cosmic voids in the local Universe. P. M. Sutter et al. 2012 have also used a galaxy sample from the SDSS DR7. They applied the Watershed transform in order to identify voids which were subsequently compiled in a void catalogue. The largest, most up to date catalogue was developed by Nadathur 2016 and included a number of 8956 voids. The authors used the ZOBOV algorithm (Neyrinck 2008) to identify the voids in the galaxy distribution.

Numerical simulations also managed to recreate the existence of voids in the cosmic web. For example, Regos and Geller 1991 used PM N-body simulations to study spherical top hat perturbations of different sizes. They found that voids collide with one another, leading to large scale velocity flows. van de Weygaert and van Kampen 1993 studied the development of underdensities in different power spectra scenarios. They focused on the structure and dynamics of voids, being the first to hint at the existence of a void hierarchy. The study of Sheth and van de Weygaert 2004 has extended the excursion set formalism and applied it to voids in order to study this hierarchy. Finally, as a consequence of the increase in computational resources, the possibility of investigating the substructure within voids became a reality (Goldberg and Vogeley 2004; Colberg, Sheth, et al. 2005; Aragon-Calvo and Szalay 2013; Wojtak, Powell, and Abel 2016; Kreisch et al. 2021).

1.3 Formation and Evolution

We have seen that voids represent a real and vital component of the cosmic web: they were observed in the galaxy distribution and recreated in numerical simulations. In this section, we will explain the basic models that account for their properties.

The key element in understanding the characteristics of voids is that they originate from underdensities present in the primordial density field. Having lower densities than the average, they will experience a repulsive gravity effect. In other words, because the surrounding regions

have a higher density they will attract more matter. As a consequence, voids will undergo super-Hubble flow expansion (i.e they will expand faster than the Universe). The effect of this expansion is to push the existing neighbouring matter (clusters, filaments and walls) towards the boundary of the voids. The evacuation of matter will leave the void more empty as time progresses. In the case of an ideal, isolated void the density value will reach δ = -1. In Fig. 1.4, one can see how a simulated void in ΛCDM scenario shows these characteristics.

The first theoretical models that tried to explain the formation of voids assumed that they evolve either from isolated, spherical (Hoffman and Shaham 1982) or ellipsoidal (Icke 1984) underdensities. In reality, voids can not be treated as isolated systems since their expansion causes them to merge with their neighbours or to interract with the surrounding structure.

Despite of this, some basic characteristics can be inferred from the simple model of an isolated, spherical void. For example, in the left panel of Fig. 1.5, we see the density profile evolution of a tophat void. One can notice the characteristics previously mentioned: the void expands causing the ridge to move at larger radii; at the same time, matter is being evacuated which causes the density to decrease, leaving the void more empty.

The formation of a ridge around the expanding void is also an important aspect. This points to a gradient in expansion: the inner layers close to the void boundary expand faster than the outer layers (repulsive gravity is stronger in the interior of the void than on the outside). As a consequence, the event of shellcrossing occurs: at some point during the evolution, the inner layers overtake the outer layers.

Bertschinger 1985a has proved that once voids reach the stage of shellcrossing, they will experience self-similar expansion. Once this happens, the rate of expansion decreases with respect to the linear expansion experienced in the earlier stages. Furthermore, Blumenthal et al. 1992 showed that in a matter dominated universe, shellcrossing occurs when a density depression reaches a lineary extrapolated density value of $\delta_{sc} = -2.81$. At this time, a spherical void will have expanded by a value of 1.72 (corresponding to a nonlinear density value of $\delta \approx -0.8$).

1.4 Void Dynamics

We mentioned previously that voids act as an organising element in the cosmic web. This role is manifested through the outflow of matter from the void's interior (recall Fig. 1.3).

The dynamics of voids is strongly dependent on the external tidal field generated by neighbouring structures. In addition, voids are limited to a density $\delta = -1$, which limits their gravitational influence. To analyse this aspect in a quantitative manner, we start by looking at the predictions made by the linear perturbation theory.

In this framework, the outflow velocity inside a void increases linearly with the distance from the void center. The linear increase occurs due to the void expansion which makes them become super-Hubble bubbles. This is given by:

$$v_{lin} = -\frac{1}{3} H_0 f(\Omega_0) r \Delta(r) \tag{1.1}$$

where $f(\Omega_0) \approx \Omega_0^{\gamma}$ is the velocity function (Peebles 1980) . $\Delta(r)$ is the density contrast within radius r and is given by:

$$\Delta(r) = \frac{3}{r^3} \int_0^r r'^2 \delta(r') dr' \tag{1.2}$$

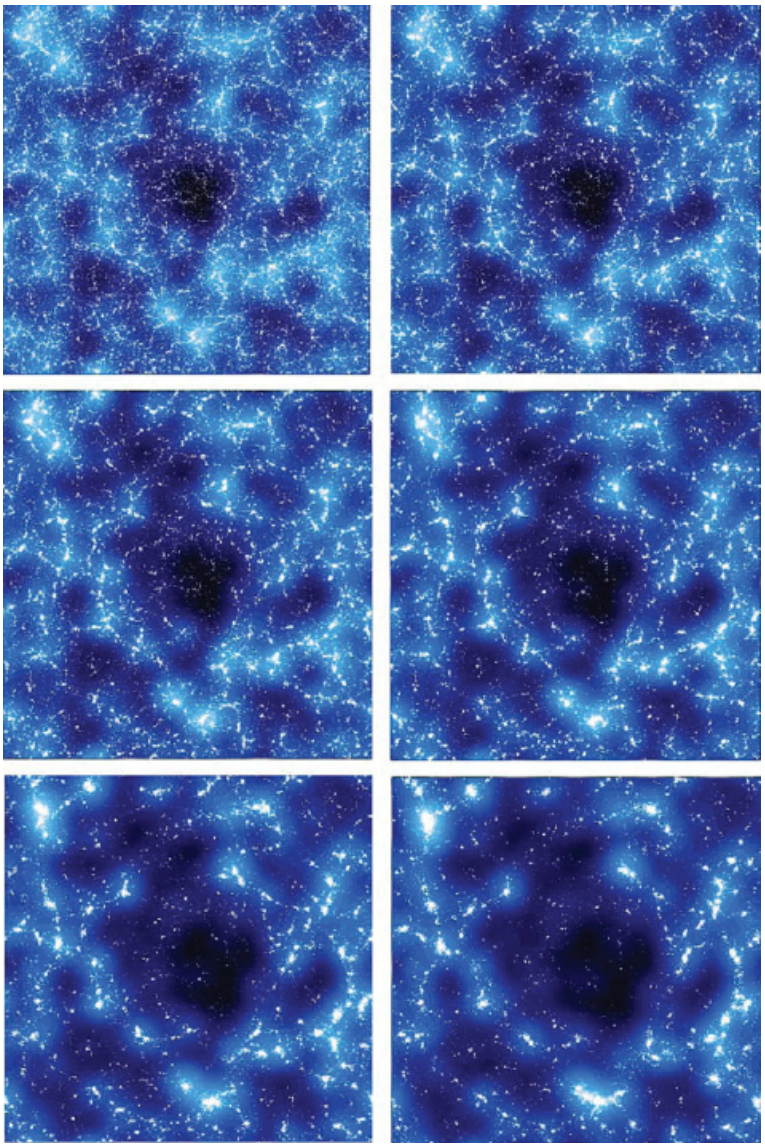

Figure 1.4: Simulated void in ΛCDM scenario across 6 time steps. Starting from the top left towards bottom right, the 6 times steps are: a=0.05, 0.15, 0.35, 0.55, 0.75 and 1. The void expands slowly and pushes the matter content towards its boundary. Figure from Platen 2009.

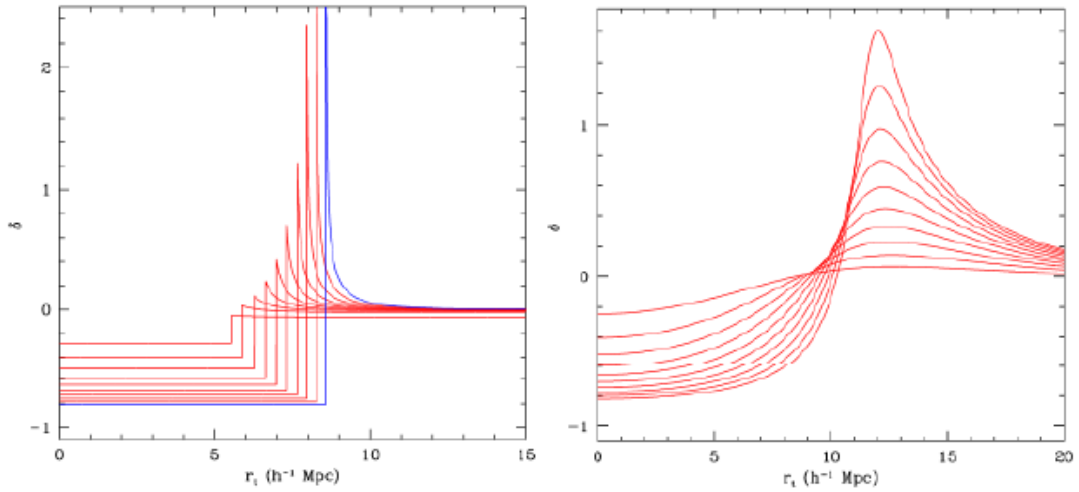

Figure 1.5: *Left*: Density profile evolution of a tophat void. The time steps show how the density evolves into a "bucket-shape" profile. *Right*: Same situation, except the spherical void evolves from an angular averaged underdensity embedded in a CDM Gaussian random field. In both cases, the initial density deficit is Δ = - 10 and the initial radius is $R_0 = 5$ h^{-1} Mpc. Both voids show the process of expansion and evacuation of matter from the center and its accumulation towards the boundary, where it forms steep ridges. Figure from Sheth and van de Weygaert 2004

A further step in understanding the void dynamics is to look at how the velocity behaves in the non-linear regime. This is where the spherical outflow model comes into play. In this model, each shell of a spherically symmetric density perturbation is treated as an individual Friedmann universe. Then, the peculiar velocity is given by (Schechter 1980) :

$$v_{sph} = H_0 r \left[\frac{3}{2} \frac{\sinh \Phi_r (\sinh \Phi_r - \Phi_r)}{(\cosh \Phi_r - 1)^2} - 1 \right] \tag{1.3}$$

where Φ_r is the development angle. van de Weygaert and van Kampen 1993 showed how the radial velocity profile inside a simulated void deviates from the linear and spherical models (left panel of Fig. 1.6). They found that the radial velocity increases linearly from the center up to a distance of $\approx$ 10 Mpc and reaches a maximum at about $\approx$ 18 Mpc. The predicted linear radial velocity v_{lin} deviates by about $20-25\%$. By comparison, the spherical model v_{sph} approximates well the radial velocity profile up to a distance of 10 Mpc. Further out, the radial velocity starts deviating from the spherical model. This is explained by the increase in density (right panel of Fig. 1.6) which causes disturbances in the velocity field. The corresponding density profile is mostly flat below 15 Mpc, being in agreement with the linear increase of the radial velocity v_r.

In Chapter 6 we will make use of Eq. 1.1 and 1.2 in order to see how the voids in our work deviate from the predictions made by the linear theory. We will also compare the stacked density profiles for a sample of our voids with the average underdensity $\Delta(r)$.

1.5 Tidal field influence on voids

An important factor in the evolution and dynamics of voids is the effect of the tidal field generated by surrounding structure. The primary characteristics of voids that are affected are their shapes, mutual allignment and expansion.

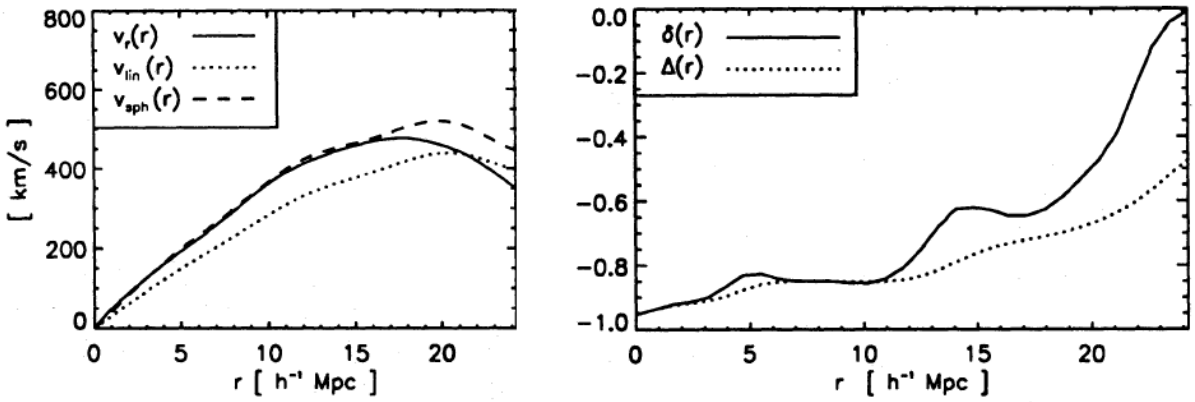

Figure 1.6: *Left:* Velocity profiles for a void in λCDM. The solid line shows the radial velocity of the void. A comparison is made with the radial velocity inferred from the linear theory v_{lin} (dotted line) and with the spherical model v_{sph} (dashed line). *Right*: The corresponding radial density profile together with the average underdensity within a radius r, $\Delta(r)$ (Eq. 1.2). Figure from (van de Weygaert and van Kampen 1993).

To understand how the tidal field plays its role in the void evolution, we discuss the homogeneous underdense ellipsoidal model (Icke 1984). The main assumption of this model is that voids can be represented by a triaxially symmetric ellipsoid with a uniform interior density. If external tidal shear is present then the gravitational acceleration induced is given by:

$$\frac{d^2R_m}{dt^2} = -4\pi G\rho_u(t)\left[\frac{1+\delta}{3} + \frac{1}{2}(\alpha_m - \frac{2}{3}\delta)\right]R_m - \tau_m R_m + \Lambda R_m \tag{1.4}$$

where R_m is the scale factor corresponding to one of the ellipsoid's axes, τ_m reflects the influence of the tidal field shear tensor and Λ is the cosmological constant. The factors α_m are the coefficients of the ellipsoid given by:

$$\alpha_m = R_1(t)R_3(t)R_3(t)\int_0^\infty \frac{d\lambda}{(R_m^2(t)+\lambda)\prod_{n=1}^3(R_n^2(t)+\lambda)^{1/2}} \tag{1.5}$$

We know that voids can never achieve densities $\delta > 1$. However, the tidal shear influence, τ_m, does not have any upper llimits. As such, tidal shears will deform the void, making it more anisotropic. Strong tidal shears may even lead to the collapse of voids, feature discussed more in the void hierarchy section.

Void shapes and dark energy

Isolated aspherical underdensities will tend to become more spherical over time (Icke 1984). This happens because the gravitational acceleration is stronger across the shorter axis of the ellipsoid. As a consequence, the anisotropies inside voids will diminish (van de Weygaert and van Kampen 1993).

However, voids will never reach perfect sphericity. Platen, van de Weygaert, and Jones 2008 showed that voids in a ΛCDM simulation are quite prolate, with the axes ratios of the ellipsoid being c:b:a $\approx$ 0.5:0.7:1 (see also our results in Chapter 4). We have already seen that the major factor responsible for this is the tidal influence. A second reason proposed by the authors is that

as voids expand, they will encounter other structures in the cosmic web which will prohibit them to reach perfect sphericity.

Besides the effect of the tidal field and of the surrounding structure, the void shapes are also affected by the presence of dark energy. Numerous studies have been dedicated to the study of voids as cosmic probes, that would help us gain a better understanding of dark energy. For example, Park and Lee 2007 were the first to derive an analytical model of the voids ellipticity distribution, which was showed to be dependent on the cosmological parameters. As a follow up, Bos et al. 2012 studied the void ellipticity using various N-body simulations in different dark energy scenarios. They confirmed the sensitivity of the voids shapes in dark matter simulation. However, they signalised that this sensitivity may not be easily detected in voids present in the galaxy distribution. Furthermore, Verza et al. 2019 confirmed the dependence of voids on dark energy using simulated halo catalogues.

An important contribution was brought by Lavaux and Wandelt 2012 who used the shape of voids from redshift surveys in order to study the expansion of the Universe. To do this, the authors used the fact that the shape of voids can be averaged out as being spherical. Then, the stretched shape that voids show in redshift surveys is a consequence of the Hubble expansion which, in turn, is dependent on cosmic parameters (dark energy in particular).

1.6 Void hierarchy

We have seen that the basic characteristics of voids can be inferred from the simple models of an isolated, spherical (or ellipsoidal) void. However, in reality voids are not isolated and the interaction with their peers and the surrounding structure can lead to a more complex evolution. This interaction leads to a hierarchical evolution of voids whose main aspects are revealed in the voids substructure. The development of voids has been treated by Sheth and van de Weygaert 2004 in the context of the gravitational instability scenario. They proposed that two distinct processes lie at the root of the hierarchical evolution: void merging and void collapse.

In the first process, small voids embedded in a large underdense region will expand and merge together. As they do, the matter in between them will get squeezed in thin walls (or filaments). Eventually, the structure formed within the expanding voids will be evacuated along the boundary of the resultant void (top panel of Fig. 1.7).

In the second process, small voids embedded in collapsing overdense regions will be squeezed out of existence (bottom panel of Fig. 1.7). As the figure shows, the voids usually are situated at the boundary of the overdensity which will slowly collapse and cause their disappearance. This process is usually coupled with the effect of surrounding tidal field. Furthermore, the process is responsible for the cutoff of voids at smaller sizes (by contrast, the halo population is dominated by small objects).

In order to model the hierarchical build up of voids, Sheth and van de Weygaert 2004 extended the excursion set formalism (Press and Schechter 1974; Bond et al. 1991) into a two-barrier excursion set. In this formalism, the two barriers are associated with the critical density values necessary for the void collapse and merging processes. We know that in a matter dominated Universe, an overdensity collapses when the critical value of $\delta_{o,c} = 1.69$ is reached. Similarly, a void forms when the density threshold of shellcrossing $\delta_{v,c}$ = -2.81 is obtained.

Similar to how the original excursion set formalism takes care of the cloud-in-cloud problem, the two-barrier excursion set resolves the void-in-void problem: small voids embedded in larger voids will merge into a larger structure and thus, should no longer be considered.

One can also encounter the situation in which voids are present in larger overdensities: the void-in-cloud issue. These are the voids that will cease to exist due to the collapsing overdensity,

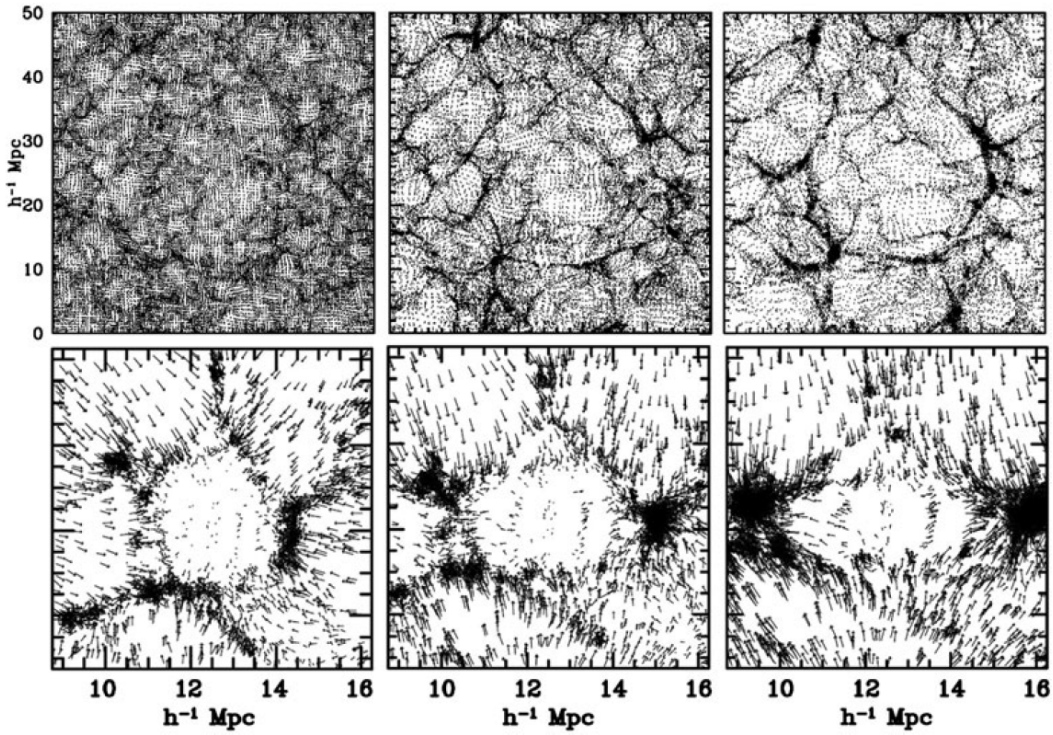

Figure 1.7: The two processes governing the void evolution: void merging (top panels) and void collapse (bottom panels). *Top*: Three different time steps ($a = 0.1, 0.3, 0.5$) illustrating the merging of smaller voids into a large void with a diameter of ≈ 25 h^{-1} Mpc. *Bottom*: Same time steps, this time the collapse and disappearance of three voids due to the surrounding matter infall is shown. Figure from Sheth and van de Weygaert 2004.

so they too should no longer be taken into account. The case of a cloud-in-void is not an issue because overdensities within voids will not be torn apart by the void's expansion.

1.7 Environmental influence of voids on dark matter halos and galaxies

Perhaps the most evident link between environment and evolution has been brought forward by the morphology-density relation (Oemler 1974; Dressler 1980). This relation suggests that the number of elliptical and lenticular galaxies increases in denser regions. By contrast, irregular and late-type galaxies tend to populate more the lower density regions. The difference is explained by processes, such as quenching, tidal stripping or ram pressure (Gunn and Gott 1972) that are present in denser regions and which would decrease the gas content in galaxies. The efficiency of these processes in environments such as voids is decreased which causes a more abundant number of late-type galaxies to be found there.

The low density setting of voids makes them ideal environments for the study of dark matter halo and, subsequently, galaxy formation. This is reflected in slow merger history and delayed evolution of galaxies that is not encountered in high density regions. In addition, the void galaxies provide a test of the ΛCDM model which predicts that underdense regions should contain numerous dark matter halos with lower masses than the average (Peebles 2001). These halos should be observed in surveys as low luminosity galaxies populating the voids. Instead, the absence of such observations creates a conundrum. Numerous studies have been dedicated to observing and determining properties of void galaxies (Grogin and Geller 1999; Grogin and Geller 2000; Kreckel, Platen, Aragón-Calvo, et al. 2012; Ricciardelli et al. 2014; Beygu et al. 2017; Pandey, Saha, and Pradhan 2021). The main characteristics found are that void galaxies are late-type disk galaxies with a high star formation rate. They are rich in gas, present low luminosities and appear bluer than the rest. All these properties are a consequence of the slow evolution that galaxies experience in voids.

Cosmological simulations have similarly shown that the properties of dark matter halos do not depend only on mass of the halo but rather depend on the environment as well. For example, Hahn et al. 2007 used GADGET-2 simulations in order to study how the characteristics of halos, such as formation redshift, spin and shape, vary with environment. In this case, the cosmic web was separated in clusters, filaments, sheets and voids based on the eigenvalues of the tidal field tensor. The authors found that halos with the highest masses in filaments spin faster than halos with the same masses in clusters. Furthermore, the halos located in voids have been found to have the lowest median spin values. They also report that the median sphericity (for a particular mass interval) decreases from denser environments, such as clusters and filaments, up to voids. A correlation between the halo formation time with environment and mass has also been found. For a certain mass regime, halos in clusters were more developed than halos in voids, who formed more recently.

A series of studies (Ganeshaiah Veena et al. 2018; P. Ganeshaiah Veena et al. 2019) which focused on the alignment of halos with respect to the filaments have also found environmental dependencies. The analysis was based on the Planck-Millenium simulation (Baugh et al. 2019) and the environment identification was performed using the NEXUS algorithm (Aragón-Calvo et al. 2007; Cautun, van de Weygaert, and Jones 2013). One of their findings indicates that the halo mass function is dependent on the environment: halos with the largest masses are located in clusters while the less massive halos in voids. Similarly with the result of Hahn et al. 2007, the authors found a small variation of the halo shapes with the cosmic web environment. They report that halos located in voids and nodes are more flattened than halos in walls and filaments.

In addition, they also report that halos in filaments and walls have the largest spin followed by the halos in voids and nodes.

Confirmation of the environmental dependence proceeds up to the present date, with the study of Hellwing, Cautun, et al. 2021. They use the Copernicus Complexio suite of N-body simulations (Hellwing, Frenk, et al. 2016) and characterise the web environment using the NEXUS+ algorithm (Cautun, van de Weygaert, and Jones 2013). For the first time, the authors study halos spanning six order of magnitude in mass and have managed to confirm previous results. This includes that large mass halos are present in filaments while the lower mass ones reside in voids. Interestingly, at the lower end of the mass function, they found that the fraction of halos in voids, walls and filaments is almost equal to $\approx \frac{1}{3}$ for each environment. The spin parameter manifests environmental differences only for more massive halos. The void sample indicated a reduced spin in comparison with the universal mean. Furthermore, halos living in less dense mediums appear to be more prolate.

On the basis of these studies, it is reasonable to assume that the location of halos in the cosmic web will impact their development and properties. As noted by Hellwing, Cautun, et al. 2021, the way in which this dependence is assessed will rely on the web finders used. Ideally, one would want to compare how the halo properties vary in various environments taking into account the algorithm used to trace the various components of the cosmic web. In the end, this will provide a much more physically motivated scenario of evolution of galaxies and could establish a better link between observations and predictions made by theory.

We have seen so far why voids are essential in our understanding of the cosmic web, how they form and evolve and what effect do they have on halos and galaxy formation. In the next chapter, we will provide the current understanding of how structure in the Universe developed into the astounding cosmic web that we observe today. In Chapter 3 we describe the tools used to achieve our goal: we start with the identification of voids using the watershed transform, a mathematical operation implemented in the Watershed Void Finder. Then, we present the principles of N-body simulations and focus on the GADGET-2 code and its gravitational algorithms. We follow with the DTFE algorithm, a method which uses tesselation in order to obtain the underlying density field from a particle distribution. Finally, in the last section of Chapter 3 we present the identification of halos in the dark matter particle distribution using the ROCKSTAR algorithm. Furthermore, we concretely discuss how the convex hull algorithm can be used to identify halos within voids. In Chapter 4 we present our results regarding the void environment. Here we talk about the sizes, shapes, matter content and kinematics of voids. Chapter 5 deals with properties of the void halo population: abundance, mass function, spin and shape and how these properties relate with the void environment. Finally, we end this work with Chapter 6 in which we summarise the goal and the findings behind this work. We add some possible ideas and improvements that can extend our understanding on the void halos.

Chapter 2

Cosmology and formation of the Large Scale Structure

2.1 The concordance model: ΛCDM

The Cosmological Principle is one of the main pillars in Cosmology. This principle states that at large scales (≈ 100 Mpc), the Universe is homogeneous and isotropic. The discovery (Penzias and Wilson 1965) of an unpolarized, isotropic microwave radiation (later coined the Cosmic Microwave Background) has provided essential evidence in supporting this concept.

Furthermore, Hubble 1929 measured distances to galaxies and found that galaxies located further away were receiding faster. This is now known as the Hubble's law and is mathematically defined as:

$$\mathbf{v}_H = H_0 \mathbf{r} \tag{2.1}$$

where $\mathbf{v}_H$ is the velocity of a galaxy, $\mathbf{r}$ is the distance and H_0 is the Hubble constant. Coupling the Hubble's law with the Cosmological Principle, we can state that we live in a Universe that undergoes homogeneous and isotropic *expansion*.

In order to quantify the expansion, a new coordinate system has to be introduced - the comoving coordinates $\mathbf{x}$. These coordinates are associated with an observer that follows along the expansion. As such, the distance to a galaxy can now be written as

$$\mathbf{r} = a(t)\mathbf{x} \tag{2.2}$$

where $a(t)$ is the scale factor, dependent on time. At the present moment ($t = t_0$), the scale factor is equal to one.

Differentiating Eq. 2.2 with respect to time will give

$$\mathbf{v}_H = \frac{\dot{a(t)}}{a(t)}\mathbf{r} \tag{2.3}$$

Comparing with Eq. 2.1, we can identify $H_0 = \frac{\dot{a(t)}}{a(t)}$. Note that in deriving this result, we assumed that galaxies do not posses any peculiar velocities (that is, their motion does not deviate from the Universe's expansion: $\dot{\mathbf{x}} = 0$).

In order to understand how the Unviverse evolved and how structure emerged, one has to understand gravity - the dominant force at the large scale. In physics, gravity is described by the Einstein's field equations:

$$G_{\mu\nu} = \frac{8\pi G}{c^4} T_{\mu\nu} \tag{2.4}$$

where $G_{\mu\nu}$ is the Einstein's tensor which quantifies the curvature of spacetime. The stress-energy tensor $T_{\mu\nu}$ describes the density and flux of energy. Essentially, Eq. 2.4 conveys that the source of spacetime curvature (left hand side) is matter (right hand side). Conversely, it implies that the movement of matter is dictated by the spacetime curvature.

In general, the stress-energy tensor is a complex quantity to compute. However, a simple solution does exist for the Einstein's equations if one assumes a scenario in which our expanding Universe is filled with a homogeneous and isotropic gas. Such a gas would be described by only its energy density ρ and pressure P. Furthermore, to describe the curvature of spacetime, the metric is given by:

$$ds^2 = -c^2 dt^2 + a(t)^2 \left[dr^2 + S_k(r)^2 d\Omega^2 \right] \tag{2.5}$$

where

$$S_k(r^2) = \begin{cases} R_0 \sin(\frac{r}{R_0}) & , k = +1 \\ r & , k = 0 \\ R_0 \sinh(\frac{r}{R_0}) & , k = -1 \end{cases} \tag{2.6}$$

The parameter k gives the curvature of the Universe while the radius of curvature is given by R_0. If k = +1, the curvature is positive while if k = -1 we are dealing with a negatively curved Universe. A flat Universe corresponds to k = 0.

Besides the curvature, another ingredient necessary in describing the Universe's geometry is the time evolution of the scale factor a(t). If we continue with our model of the gaseous Universe, this evolution is described by the Friedmann equations:

$$\left(\frac{\dot{a}}{a} \right)^2 = \frac{8\pi G}{3c^2} \rho(t) - \frac{kc^2}{R_0^2} \frac{1}{a(t)^2} \tag{2.7}$$

The solution to this equation requires knowledge about the time evolution of the density ρ.

If we assume a flat Universe (k = 0), from the Friedmann equation we can obtain the critical density ρ_c:

$$\rho_c = \frac{3c^2 H(t)^2}{8\pi G} \tag{2.8}$$

With it, we can define the density parameter:

$$\Omega(t) = \frac{\rho(t)}{\rho_c} \tag{2.9}$$

This parameter indicates the fraction of the density in the Universe at a time t with respect to the critical density. We know that the Universe is composed of multiple components: matter (baryons and dark matter), radiation and dark energy. With this in mind, we can express Ω as the sum of the density parameters corresponding to these components: $\Omega = \Omega_b + \Omega_{dm} + \Omega_r + \Omega_\Lambda$. These parameters, together with the Hubble constant, form what is known as the concordance model in Cosmology - the ΛCDM model. Table 2.1 shows the most recent values which have been obtained by the Planck mission (Planck Collaboration et al. 2020). It is clear that we live in a Universe dominated by dark energy, with dark matter being the second dominant component.

Ω_b	0.0486 ± 0.0010
Ω_{dm}	0.2589 ± 0.0057
Ω_r	$\approx 10^{-5}$
Ω_Λ	0.6911 ± 0.0062
H_0	$67.74 \pm 0.46 kms^{-1}Mpc^{-1}$

Table 2.1: Parameters of the model extracted from Planck Collaboration et al. 2020.

2.2 Emergence of the Large Scale Structure

If we look around us, we certainly do not notice the homogeneity and isotropy advertised by the Cosmological Principle. After all, humans, planets, stars and galaxies are pretty well defined structures. We have to conclude then, that the Cosmological Principle only applies to the very large scales of hundreds of megaparsescs. So how did all the structure came to be?

In Cosmology, the large scale structure refers to objects that are bigger than galaxies (e.g clusters and superclusters of galaxies). These structures formed as a consequence of density perturbations present in the early Universe.

In order to quantitatively understand the growth of large structure (process known as gravitational instability), we define the density perturbation at a position $\mathbf{r}$ and at a time t as:

$$\delta(\mathbf{r}, t) = \frac{\rho(\mathbf{r}, t) - \bar{\rho}(t)}{\bar{\rho}(t)} \tag{2.10}$$

where $\rho(\mathbf{r}, t)$ is the density value at position $\mathbf{r}$ and at a time t while $\bar{\rho}(t)$ is the average density in the Universe at the same time t. An overdense region will have $\delta(\mathbf{r}, t) > 0$ while an underdense region will have $\delta(\mathbf{r}, t) < 0$. Notice that there is a lower limit: when $\rho(\mathbf{r}, t) = 0$ then $\delta(\mathbf{r}, t) =$ -1. No upper limit exists - the density perturbation can have any positive value. Thus, we can see that overdense regions will gravitationally attract more matter over time. When a critical density is reached, the overdense region will stop expanding with the Universe and proceed to collapse. This will lead to the formation of dark matter halos. On the other hand, underdense regions (voids) will expand, pushing the existing matter outwards.

Further on, to analyse the statistical properties of the density field, we expand $\delta(\mathbf{r}, t)$ in terms of its Fourier components:

$$\delta(\mathbf{r}) = \frac{V}{(2\pi)^3} \int \delta_{\mathbf{k}} e^{-i\mathbf{k}\cdot\mathbf{r}} d^3k \tag{2.11}$$

where V is the comoving volume that expands with the Universe and the Fourier components δ_k are obtained by:

$$\delta_{\mathbf{k}} = \frac{1}{V} \int \delta(\mathbf{r}) e^{i\mathbf{k}\cdot\mathbf{r}} d^3r \tag{2.12}$$

This procedure emphasises the contribution of density perturbations with various wavenumbers $\mathbf{k}$ to the overall density field.

Inflationary scenarios predict that the primordial density field is Gaussian in nature. The main reason supporting this is that density perturbations are believed to originate from inflationary quantum noise which posses a Gaussian character. As a result, the value of the density perturbations at a position $\mathbf{r}$ is randomly selected from a Gaussian probability distribution:

$$p(\delta) = \frac{1}{\sqrt{2\pi}\sigma_\delta} e^{-\frac{\delta^2}{2\sigma_\delta^2}} \tag{2.13}$$

In order to compute the variance σ_δ^2, we first introduce the Power Spectrum. This quantity is obtained by squaring the amplitude of the Fourier components (Eq. 2.12) and taking its average:

$$P(k) = \langle |\delta_{\mathbf{k}}|^2 \rangle \tag{2.14}$$

Then, the variance of the Gaussian distribution is obtained by:

$$\sigma_\delta^2 = \frac{V}{(2\pi)^3} \int P(k) d^3k \tag{2.15}$$

This shows that the statistics of the Gaussian density field is completely determined by the power spectrum P(k), cementing its importance in Cosmology. Usually, the power spectrum predicted by inflation is expected to take a power law form:

$$P(k) \propto k^n \tag{2.16}$$

where the spectral index n indicates the power of different wavemodes to the density field. Inflation predicts a spectral index of n = 1 (also known as the Harrison-Zel'dovich spectrum). Such a power spectrum presents a scale-free potential perturbation and assures a hierarchical evolution of structure (that is, the small scale perturbations have a higher amplitude than those at large scales).

2.3 Linear Perturbation Theory

Now that we have seen that the structure we observe originates from density perturbations, we want to investigate how these fluctuations evolve over time. In the linear stage of evolution (when the fluctuations are very small, $\delta << 1$), the growth of perturbations can be described using the linear perturbation theory. We first specify the perturbation quantities that will help describe this evolution:

$$\delta(\mathbf{x},t) = \frac{\rho(\mathbf{x},t) - \bar{\rho}(t)}{\bar{\rho}(t)} \quad \text{Density perturbation} \quad (2.17)$$

$$\mathbf{v} = a(t)\dot{\mathbf{x}} \quad \text{Peculiar velocity} \quad (2.18)$$

$$\phi(\mathbf{x},t) = \Phi(\mathbf{r},t) - \frac{1}{2}a\ddot{a}x^2 \quad \text{Potential perturbation} \quad (2.19)$$

$$\mathbf{g}(\mathbf{x},t) = -\frac{\nabla\phi}{a} \quad \text{Peculiar gravity} \quad (2.20)$$

Eq. 2.17 is the perturbation to the density field encountered before. Eq. 2.18 is the peculiar velocity and can be obtained from differentiating Eq. 2.2 with respect to time. It essentially describes how the total velocity **u** of a galaxy deviates from the Hubble's flow ($\mathbf{v} = \mathbf{u}(\mathbf{r}, t)$ - $\mathbf{v}_H$ ($\mathbf{r}$, t)). Eq. 2.19 specifies perturbations in the gravitational potential field and can be linked to the density perturbation via the Poisson's equation. Eq. 2.20 is the peculiar acceleration and is defined in terms of the potential perturbation. This equation reflects the surplus acceleration with respect to the background Universe.

Now that the perturbation quantities were defined, we can further assume that the matter and radiation in the Universe form a continuous fluid. Such an assumption is valid only when considering megaparsec scales. At these scales, the discreetness of galaxies, stars and planets can be neglected. It follows then that the cosmic fluid can be described by the three fluid equations:

$$\frac{\partial\rho}{\partial t} + \nabla_r \cdot \rho\mathbf{u} = 0 \quad \text{Continuity equation} \quad (2.21)$$

$$\frac{\partial\mathbf{u}}{\partial t} + (\mathbf{u}\cdot\nabla_r)\mathbf{u} = -\frac{1}{\rho}\nabla_r P - \nabla_r\Phi \quad \text{Euler equation} \quad (2.22)$$

$$\nabla_r^2\Phi = 4\pi G\left(\rho(\mathbf{r},t) + \frac{3P}{c^2}\right) \quad \text{Poisson equation} \quad (2.23)$$

Eq. 2.21 describes the mass conservation of a fluid element. Eq. 2.22 indicates that the acceleration of fluid elements is caused by the existence of pressure gradients and gravitational forces. Finally, Eq. 2.23 shows that the source of the gravitational potential is the energy density of matter. The pressure term P that appears corresponds to the radiation and dark energy.

In order to see how the perturbations grow with time (with respect to the expanding background Universe) we must convert the fluid equations from physical coordinates to comoving coordinates. A second step requires to replace the physical quantities, $\rho, \mathbf{u}, \Phi$ with the perturbation quantities, $\delta, \mathbf{v}, \phi$. Since the structure formation occurs in the matter dominated epoch, we will neglect the pressure and energy density terms of radiation. The perturbations in energy density due the dark energy component will not develop. The reason being that dark energy has negative pressure which will produce a uniform, unperturbed medium. As such, we are left with matter perturbations only. The linearized fluid equations will then take the form:

$$\frac{\partial\delta}{\partial t} + \frac{1}{a}\nabla_x\cdot\mathbf{v} = 0 \quad (2.24)$$

$$\frac{\partial\mathbf{v}}{\partial t} + \frac{\dot{a}}{a}\mathbf{v} = -\frac{1}{a}\nabla\phi \quad (2.25)$$

$$\nabla^2\phi = 4\pi G a^2\rho_u\delta \quad (2.26)$$

If we take the divergence of Eq. 2.25 and combine it with the linearized continuity equation (Eq. 2.24), we obtain the following expression:

$$\frac{\partial^2\delta}{\partial t^2} + 2\frac{\dot{a}}{a}\frac{\partial\delta}{\partial t} = \frac{3}{2}\Omega_0 H_0^2 \frac{1}{a^3}\delta \tag{2.27}$$

where in a matter dominated Universe $\Omega_0 = \frac{8\pi G\rho_0}{3H_0^2}$. This is a second order, partial differential equation whose solutions describe the growth of density perturbations. The general solution to this equation can be written as:

$$\delta(\mathbf{x}, t) = D_1(t)\Delta_1(\mathbf{x}) + D_2(t)\Delta(\mathbf{x}) \tag{2.28}$$

where $D_1(t)$ and $D_2(t)$ are the density growth factors, showing how the perturbation evolves with time. The $\Delta_1(\mathbf{x})$ and $\Delta_2(\mathbf{x})$ are the spatial configuration of the matter distribution.

Now that the general solution has been obtained, we can consider a matter dominated Universe ($\Omega_0 = 1$). In such a case, the density growth factors are:

$$D_1(t) \propto t^{2/3} \tag{2.29}$$

$$D_2(t) \propto t^{-1} \tag{2.30}$$

where $D_1(t)$ is the growing mode solution while $D_2(t)$ is the decaying mode solution. At the current epoch, we can discard $D_2(t)$ since it slowly decreases with time. As such, we finally see that in a matter dominted Universe, the density perturbations grow according to: $\delta(\mathbf{x}, t) \propto D(t) \propto t^{2/3}$.

Another important result inferred from the linear perturbation theory is the relation between peculiar velocity and peculiar gravity. In order to obtain this, we extract the density perturbation from the linear Poisson equation (Eq. 2.26) and replace it in the linear continuity equation (Eq. 2.24), such that:

$$\nabla \cdot \mathbf{v} = -a\nabla \cdot \frac{\partial}{\partial t}\left(\frac{\nabla\phi}{4\pi G a^2 \rho_c}\right) \tag{2.31}$$

Using the definition of peculiar gravity (Eq. 2.20) and knowing that $\mathbf{g}$ grows as $\mathbf{g}(t) \propto \frac{D}{a^2}$ (see van de Weygaert[1] for a full derivation) we obtain:

$$\mathbf{v} = \frac{Hf}{4\pi G\rho_c}\mathbf{g} \tag{2.32}$$

where f is the dimensionless linear velocity growth factor defined as

$$f = \frac{1}{D}\frac{dD}{dt} \tag{2.33}$$

whose value was computed by Peebles 1980 for a matter dominated Universe to be $f \propto \Omega_m^{0.6}$.

Eq. 2.32 is one of the most fundamental results in the linear perturbation theory because it shows that the peculiar velocity $\mathbf{v}$ is proportional to the peculiar gravitational field $\mathbf{g}$, generated by the density perturbations.

[1] https://www.astro.rug.nl/ weygaert/tim1publication/lss2009/lss2009.linperturb.pdf

We can summarize the results of the linear perturbation as follows: given an initial Gaussian random field, density perturbations will develop due to quantum noise. These perturbations will generate fluctuations, **g**, in the gravitational field. Subsequently, according to Eq. 2.32, the peculiar gravity field will generate a peculiar velocity component. As a consequence, matter will be displaced from the underdense regions towards the overdense ones. When an overdense region reaches a critical density, it will turn around from the Hubble flow and it will begin to collapse. This process will lead to the formation of dark matter halos, the subject of the next section.

A final remark to note is that when the density perturbations have grown large enough ($\delta \approx 1$), linear perturbation theory can no longer be applied. This is because in the linear regime, the wavemodes of the perturbations evolve independently. By contrast, in the non-linear stage of evolution the different wavemodes of perturbations begin to couple to each other and can not be analytically described.

2.4 Dark matter halos

Dark matter is the dominant matter component in the Universe. It provides gravitational potential wells in which baryons can fall into and form galaxies. In this section we will discuss the formation mechanism of dark matter halos and present some inherent properties.

In order to see how an object emerges from the initial density field, consider a spherical overdensity composed of thin mass shells. The radius r of an individual shell of mass M evolves according to:

$$\frac{1}{2}\left(\frac{dr}{dt}\right)^2 - \frac{GM}{r} = E \tag{2.34}$$

where E is the specific energy of the shell. For the object to collapse, we require that $E < 0$. Then the solution to this equation can be written as:

$$r = A(1 - \cos\theta); \qquad t = B(\theta - \sin\theta) \tag{2.35}$$

where A and B are constants determined from the initial conditions. These equations show that the mass shell undergoes three stages of evolution. Initially, the shell expands from r = 0 at t = 0 (corresponding to a $\theta = 0$). At a time t = B π (when $\theta = \pi$), the shell will reach a maximum value r_{max} (also known as the turn-around radius). Finally, at t = 2π, the shell collapses back to r = 0.

In a matter dominated Universe, it was found that a spherical overdensity δ will reach a maximum radius when $\delta = \delta_l(t_a) \approx 1.06$. The same overdensity will collapse when $\delta = \delta_c(t_{col}) \approx 1.686$. In reality, however, a collisionless system such as this one is unable to dissipate energy. As a consequence, the gravitational potential energy is converted into kinetic energy of the particles that made up the mass shells. As time evolves, the sphere will eventually relax (or virialize) to a system supported by random motions.

Now that we established the critical density value necessary for collapse, we need to assign masses to the collapsed regions. To do so, we make use of the Press-Schechter formalism (Press and Schechter 1974) which states the following: given a density field δ_s smoothed with a filter W(**x**, R) of radius R and mass M $\propto \bar{\rho}R^3$, the probability that $\delta_s > \delta_c$ is equivalent to the fraction of mass elements that are within halos that have masses larger than M. Assuming an initial density field, the probability that $\delta_s > \delta_c$ is given by:

$$P(> \delta_c(t)) = \frac{1}{2}\text{erfc}\left[\frac{\delta_c(t)}{\sqrt{2}\sigma(M)}\right] \tag{2.36}$$

where the mass variance $\sigma(M)^2$ is given by:

$$\sigma^2(M) = \frac{1}{2\pi}\int_0^\infty P(k)\tilde{W}^2(\mathbf{k}R)k^2 dk \tag{2.37}$$

Here P(k) is the power spectrum of the density fluctuations and $\tilde{W}$ (**k**R) is the Fourier transform of the filter. When $\sigma(M) \to \infty$, the probability P($>\delta_c(t)$) $\to \frac{1}{2}$, which generates a problem because it suggests that only half of the Universe's mass is part of collapsed objects of a given mass M. This is a consequence of the linear perturbation theory which states that only overdense regions are capable of forming collapse objects. To solve this issue, Press and Schechter multiplied Eq. 2.36 by an arbitrary factor of two and defined F($> M$) = 2 P($> \delta_c(t)$). This results into a number density of collapsed objects that have masses between M and M + dM of:

$$n(M,t)dM = \frac{\bar{\rho}}{M}\frac{\partial F(> M)}{\partial M}dM = \sqrt{\frac{2}{\pi}}\frac{\bar{\rho}}{M^2}\frac{\delta_c(t)}{\sigma(M)}\exp\left(-\frac{\delta_c^2(t)}{2\sigma^2(M)}\right)\left|\frac{d\ln\sigma(M)}{d\ln M}\right|dM \tag{2.38}$$

Eq. 2.38 is known as the Press-Schechter mass function and provides an understanding of how structure in the non-linear regime can evolve in a hierarchical way.

An alternative derivation of the halo mass function that does not suffer from the "fudge" factor was developed by (Bond et al. 1991) and is known as the excursion set formalism. In summary, this method infers the halo mass function from the Markovian random walk trajectories of a mass element with a corresponding overdensity δ_s as a function of a variable S = $\sigma^2(M)$. An illustration of this formalism can be seen in Fig. 2.1. Consider that the density field has been smoothed with a filter at a mass scale $S_1 = \sigma^2(M_1)$. The PS formalism then states that the fraction of trajectories that have passed the barrier $\delta_s > \delta_c$ at S_1 will be equal to the fraction of mass elements in collapsed objects that have M $> M_1$. Taking a look at the mass element with trajectory B, we will see that at S_1 it will not be part of a collapsed object with $M > M_1$ since $\delta_s < \delta_c$. However, on the interval $S_2 < S < S_3$, the same mass element has $\delta_s > \delta_c$ which implies that it will be part of a collapsed object with $M > M_3$. But $M_3 > M_1$! This is implies that the PS is not consistent. One can correct this by realising that trajectory B' is as equally likely as trajectory B. This stems from the consequence of the trajectories being Markovian random walks. As such, the mass fraction in halos with $M > M_1$ is given by twice the trajectories that passes through the barrier at S_1.

2.4.1 Internal properties of Dark Matter Halos

Having established how dark matter halos form, we proceed to discuss some of their internal properties. We will only mention those properties relevant for out study. For a more throughout description see (Mo, van den Bosch, and White 2010).

Halo shapes

In our description of the gravitational collapse, we assumed that the overdensities are spherical. In reality, the collapse of an overdensity is affected by the tidal field of the surrounding structure. As a consequence, the collapse will be aspherical in nature and will produce flatten,

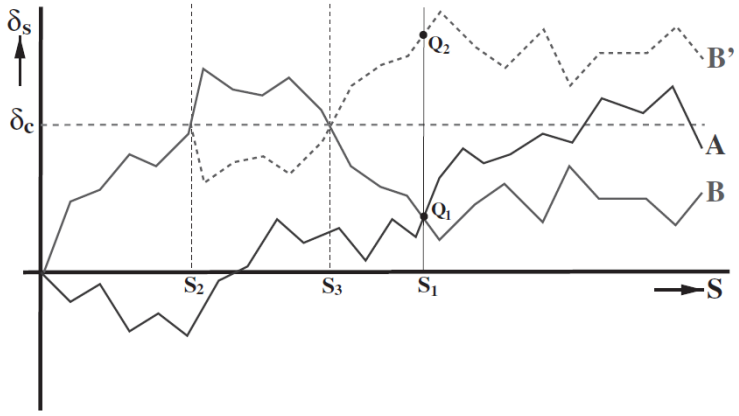

Figure 2.1: Illustration of the excursion set formalism. Figure shows the random walk trajectories of mass elements in the (S, δ_s) space. The horizontal dashed line indicates the critical density for spherical collapse δ_c. Trajectory B' is the reflection of B with respect to the δ_c line and is equally likely to occur since the random walks are Markovian in nature. Figure taken from (Mo, van den Bosch, and White 2010).

ellipsoidal halos. The shapes of the halo ellipsoids are thus described by ratios between the lengths of their axes:

$$s = \frac{c}{a}, \tag{2.39}$$

$$q = \frac{b}{a}, \tag{2.40}$$

$$p = \frac{c}{b}. \tag{2.41}$$

Numerical simulations showed that in general halos are triaxial ellipsoids which tend to be more prolate than oblate with $0.5 < s < 0.75$ and that halos with lower masses are more spherical. (Warren et al. 1992; Cole and Lacey 1996; Kasun and Evrard 2005; Bailin and Steinmetz 2005). A more recent study (Ganeshaiah Veena et al. 2018) finds more spherical halos, with $\frac{b}{a} > 0.9$ and $\frac{c}{a} > 0.8$.

Halo Angular Momentum

A second fundamental property of dark matter halos is angular momentum (or spin). The way in which halos acquire this property has been first proposed by Hoyle 1951 and later explored by Peebles 1969; Heavens and Peacock 1988 and is known as Tidal Torque Theory. Essentially, this theory states that in the linear regime proto-galaxies spin due to the interaction with the surrounding tidal field caused by the neighboring structures. N-body simulations performed by G. Efstathiou and Jones 1979 further confirmed that asymmetrical collapsing bodies end up with angular momentum.

To quantify the halo spin, Peebles 1969 has introduced the dimensionless parameter λ:

$$\lambda = \frac{J|E|^{\frac{1}{2}}}{GM^{\frac{5}{2}}} \tag{2.42}$$

where J is the angular momentum, E is the energy and M is the mass of the halo. Low values

of λ correspond to halos that are supported by velocity dispersions while high values suggest rotational support.

A more practical way, often used in the literature, is the Bullock spin parameter (Bullock et al. 2001). This parameter is preferred due to its advantage when dealing with a subvolume of a viriliazed sphere and is defined as:

$$\lambda = \frac{J}{\sqrt{2}MVR} \tag{2.43}$$

where J is the angular momentum within a sphere of radius R containing mass M and V is the circular velocity of the halo at distance R. The halo spin obeys a log normal distribution with an average between $\bar{\lambda} \approx 0.04 - 0.05$ (Heavens and Peacock 1988; Cole and Lacey 1996)

Halo density profile

The density profile of a halo describes its interior mass distribution. The simplest model used to approximate a virialized halo profile is the isothermal sphere:

$$\rho(r) \propto r^{-2}, r \leq r_h \tag{2.44}$$

Here, r_h (also known as the virial radius) represents the radius within which the mean density is:

$$\rho_h = \Delta_h \bar{\rho} = \Delta_h \rho_{crit} \Omega_m \tag{2.45}$$

where $\bar{\rho}$ is the average density in the Universe and ρ_{crit} is the critical density. Then, the profile can be written as:

$$\rho(r) = \frac{V_h^2}{4\pi G r^2}, \qquad r_h = \sqrt{\frac{200}{\Delta_h \Omega_m}} \frac{V_h}{10H(t)}, \qquad V_h = \sqrt{\frac{GM_h}{r_h}} \tag{2.46}$$

where V_h is the circular velocity at r_h and M_h is the mass of the halo. The mean overdensity is considered to be equal to $\Delta_h = \Delta_{vir} = 200$ according to the virial theorem.

However, obtaining a density profile based on the spherical collapse model will produce an inaccurate representation. Deviations may appear due to several factors such as: 1) equilibrium state may not be reached in the outer region of the halo, 2) importance of non-radial motion and 3) the hierarchical formation of a halo may cause the model to fail.

However, numerical simulations of structure formation have managed to offer better approximations. Especially, the study of Navarro, Frenk, and White 1996 found that halo density profiles are well described by (what is now known as) a Navarro, Frenk White (NFW) profile:

$$\rho(r) = \rho_{crit} \frac{\delta_{char}}{(\frac{r}{r_s})(1 + \frac{r}{r_s})} \tag{2.47}$$

where r_s is the scale radius, δ_{char} is the characteristic overdensity. It has been showed that the NFW profile represents a good approximation for the equilibrium density profiles of halos regardless of the mass and cosmological model used.

2.5 Cosmic Web

We mentioned in Chapter 1 that the matter distribution in the Universe resembles a cosmic web. This is apparent in both observations and N-body simulations. For example, Fig. 2.2 shows the galaxy distribution obtained through the 2 degree field galaxy survey (2dF) (Colless et al. 2003). At first glance, one can see that the galaxies are not randomly distributed in the Universe but are grouped into clusters and filaments. Between these components lie the voids which stand out as the empty regions on which galaxies lie on. Similarly, Fig. 2.3 [2] shows a slice through the Illustris simulation focusing on a massive galaxy cluster.

In Section 2.3 we have used linear perturbation theory to investigate how structure emerges out of the minute density fluctuations. We also noted that when $\delta \approx 1$ structure will grow non-linearly. As such, we no longer be able to assume that density perturbations of different modes are acting independently. To give an example, one may deal with a collapsing peak. When such a region starts collapsing under its own gravity, the corresponding density modes will begin to grow. This occurs due to the interaction with the neighbouring structure at different scales. Another example may include overdense small regions embedded in larger overdense structures. In this case, the smaller regions will enter non-linearity and collapse faster.

An extremely useful way to describe the non-linear evolution (and to understand the appearance of the cosmic web) has been developed by Zel'Dovich 1970 and is known as the Zel'Dovich approximation. Essentially, this approach uses Lagrangian perturbation theory and follows the displacement of a mass element from an initial Lagrangian position $\mathbf{q}$ to a final Eulearian location $\mathbf{x}(\mathbf{q}, \mathrm{t})$:

$$\mathbf{x}(\mathbf{q}, t) = \mathbf{q} + D(t)\Psi(\mathbf{q}) \tag{2.48}$$

where D(t) is the linear growth factor and $\Psi(\mathbf{q})$ is the displacement vector which depends on the gravitational potential field: $\Psi(\mathbf{q}) \propto \nabla\phi$.

Furthermore, we can infer the evolution of density on the basis of mass conservation between the Lagrangian and Eulearian coordinates:

$$\rho(\mathbf{x}, t)d\mathbf{x} = \rho_u(t)d\mathbf{q} \tag{2.49}$$

where $\rho(\mathbf{x}, t)$ is the density at position $\mathbf{x}$ in Eulerian space while $\rho_u(t)$ is the average density at the Lagrangian position $\mathbf{q}$. It follows then that the density perturbation is given by:

$$1 + \delta(\mathbf{x},\ \mathbf{t}) = \frac{\rho(\mathbf{x}, t)}{\rho_u(t)} = \left|\left|\frac{\partial \mathbf{x}}{\partial \mathbf{q}}\right|\right|^{-1} \tag{2.50}$$

where $||...||$ is the Jacobian determinant. Further on, using Eq. 2.48, we can write the Jacobian more explicitly as:

$$\left|\left|\frac{\partial \mathbf{x}}{\partial \mathbf{q}}\right|\right|^{-1} = ||\delta_{mn} - a(t)\psi_{mn}||^{-1} = \frac{1}{[1 - a(t)\lambda_1][1 - a(t)\lambda_2][1 - a(t)\lambda_3]} \tag{2.51}$$

where ψ_{mn} is the deformation tensor and λ_1, λ_2 and λ_3 are its eigenvalues. These eigenvalues are essential because they provide clues onto the formation of the cosmic web components.

[2] https://www.illustris-project.org/media/

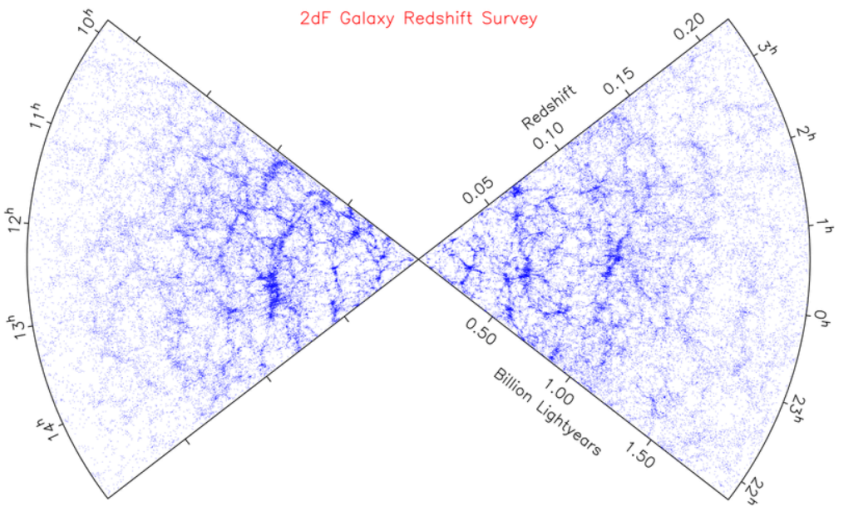

Figure 2.2: The web-like pattern of the galaxy distribution in the Universe. The redshift values shown here were obtained through spectral observations of the 2dF survey. A total number of 221,414 reliable galaxy spectra have been obtained.

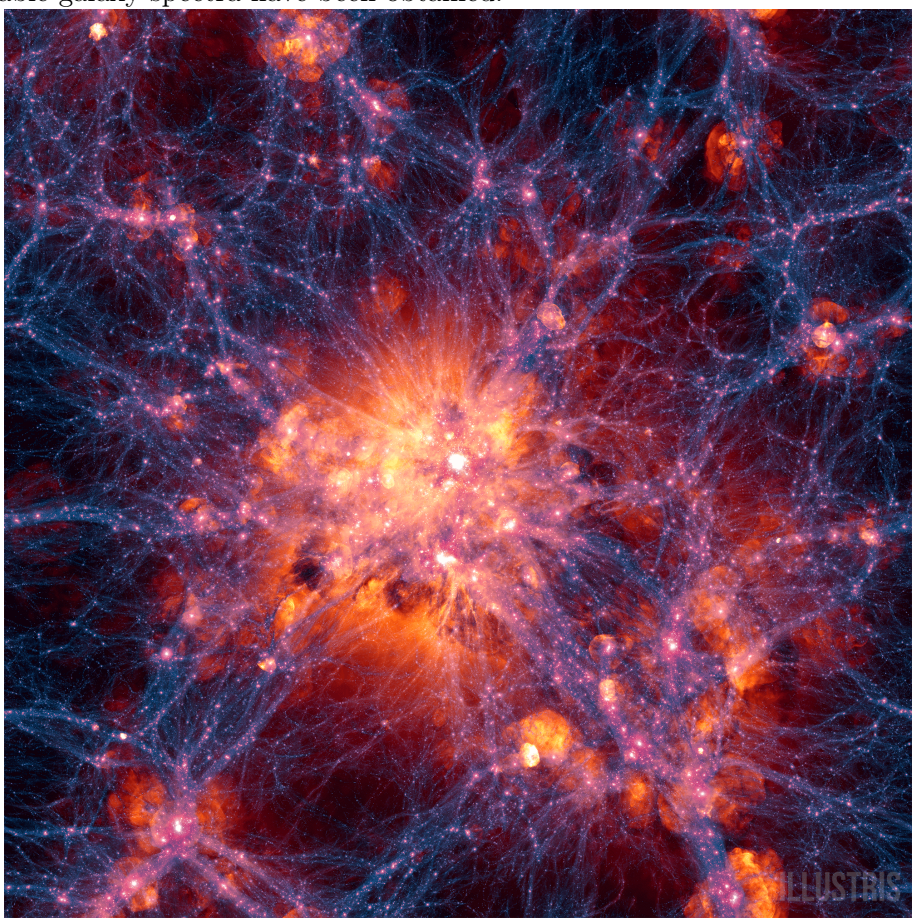

Figure 2.3: Projection through the Illustris simulation volume at present time. Image shows the dark matter density overlaid with the gas velocity. Image courtesy: Illustris Collaboration

Concretely, they represent the deformation axes of the ellipsoid density perturbation. If one of the eigenvalues is positive than the ellipsoid will collapse along that direction. Based on this, the cosmic web components are identified as follows:

i) Clusters: $\lambda_1 \approx \lambda_2 \approx \lambda_3 > 0$

ii) Filaments: $\lambda_1 \approx \lambda_2 > 0$

iii) Walls: $\lambda_1 > 0$

iv) Voids: $\lambda_1, \lambda_2, \lambda_3 < 0$.

The Zel'dovich approximation is an accurate description of the non-linear evolution up to the point of shell-crossing. At this point, a mass element will ignore gravitational attraction from its neighbours and will end up crossing through them. To correct for this, the adhesion model has been developed. At its core, this model introduces a viscosity term which takes into account the self-gravity of matter. Thus, shells of matter will be able to slow down as they approach each other.

So far, we have explored the theory behind the formation and evolution of the large scale structure. In the next chapter, we present the methods used in this work to explore the impact of the void environment on halos.

Chapter 3

Methodology

In this chapter we describe the tools used to analyse the effect that voids have on the properties of dark matter halos. In Section 3.1 we present the Watershed Void Finder algorithm which we used to identify voids in the GADGET-2 simulation. We follow with a description of GADGET-2, the N-body simulation used, and the governing principles and algorithms in Section 3.2. The last two sections will deal with simulation processing. In Section 3.3 we describe the Delaunay Tesselation Field Estimator (DTFE), a method used to obtain the density field from the particle distribution while in Section 3.4 we describe the ROCKSTAR Halo Finder, an algorithm used to identify halos. We also describe explicitly how we identified halos within the watershed voids using the convex hull algorithm.

3.1 Void identification: the Watershed Void Finder

We have seen that the spherical model predicts how a void looks like: an expanding spherical underdense region with a high density ridge. However, when it comes to identify voids in numerical simulations or observations, matters become more complex. This stems from the fact that, at the moment, there is no clear, agreed upon definition of voids. One can ask, then, how are voids identified ?

In this work, we used the Watershed Void Finder (WVF) (Platen, van de Weygaert, and Jones 2007) algorithm to identify the underdense regions in the GADGET-2 simulation. We choose the WVF because it offers several advantages in comparison with other void finders. First of all, the algorithm inputs as parameters only the filtering radii. No additional values have to be introduced. Furthermore, the algorithm recovers the geometry of the voids, despite their irregular shapes, since it is working directly on the topology of the field.

At the core of the WVF lies the *watershed transform*, a technique which stems from the field of mathematical morphology used in the segmentation of images. The watershed transform can be understood using a geophysical analogy. One can imagine a landscape (Fig 3.1) that is slowly being flooded by water. Initially, each basin (which represents a minimum point in the landscape surface) is punctured and it slowly starts to be filled in. The water level will increase until all the basins will meet at the ridges (these correspond to a maximum point). The last panel illustrates the segmented landscape - the ridges represent the boundaries that separate the flooded basins.

Using this analogy, we can see how the watershed transform translates in the context of the cosmic web. The basins in the density field are identified with underdense regions (voids) while the ridges separating them correspond to overdense regions (walls and filaments). In Fig. 3.2 we show the voids identified in this work by the WVF. One can notice how the irregular geometry and the variety of sizes and shapes of voids is maintained. The zoom-in panel shows the 3D

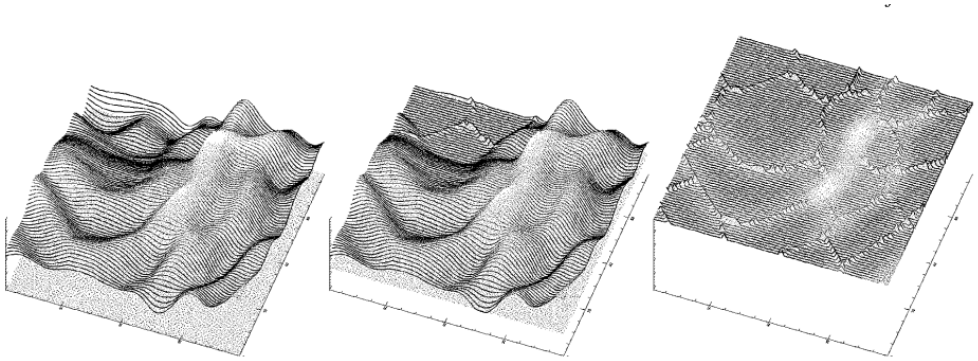

Figure 3.1: Plots illustrating the principle of the Watershed Transform by making use of a geophysical landscape with basins and ridges. From left to right, the landscape is slowly flooded with water until the whole landscape is submerged. The right image shows the final product of the segmentation procedure: flooded basins separated by ridges. Figure from Platen, van de Weygaert, and Jones 2007.

perspective of the cross-section of a ≈ 36 Mpc void from the left panel. The irregularities on the surface illustrate the ability of the WVF to preserve the topological shape of the void. The void shapes and sizes will be discussed in more detail in Chapter 4.

We enumerate now the primary steps used in the WVF to identify voids:

1. Once the density field of a given point distribution has been obtained, the WVF samples the field on a grid and smooths it using natural neighbour (NN) interpolation and median filtering. Contour densities of the image are then obtained via a uniform partitioning of the cumulative density distribution.

2. Minimum points in the smoothed density field are identified as the pixels that are surrounded by higher density values.

3. The flooding procedure begins at a minimum point. Once the density contour reaches a certain level, the pixels surrounding the minimum with a value below the density threshold of that contour are added as an element of the overall void region.

4. The segmentation of the image occurs when a pixel reaches a value common for two distinct basins. All the pixels with this particular value will form the boundary between the underdense regions. This process continues until all the landscape is segmented into void patches.

Besides its application in N-body simulations, the WVF is also an instrumental tool in identifying voids in redshift surveys. One of the aims of the work written by Platen, van de Weygaert, Jones, et al. 2011 was to investigate the topology of the SDSS galaxy distribution on the basis of the void population, identified by the WVF. The segmentation obtained through the watershed transform applied on a mock galaxy sample is compared with the segmentation applied on the magnitude-limited survey (Fig. 3.3). The authors report a good agreement between the two void segmentations at distances up to R $\approx 200\mathrm{h}^{-1}$ Mpc. At larger distances, the low resolution of the survey will result into small void segments from the mock sample to be embedded in larger magnitude-limited segments.

Furthermore, the WVF has also been proven useful in the identification of void galaxies. This makes it an ideal tool for the current work since we are interested in the identification of void halos. For example, a pilot study (Kreckel, Platen, M. A. Aragón-Calvo, et al. 2011) geometrically identified 60 galaxies in the SDSS survey. These galaxies are located in local voids (identified by the WVF) at distances less than 100 Mpc. Out of these, 15 are imaged in H1 (see Fig. 3.4). A follow up of this study (Kreckel, Platen, Aragón-Calvo, et al. 2012) increased this

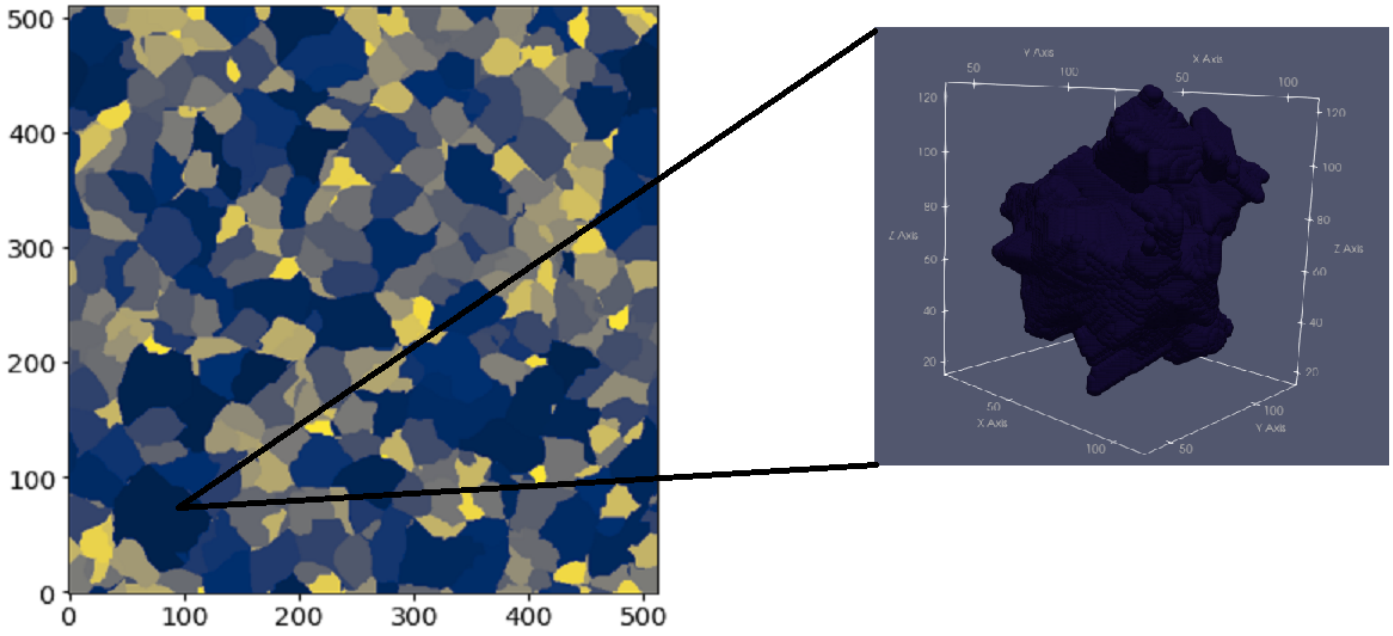

Figure 3.2: Voids identified by the Watershed Void Finder. The zoom-in shows a 3D perspective of one of the voids.

number up to 55 void galaxies. As it was discussed in Chapter 1.7. all these galaxies showed significant different properties than galaxies located in the field.

An important development of the Watershed Void Finder has been brought by Matthijs 2003. In his thesis, the author extended the original WVF into a Multiscale Watershed Void Finder (MWVF). The improvement lies in the use of filters with progressively smaller radii that will preserve the hierarchical buildup of the void population (Fig. 3.5).

The WVF is not the sole algorithm based on the watershed transform. In fact, at the present moment, this operation represents the main method used in efficient void finding algorithms . For example, ZOBOV (Neyrinck 2008) also makes use of the watershed transform in identifying depressions in the density field. The main difference between the WVF and ZOBOV is that the later is based on the Voronoi tesselation procedure to estimate densities while the former uses DTFE for the density reconstruction (for a detailed description of the DTFE see Section 3.3). Another difference lies in the fact that ZOBOV uses a statistical criterion based on the minimum density to decide on the significance of watershed basins while the WVF has a geometric filtering algorithm. The reader interested in comparing the efficiency of various void finding algorithms can visit the work of Colberg, Pearce, et al. 2008. An extension of the ZOBOV algorithm, known as VIDE, has been developed by Sutter, Lavaux, Hamaus, et al. 2015. The modifications consist in increased speed and ability to work on different observational survey geometries in the context of the watershed framework.

In this section, we discussed the Watershed Void Finder, the algorithm used in this work to identify voids in the density field. We described the watershed transform, the main operation used to efficiently identify voids, improvements of the WVF and alternative void finding algorithms developed in the literature. In the next section, we focus on N-body simulations. Specifically, we discuss the GADGET-2 simulation and detail its gravitational algorithm.

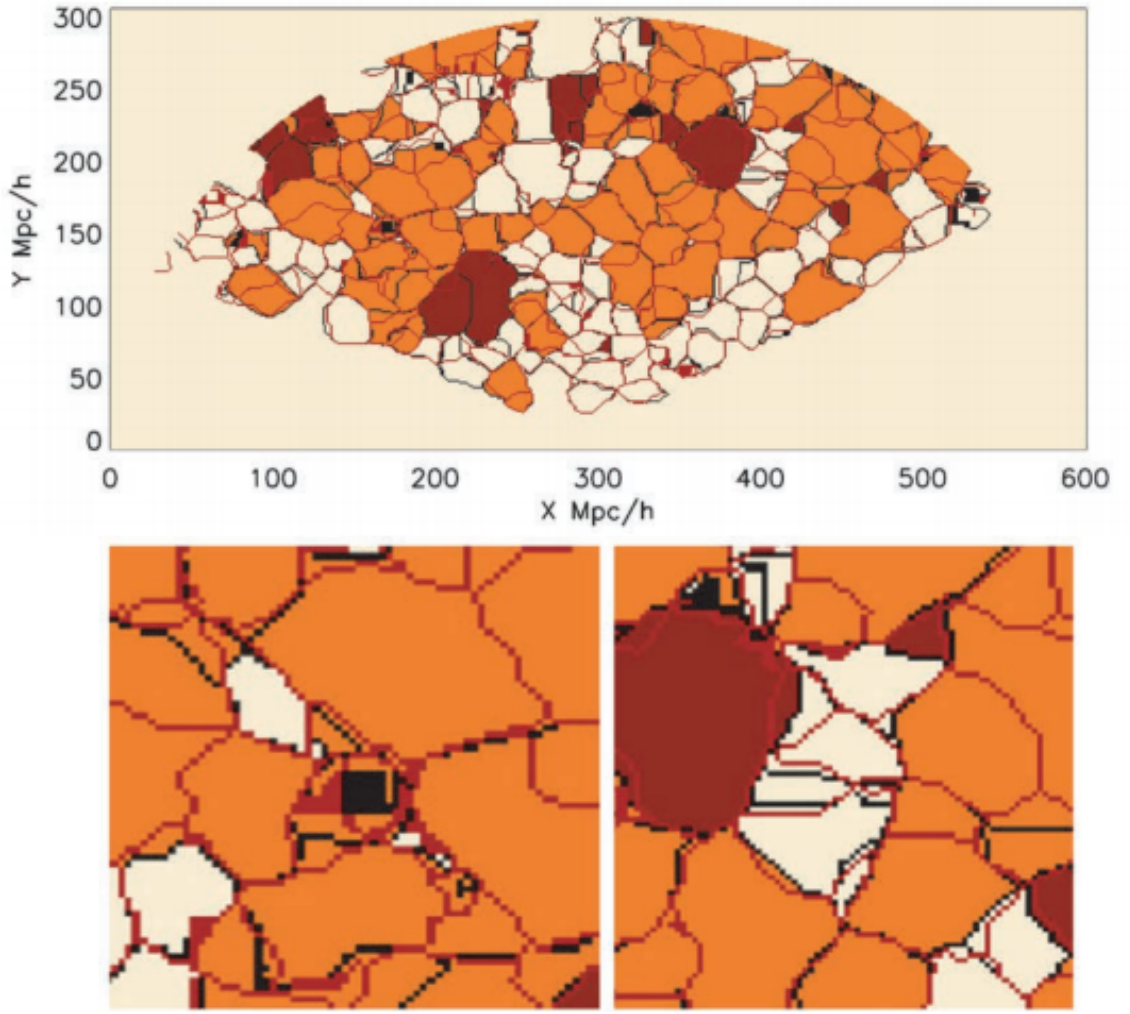

Figure 3.3: *Top*: Comparison between the WVF segmentation boundaries of the SDSS mock sample (in red) and the ones of the magnitude sample (in black). The segment colours shows the topological errors. Orange corresponds to false mergers while red corresponds to false splits. *Bottom*: Two panels show zoom-ins of mismatch between the two WVF segmentations. Figure from Platen, van de Weygaert, Jones, et al. 2011.

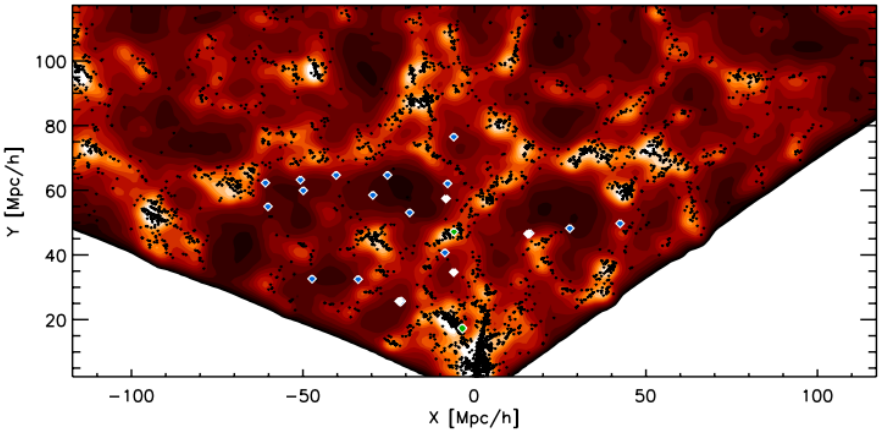

Figure 3.4: Density map and galaxies redshift survey region of SDSS from which galaxies for the Void Galaxy Survey were selected. The slice has a thickness of $4h^{-1}$ Mpc. The dark red corresponds to low void densities while the colour beige corresponds to average cosmic density. The black dots represent SDSS galaxies. The white diamonds show the initial sample of voids galaxies while the blue ones show the void galaxies from the full Void Galaxy Survey. Green diamonds correspond to a control sample.

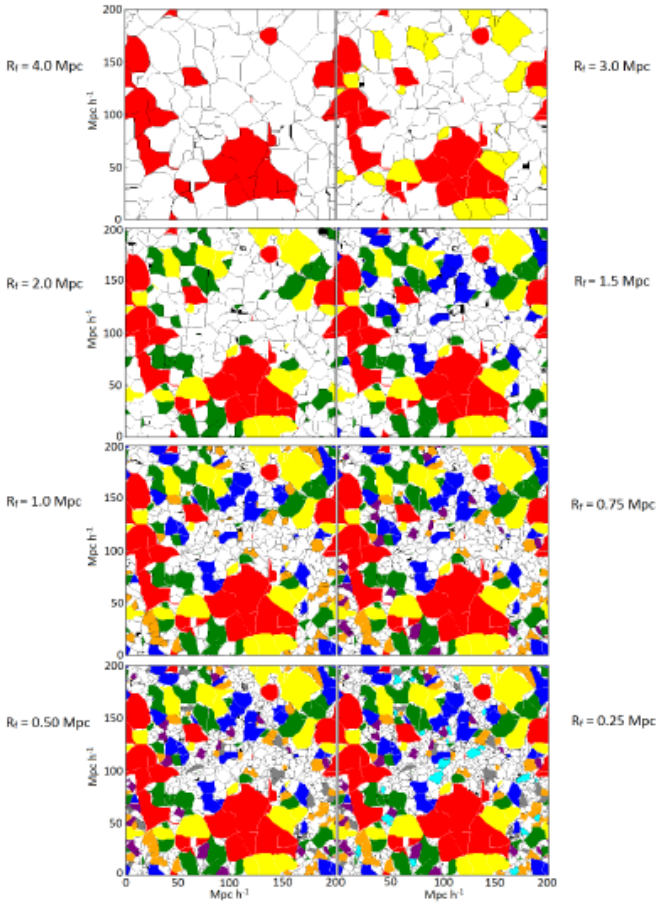

Figure 3.5: The MWVF procedure. Voids at progressively smaller filter radii R_f are added to the void population based on an emptiness criterion. Figure from Matthijs 2003.

3.2 Cosmological N-body simulations

The structure in the cosmic web formed as a consequence of gravitational amplification of small density perturbations. The growth of fluctuations is accompanied by other physical processes such as: gas dynamics, radiative transfer and photoionization. The equations governing these processes are non-linear in nature and require numerical simulations in order to accurately describe them.

The first N-body simulation was performed by Holmberg 1941 and it involved the study of the tidal deformation of two galaxies resulting from their gravitational interaction. In order to simulate the effect of gravity, the stars which build up the galaxies were represented as 37 light bulbs. Since their measured flux obeys the inverse square law, it was considered to be a good approximation of the gravitational force.

However, it would take more than 30 years until Press and Schechter 1974 performed the first cosmological simulation. The results of the 1000 bodies indicated, for the first time, the hierarchical clustering of matter at the large scale. Ever since, N-body simulations have the main use in testing cosmological models (such as the ΛCDM) and investigating how the formation of structure, from the linear stages in the early Universe up to the late non-linear stages, took place. A review of the techniques used to study the formation of the large scale structure has been written by Efstathiou et al. 1985.

In the following subsections, we will discuss the main principles of N-body simulations. Concretely, we will focus on the GADGET-2 simulation (Springel 2005) and describe its gravitational algorithms.

3.2.1 Governing principles

The main principle governing the cosmological simulations assumes that dark matter is discretized using particles which sample the phase space. Concretely, a particle moves in the gravitational field produced by all the other particles and evolves in time according to Newton's laws written in comoving coordinates (Eq. 3.1, 3.2 and 3.3). The first two equations must be integrated for each particle in the simulation, which will lead to a number of 6N differential equations. Note that the structure formation is primarily dictated by gravity so no additional effects such as hydrodynamics of the baryonic gas or radiative effects are to be considered.

$$\frac{d\mathbf{x}}{dt} = \frac{\mathbf{v}}{a} \tag{3.1}$$

$$\frac{d\mathbf{v}}{dt} + H\mathbf{v} = \mathbf{g} \tag{3.2}$$

$$\nabla \cdot \mathbf{g} = -4\pi G a[\rho(\mathbf{x}, t) - \bar{\rho}(t)] \tag{3.3}$$

In order to research the large structure (and substructure) in more detail, one has to increase the resolution of the N-body simulation. This requires a greater number of particles that will produce long running times of integration. As a consequence, the need for efficient algorithms (such as PM, P^3M and Tree PM) came by. Such algorithms could compute the gravitational force between the particles more easily.

3.2.2 GADGET-2

The GADGET simulation (Springel, Yoshida, and White 2001; Springel 2005; V. Springel et al. 2008; Springel, Pakmor, et al. 2021) is a TreeSPH cosmological simulation code used to study

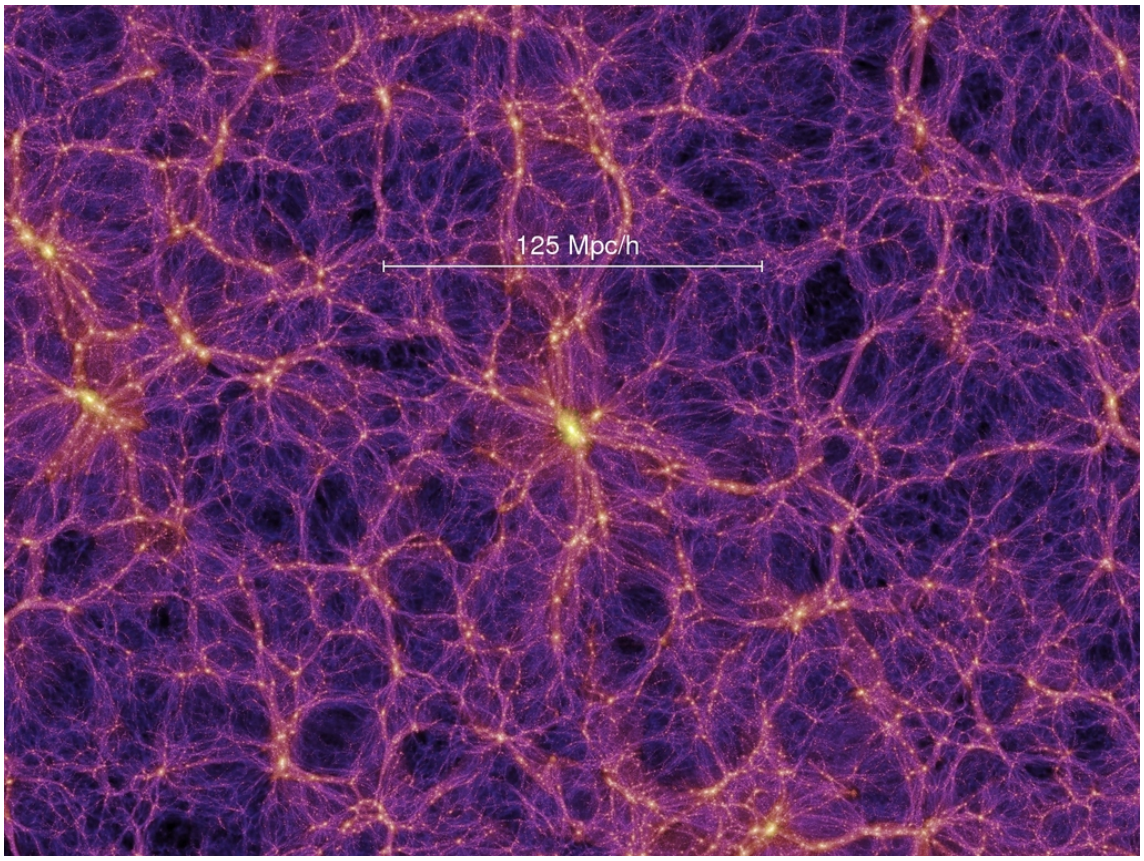

Figure 3.6: Cosmic structure formation in the Millenium simulation, a customised version of the GADGET code. Credits to (Springel, Yoshida, and White 2001; Springel, White, Jenkins, et al. 2005).

the structure formation processes in the Universe (Fig. 3.6). GADGET permits simulations with both a colisionless component (dark matter or stars in galaxies) and of an ideal gas (baryonic, mostly hydrogen and helium).

In this work, we use the second instalment of the simulation, GADGET-2 (Springel 2005). This code uses a TreePM algorithm in order to compute the gravitational forces. The short-range forces are calculated using the Tree method while the long-range forces are established using Fourier techniques. By contrast, the gas dynamics are computed using smoothed particle hydrodynamics (SPH). As the focus of this work was on dark matter simulations of the large scale structure, the SPH method will not be detailed further. In the following section, details on the TreePM algorithm and other features of the code will be discussed.

3.2.3 Gravitational algorithms

The Tree algorithm

Computing the gravitational forces at the large scale presents issues due to its long range nature. As mentioned before, investigating a large number of particles will result into a N^2 number of calculations which produces slow times of integration.

One way to combat this problem is to group distant particles together and calculate their hierarchical multipole expansion (this is known as a tree algorithm). The idea is that we do not need to compute the *individual* gravitational force for particles located at large distances. As

such, the Tree algorithm decomposes the gravitational field depending on the accuracy of the multipole expansion computation.

Quantitatively, this can be done by continuously subdividing the simulation space in which the particles reside into daughter nodes with side lengths half of the original cube until each cube contains at least one particle - the leaves of the tree (Fig 3.7). The forces are then calculated by "walking" the tree. From the trunk node, a decision is made based on the following question: is the multipole expansion a good enough approximation of the gravitational force? If the answer is positive, the multipole expansion is used and the "walk" on that particular node ends. If the answer is negative, the node at the branch opens up and the daughter nodes are considered. This type of tree algorithm is known as the Barnes-Hut oct-tree (Barnes and Hut 1986). The advantage of this technique is that instead of needing N-1 force terms per particle, the gravitational force on a single particle will require only $\log N$ interactions.

In order to compute the gravitational force, consider the potential at a position r of a particle j of mass m in a particle distribution where N is the number of particles:

$$\Phi(\mathbf{r}) = -G\sum_{j=1}^{N}\frac{m_j}{\mathbf{r}-\mathbf{x}_j} \tag{3.4}$$

We can expand

$$\frac{1}{\mathbf{r}-\mathbf{x}_j} = \frac{1}{\mathbf{y}+\mathbf{s}-\mathbf{x}_j} = \frac{1}{|y|} - \frac{\mathbf{y}\cdot(\mathbf{s}-\mathbf{x}_j)}{|y|^3} + \frac{1}{2}\frac{\mathbf{y}^T[3(\mathbf{s}-\mathbf{x}_i)((\mathbf{s}-\mathbf{x}_i)^T - \mathbf{I}(\mathbf{s}-\mathbf{x}_i)^2]}{|\mathbf{y}|^5} + ... \tag{3.5}$$

where $\mathbf{y} = \mathbf{r} - \mathbf{s}$ and the dipole term vanishes due to the summation over all the particles in the group. The multipole moments can be computed for each node of the tree resulting into a gravitational potential expression

$$\Phi(\mathbf{r}) = -G\left[\frac{M}{|\mathbf{y}|} + \frac{1}{2}\frac{\mathbf{y}^T\mathbf{Q}\mathbf{y}}{|\mathbf{y}|^5}\right] \tag{3.6}$$

where M is the monopole moment and Q is the quadrupole tensor. As such, computing the gravitational force on a particle will not require to compute N single particle forces but instead the order of the calculation will be of $\log N$ multipoles.

The particle mesh (PM)

Another method used to compute the gravitational potential is the particle mesh (PM) technique. This algorithm is computed on a computational grid and it determines for each particle in the distribution the density at each grid point based on the neighbouring particles. The gravitational potential can then be obtained by solving the Poisson's equation. This equation is solved in real space by considering a convolution of the density field $\rho(\mathbf{x'})$ with a Green's function $g(\mathbf{x})$ $\propto \frac{1}{k^2}$:

$$\Phi(\mathbf{x}) = \int g(\mathbf{x}-\mathbf{x'})\rho(\mathbf{x'})d\mathbf{x'} \tag{3.7}$$

According to Parseval's theorem, the Fourier transform is unitary which implies that in Fourier space, the convolution between the Green's function and the density field becomes a simple product:

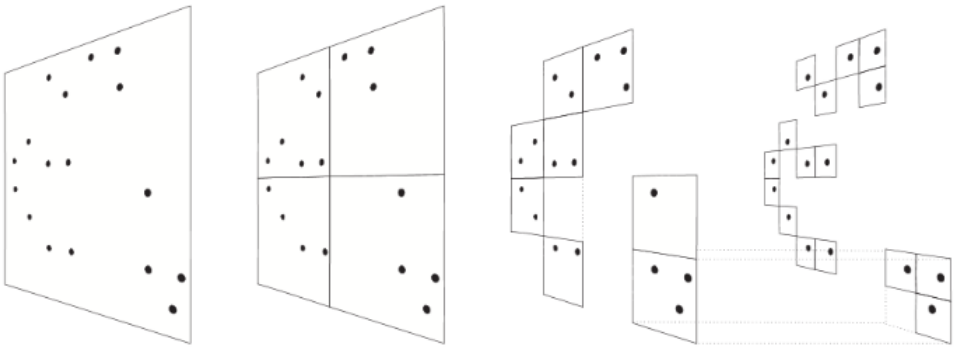

Figure 3.7: Illustration of the Tree algorithm. The space is continuously subdivided until each cell contains at least one. particle. Figure from Springel, Yoshida, and White 2001.

$$\hat{\Phi}(\mathbf{k}) = \hat{g}(\mathbf{k}) \cdot \hat{\rho}(\mathbf{k}) \tag{3.8}$$

The potential is then obtained by performing a fast Fourier transformation again into real space. Working in Fourier space thus makes the PM technique very fast, reducing the number of calculations to the order of NlogN. However, despite the PM's advantages of simplicity and speed, the resolution is limited to the mesh size.

The TreePM

The GADGET-2 algorithm uses the treePM method which combines the advantages of the previous two techniques. The idea of treePM is to split the potential, in Fourier space, into a long range and a short range component and compute them individually using the PM and tree algorithms respectively:

$$\Phi_{\mathbf{k}} = \Phi_{\mathbf{k}}^{long} + \Phi_{\mathbf{k}}^{short} \tag{3.9}$$

$$\Phi_{\mathbf{k}}^{long} = \Phi_{\mathbf{k}} \exp(-\mathbf{k}^2 r_s^2) -> PM \tag{3.10}$$

$$\Phi_{\mathbf{k}}^{short} = \Phi_{\mathbf{k}}[1 - \exp(-\mathbf{k}^2 r_s^2)] -> tree \tag{3.11}$$

where exponential factors are used to suppress the long and short range potential below some scale r_s. In other words, in the case of the $\Phi_{\mathbf{k}}^{long}$ computed by PM, if r_s is chosen larger than the mesh scale, then the force anisotropies will be suppressed. Similarly, r_s has the role to suppress the force for large distances in the potential $\Phi_{\mathbf{k}}^{short}$ computed via the Tree algorithm.

The advantage of combining both methods arises from the way algorithms compensate for one another. The Tree algorithm becomes slow when dealing with mass distributions that have a low density contrast. By comparison, in the PM algorithm, the efficiency in computing the gravitational field decreases at small scales and thus makes it inadequate in high spatial resolution simulations.

3.2.4 Simulation parameters

The simulation parameters used in this work are listed in Table 3.1. These parameters are inferred from the Seven-year Wilkinson Microwave Anisotropy Probe (WMAP) (Jarosik et al. 2011) temperature and polarization observations.

Number of particles	512^3
Boxsize	300 Mpc
Redshift	0
Energy density matter Ω_0	0.272
Energy density dark energy Ω_Λ	0.728
Hubble parameter H	70.4 km s^{-1} Mpc^{-1}

Table 3.1: Values for the simulation parameters used in this work

3.3 Simulation processing: DTFE

In order to obtain the density field of the particle distribution, the Delaunay Tessellation Field Estimator (DTFE) (W. E. Schaap and van de Weygaert 2000, Cautun and van de Weygaert 2011) has been used. The DTFE is an algorithm used to reconstruct the underlying density field from a sample of discrete data points. There are several advantages for using this algorithm which include its ability to retain the anisotropy of the particle distribution and to preserve the hierarchical structure of the mass distribution. Furthermore, it does not suffer from the disadvantage of depending on any pre-specified filtering which would dilute these properties.

The first step in obtaining a continuous field is the Voronoi tessellation. This technique represents the generalization in multidimensional space of partitioning into bins a one dimensional space. In this case, the space is divided into disjunct convex polyhedral cells (Fig. 3.8). Physical discontinuities at the boundaries of the polyhedra can appear due to this discretization. To eliminate them, one has to linearly interpolate the sampling points (Delaunay tessellation). This tessellation is realised by splitting the space into triangles (or tetrahedra in 3-dimensions) with the property that no vertex lies inside the circumscribe circle (or sphere). From the figure, one can notice that the Voronoi and Delaunay tessellations are closely linked: the centre of each circumcircle in the Delaunay tetrahedron is a vertex of a Voronoi cell and the vertices of the Delaunay cells are the centers in the Voronoi tessellation cells.

In order to obtain the density estimate of a particle distribution, one has to divide by the normalized volume of the contiguous Voronoy cell, $V(W_i)$, as to assure mass conservation:

$$\rho(x_i) = \frac{m(1+N)}{V(W_i)} \tag{3.12}$$

where N represents the number of particles located at positions x_1, x_2, ..., x_N that defines the contiguous Voronoi cell while m is the equal mass of the particles.

After computing density estimates at the vertices of a Delaunay tetrahedron, one can obtain the volume-covering density field by linearly interpolating:

$$\rho(\mathbf{x}) = \rho(\mathbf{x}_0) + \nabla\rho(\mathbf{x}_0) \cdot (\mathbf{x} - \mathbf{x}_0) \tag{3.13}$$

where $\nabla\rho(\mathbf{x}_0)$ is the estimated constant density field gradient within the tetrahedron.

A slice of the density field in the simulation can be seen in Fig. 3.9. We can visually identify the voids, as the dark patches in the slice, and the clusters and filaments located at their boundaries. Notice how the multiscale character of the particle distribution has been preserved. This can be easily seen when looking inside voids where the substructure is present. This consists out of small, tenous filaments which delimit other smaller subvoids. The hierarchical character is visible in filaments as well. Large, thick filaments branch themselves into smaller, thinner ones.

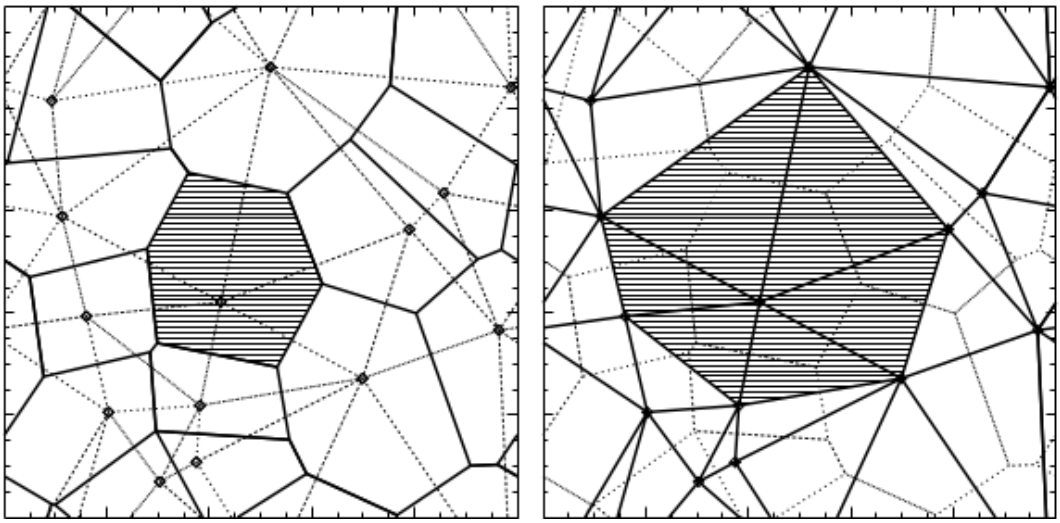

Figure 3.8: Left: Voronoi cells for a 2-dimensional point distribution. Shaded region corresponds to the point located below the center. Right: Delaunay tessellation for the same distribution. The shades region indicates the "contiguous Voronoi cell" of the same center point. Figure from W. E. Schaap 2007

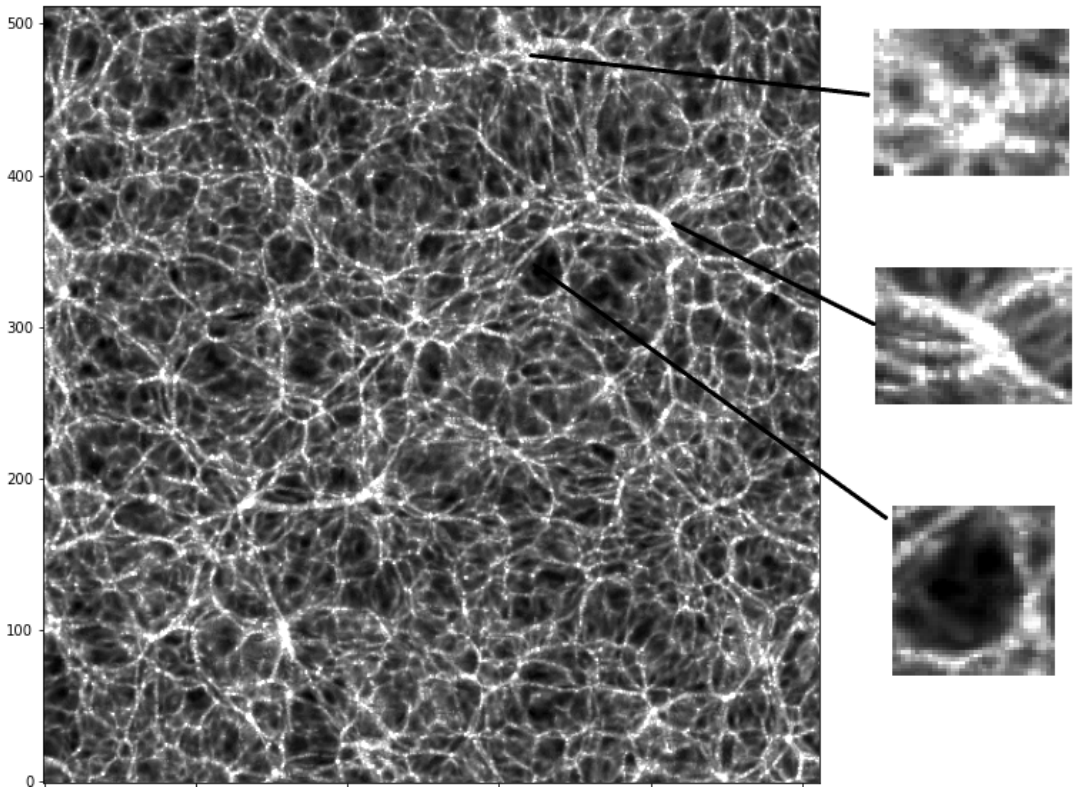

Figure 3.9: A slice through the density field in the GADGET-2 simulation used in this work. The zoom-ins show a visually identified cluster (top), a filaments (middle) and a void (bottom).

In a similar fashion, the DTFE method allows the calculation of cosmic velocity fields which, in turn, can be used to obtain the velocity divergence (see our results in Chapter 6), shear and vorticities.

To obtain the velocity field from a discrete set of points, the DTFE linearly interpolates the velocity of the particles in the distribution (Bernardeau and van de Weygaert 1996; Romano-Dıaz and van de Weygaert 2007; van de Weygaert and Schaap 2009). Once the Delaunay tetrahedra have been defined as interpolation intervals, the components of the gradient velocity tensor $\frac{\partial v_i}{\partial x_j}$ are determined. These will be calculated from the values of the velocity field at each location $\mathbf{r}_0$, $\mathbf{r}_1$, $\mathbf{r}_2$ and $\mathbf{r}_3$ that defines the vertices:

$$\Delta v_{xn} = \frac{\partial v_x}{\partial x}\Delta x_n + \frac{\partial v_x}{\partial y}\Delta y_n + \frac{\partial v_x}{\partial z}\Delta z_n \tag{3.14}$$

$$\Delta v_{yn} = \frac{\partial v_y}{\partial x}\Delta x_n + \frac{\partial v_y}{\partial y}\Delta y_n + \frac{\partial v_y}{\partial z}\Delta z_n \tag{3.15}$$

$$\Delta v_{zn} = \frac{\partial v_z}{\partial x}\Delta x_n + \frac{\partial v_z}{\partial y}\Delta y_n + \frac{\partial v_z}{\partial z}\Delta z_n \tag{3.16}$$

where $\Delta x_n = x_n - x_0$, $\Delta y_n = y_n - y_0$ and $\Delta z_n = z_n - x_0$ for n = 1,2,3. Similarly, $\Delta v_{xn} = v_{xn} - v_{x0}$, $\Delta v_{yn} = v_{yn} - v_{y0}$ and $\Delta v_{zn} = v_{zn} - v_{z0}$.

Further on, the velocity gradient components are given by

$$\begin{pmatrix} \frac{\partial v_x}{\partial x} \\ \frac{\partial v_x}{\partial y} \\ \frac{\partial v_x}{\partial z} \end{pmatrix} = \mathbf{A}^{-1} \begin{pmatrix} \Delta v_{x1} \\ \Delta v_{x2} \\ \Delta v_{x3} \end{pmatrix} \tag{3.17}$$

$$\begin{pmatrix} \frac{\partial v_y}{\partial x} \\ \frac{\partial v_y}{\partial y} \\ \frac{\partial v_y}{\partial z} \end{pmatrix} = \mathbf{A}^{-1} \begin{pmatrix} \Delta v_{y1} \\ \Delta v_{y2} \\ \Delta v_{y3} \end{pmatrix} \tag{3.18}$$

$$\begin{pmatrix} \frac{\partial v_z}{\partial x} \\ \frac{\partial v_z}{\partial y} \\ \frac{\partial v_z}{\partial z} \end{pmatrix} = \mathbf{A}^{-1} \begin{pmatrix} \Delta v_{z1} \\ \Delta v_{z2} \\ \Delta v_{z3} \end{pmatrix} \tag{3.19}$$

$$\tag{3.20}$$

where $\mathbf{A}^{-1}$ is the inverse of the matrix

$$\mathbf{A} = \begin{pmatrix} \Delta x_1 & \Delta y_1 & \Delta z_1 \\ \Delta x_2 & \Delta y_2 & \Delta z_2 \\ \Delta x_3 & \Delta y_3 & \Delta z_3 \end{pmatrix} \tag{3.21}$$

Knowing the values of $\frac{\partial v_i}{\partial x_j}$ we can evaluate the velocity divergence θ, shear σ_{ij} and vorticity ω_{ij} :

$$\theta = \frac{1}{H}(\nabla \cdot \mathbf{v}) \tag{3.22}$$

$$\sigma_{ij} = \frac{1}{2}(\frac{\partial v_i}{\partial x_j} + \frac{\partial v_j}{\partial x_i}) - \frac{1}{3}(\nabla \cdot \mathbf{v}\delta_{ij}) \tag{3.23}$$

$$\omega_{ij} = \frac{1}{2}(\frac{\partial v_i}{\partial x_j} - \frac{\partial v_j}{\partial x_i}) \tag{3.24}$$

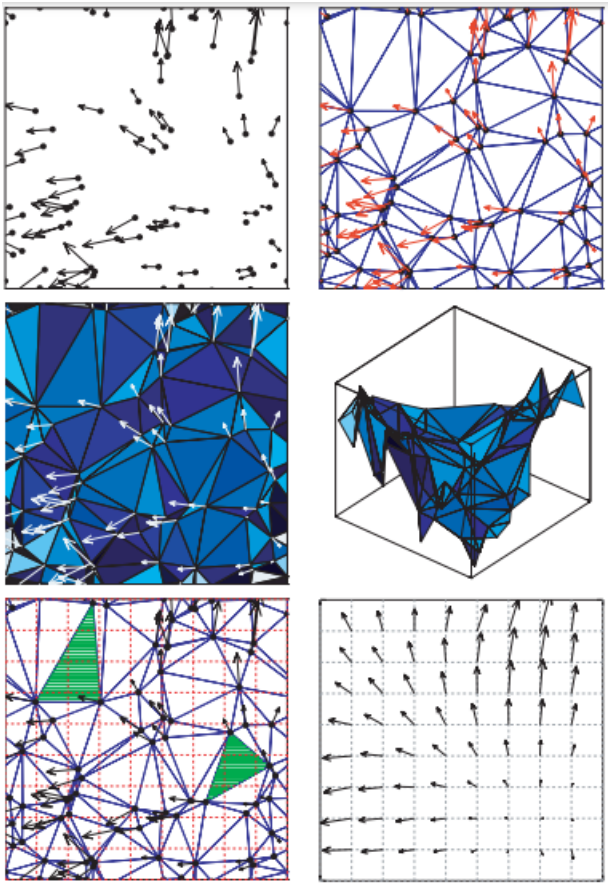

Figure 3.10: The velocity interpolation procedure obtained via the DTFE. The top left hand panel shows the particle positions of the velocity field while the top right panel shows the corresponding Delaunay triangulation. The middle panels show the velocity gradient determined for each triangle and the 3D representation. The velocity amplitude is represented through the height of each point. The bottom lefft panel shows the estimation of the DTFE velocity field at the grid points. The bottom right panel shows the final result of the interpolation procedure. Figure from Romano-Dıaz and van de Weygaert 2007.

An illustration of the Delaunay tesselation procedure used to infer the velocity field can be seen in Fig. 3.10. In Chapter 4.4 we will show the velocity fields and the stream of matter in our simulation.

In this section we presented the DTFE algorithm used to obtain the underlying density field in the particle distribution. Once this is obtained, the WVF can be used in order to identify the voids. In the next section, we focus on identifying halos in the simulation. We discuss the ROCKSTAR halo algorithm and the convex hull method used to specifically locate void halos.

3.4 Simulation processing: Halo identification

As we have seen in Chapter 2.4, halos are gravitationally bound clumps of dark matter that have virialized over time (Fig. 3.11). They are born from the collapse of overdensities in the primordial field and are essential in the formation of galaxies since they supply the gravitational potential wells in which baryons can fall into. The lack of electromagnetic interaction makes the

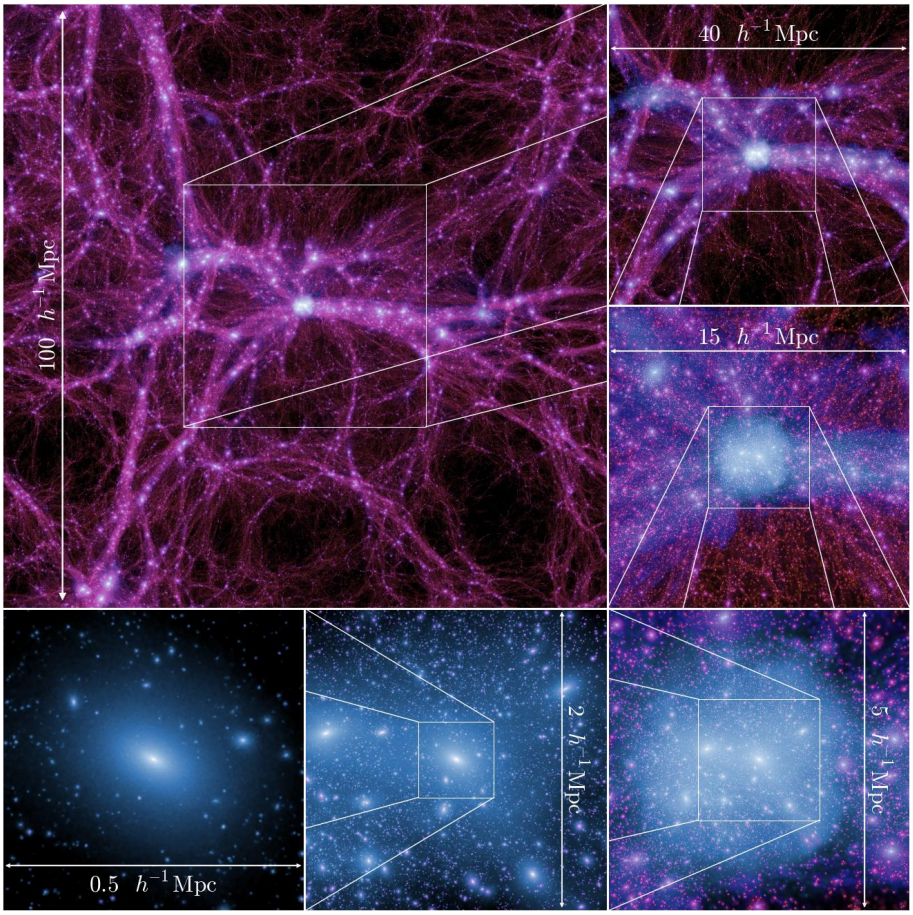

Figure 3.11: A zoom sequence onto the most massive halo in the dark matter distribution of the Millenium-II Simulation. The top left, largest image is a 15 h^{-1} Mpc thick slice through the 100 h^{-1} Mpc volume. The halo shown has a mass of $M_h = 8.2 \times 10^{14}\ h^{-1} M_{odot}$. Figure from Boylan-Kolchin et al. 2009

study of dark matter possible only through gravity. To obtain properties of the halos, such as masses, shapes, angular momenta or merging histories; post-processsing N-body simulations is needed. This requires developing algorithms that are capable of identifying halos in dark matter simulations.

3.4.1 Halo Finders

Previous halo finders that have been developed in the literature can be classified as bottom-up or top down finders.

Bottom-up Halo Finders

The main type of halo finder is the Friends-of-Friends (FOF) algorithm. This algorithm groups particles together provided they are located at a certain distance (linking length) from one another. Usually, this length is chosen as a fraction of the mean interparticle distance. The most efficient FOF algorithms used in the present are SUBFIND (Springel, White, Tormen, et al. 2001) and ROCKSTAR (Behroozi, Wechsler, and Wu 2013) which will be detailed in the next section. Extensions of this type of algorithm include phase-space finders such as 6DFOF

(Diemand, Kuhlen, and Madau 2006) and Hierarchical Structure Finder (Maciejewski et al. 2009).

Top-down Halo Finders

In the second category lies spherical overdensity (SO) finders. These algorithms identify density maxima in the particle distribution and collect particles around that peak in increasing spheres until their total mass falls below a certain density threshold. The most used top-down algorithm is the Amiga Halo Finder (AHF) (Knollmann and Knebe 2009). Some other examples include the ASHF (Planelles and Quilis 2010) and the Bound Density Maxima (Klypin et al. 1999).

Limitations

Limitations of the halo-finders that use only three dimensions usually involve the inability to correctly identify major mergers and halos that reside too close to their parent halo. The common reason has to do with the insufficient density contrast that would allow one to separate close-by halos. Despite the fact that this problem can be solved by investigating the 6D phase space, limitations can also arise in this case as well. This time, the problem is related to the lack of a position-velocity metric. More details on more halo finders codes and their efficiency in retrieving properties of mock halos can be found in Knebe et al. 2011.

3.4.2 Rockstar Halo Finder

The ROCKSTAR (Robust Overdensity Calculation using K-space Topologically Adaptive Refinement) Halo Finder, developed by Behroozi, Wechsler, and Wu 2013, is an adaptive phase-space temporal halo-finder, able to preserve the particle-halo and halo-subhalo identities at various time steps. Moreover, the algorithm can easily adapt to the high-resolution simulations due to its efficiency and parallelization. The algorithm steps are summarized here (see also Fig. 3.12 for a visual representation of the steps).

1. Rockstar identifies overdense regions in the simulation via 3D FOF and splits the task among multiple processors for analysis. In the original 3D FOF, if a particle has reached a certain number of "friends" (neighbours) within the linking length, then the neighbour finding process is terminated. By contrast, the Rockstar algorithm searches for neighbours located inside twice the linking length and, if these neighbours correspond to other FOF groups, the two groups are merged. This technique is used in order to speed up the process of neighbour-finding.

2. In phase space, a hierarchy of FOF subgroups are constructed by reducing the 6D linking length. This means that for two particles p_1 and p_2, the 6D metric is given by

$$d(p_1, p_2) = \left(\frac{|\mathbf{x}_1 - \mathbf{x}_2|^2}{\sigma_x^2} + \frac{|\mathbf{v}_1 - \mathbf{v}_2|^2}{\sigma_v^2} \right)^{\frac{1}{2}} \tag{3.25}$$

where σ_x and σ_v are the position and velocity dispersion of the particles in a particular FOF group. A linking length is then chosen such that a fraction f = 0.7 of the group particles are linked with at least another particle in subgroups. This operation is repeated for each subgroup such that deeper and deeper levels of substructure are sampled.

3. Starting from the bottom level of the hierarchy, a halo seed is generated at each local phase-space maxima, in each identified subgroup. The algorithm will then assign particles to the seed halo as it advances upwards on the hierarchical group scale. This will end when all the particles in the original FOF group will be collected.

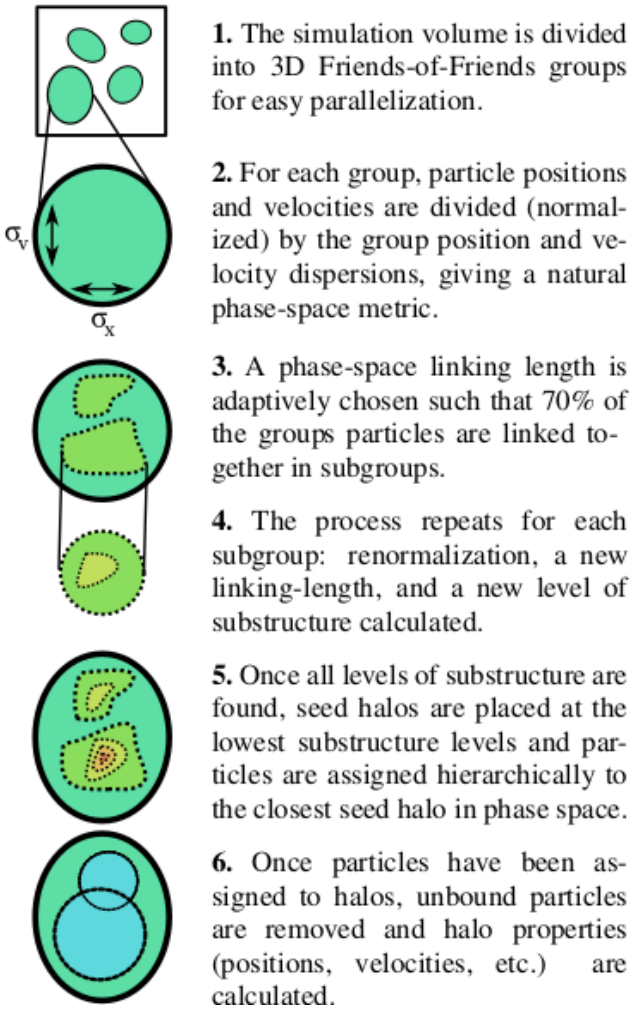

Figure 3.12: Steps that the Rockstar algorithm takes in the halo analysis. Figure from Behroozi, Wechsler, and Wu 2013.

Two cases must be now distinguished here. In the case of a parent group that has no other subgroups, all the particles present will be associated with the same seed halo. However, if the parent group contains multiple subgroups then the particles will be associated with the seed halos of those subgroups based on the shortest distance in phase-space. The phase-space metric will be based on halo properties such that the distance between a particle p and a halo h

$$d(h,p) = \left(\frac{|\mathbf{x}_h - \mathbf{x}_p|^2}{r_{vir}^2} + \frac{|\mathbf{v}_h - \mathbf{v}_p|^2}{\sigma_v^2} \right)^{\frac{1}{2}} \tag{3.26}$$

where r_{vir} is the virial radius of the seed halo and σ_v is the velocity dispersion of the particle.

4. If previous time steps are availabe, relations between halos/subhalos are computed.

5. Unbound particles from halos are eliminated and halo properties such as mass, shape or spin are computed. The unbinding method involves the computation of the particle potential via a Barnes-Hut tree algorithm.

A visual representation of the algorithm's ability to identify halos can be seen in Fig. 3.13. The image shows how particles are assigned to halos in a major merger event (example taken from the Bolshoi simulation at z = 0). A closer inspection shows that the larger halo contains another, smaller, merger. This event can be more clearly be seen in the velocity space in the bottom right panel.

3.4.3 Identifying halos in voids: the convex hull algorithm

We have seen that voids are anistropic structures, with complex boundaries that are difficult to pinpoint. In order to locate halos within voids, we have to find a suitable algorithm that would be able to correctly identify these boundaries. We turn to the convex hull algorithm (Barber, Dobkin, and Huhdanpaa 1996). To summarize, given a set of points in 3D, the convex hull finds the smallest polyhedron that encloses these points such that each point lies either on the boundary or inside the polyhedron. As an analogy, one can imagine a random distribution of sticks placed perpendicular on a table. A rubber band stretched around the outermost sticks represents the convex hull. Then, the void halo identification proceeds as follows:

i. Identify the positions of halos within spheres of increasing radii, centered on the void's center.

ii. Since voids are not perfectly spherical, the localising spheres will overflow the void at some particular radius (i.e will contain regions that are outside the void). As a consequence, halos that are not part of the void will be collected.

iii. Compute the convex hull of the void and keep only the halos that are *inside* the hull.

Fig. 3.14 illustrates the final step of the procedure. The density field at a particular slice is shown together with a cross-section of a void (yellow region). The yellow points represent the halo centers and tend to be found mostly in regions of high density (e.g filaments and clusters). The white line that surrounds the void represents the boundary of the convex hull (which we will refer to it from now on as simply the void boundary). The red dots are the halos that were identified inside the hull. In Fig. 3.15, we show a 3D perspective of the identified halos in an arbitrary void. The convex hull of the void is shown as a transparent polyhedra while the yellow spheres indicate the positions of the halo centers. Notice how most halos tend to be located at the void boundary. The center being mostly devoid of them.

Once the halos have been identified inside voids, we can investigate how various properties (number, mass, spin, shape) vary as a function of *radial* distance from the void's boundary (see Chapter 5 for results). This distance is computed in the following way

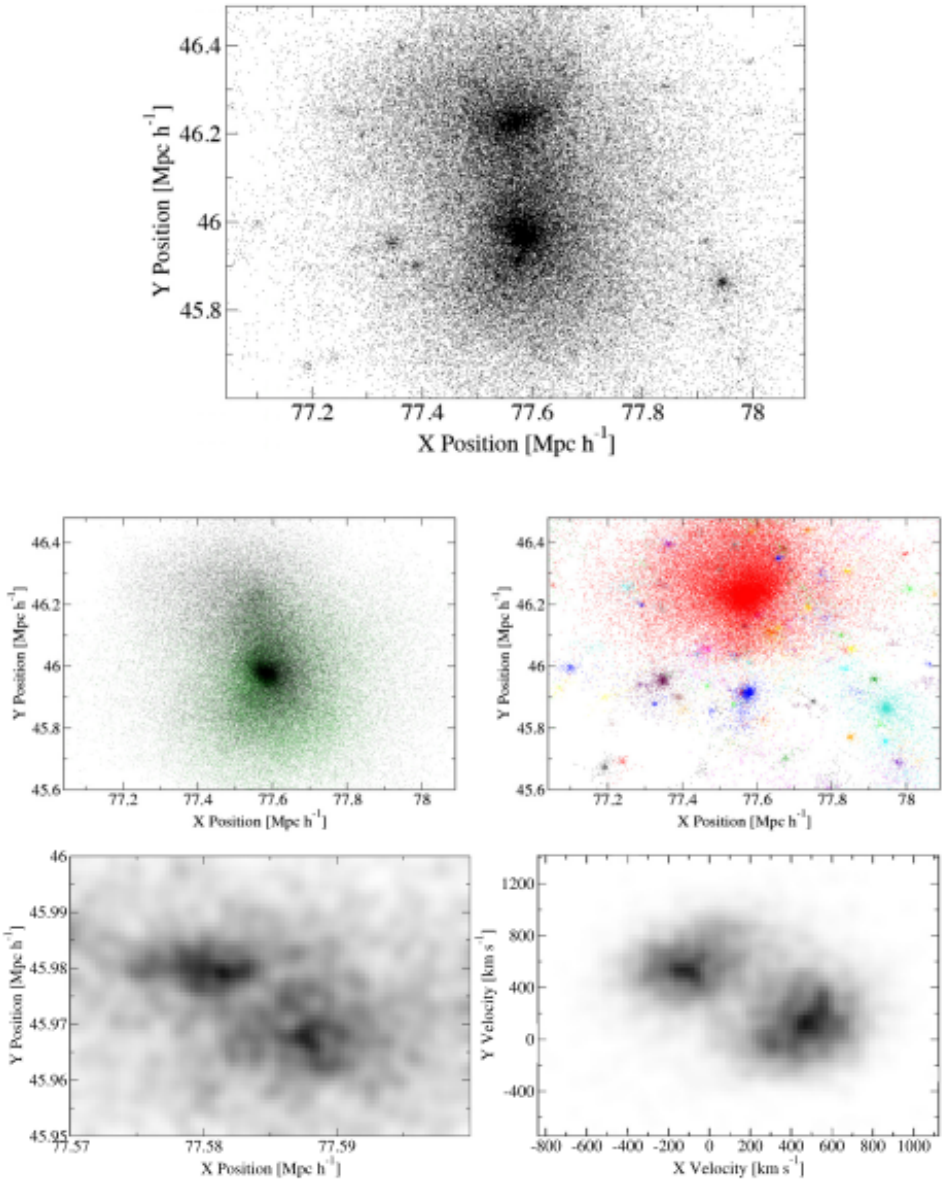

Figure 3.13: Halos in a major merger event in the Bolshoi simulation recovered by Rockstar. Top panel shows the particle distribution associated with the halos. The left panel in the second row shows the host halo particle distribution while the right one shows the subhalo particle distribution. It can be noticed that there are actually three halos involved in the major merger, two of them being very close together. The bottom panel shows this close merger in position and, more clearly distinguishable, in velocity space. Figure from Behroozi, Wechsler, and Wu 2013.

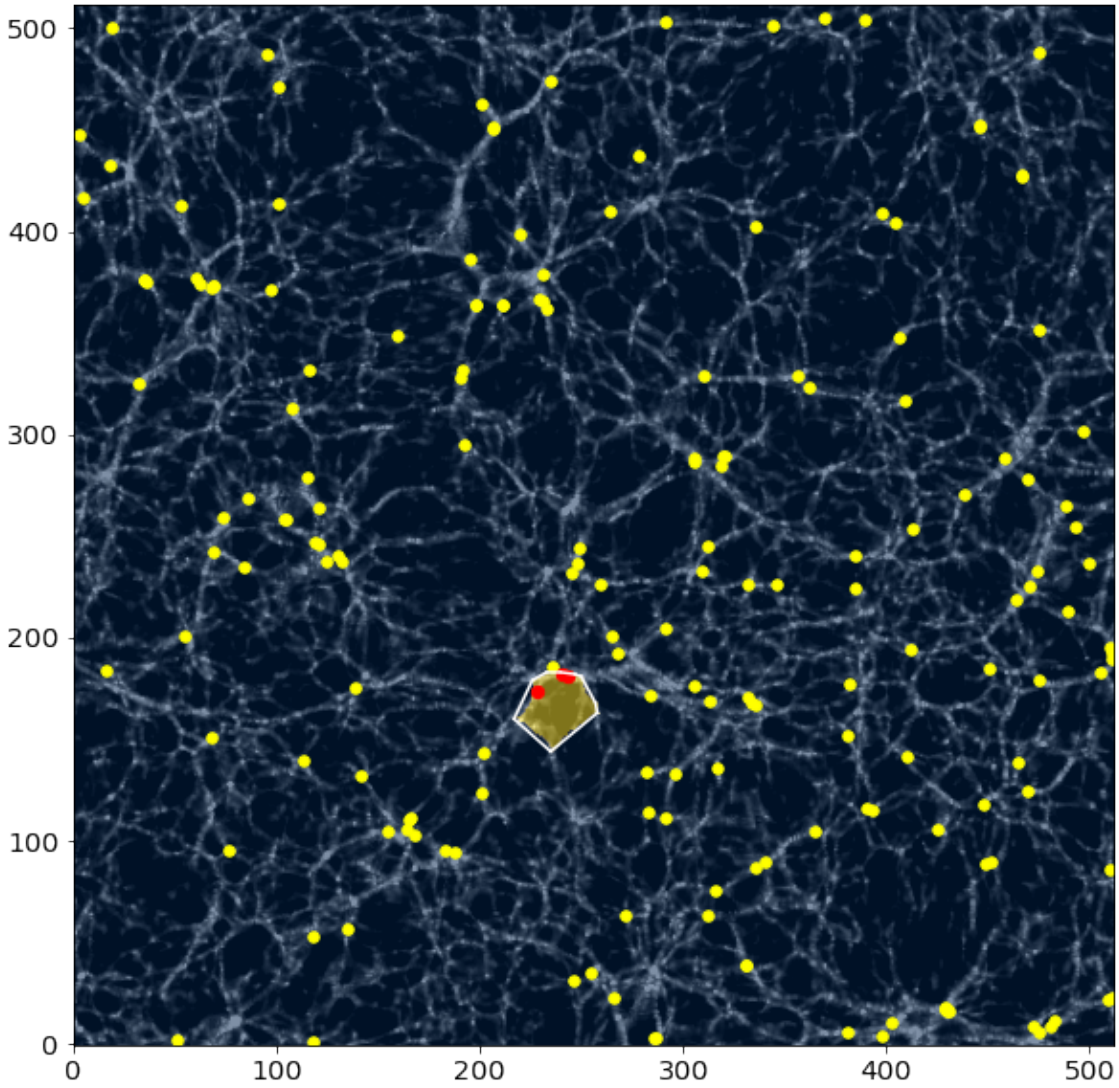

Figure 3.14: Cross-section of the density slice superposed over a void (yellow region) identified by the watershed algorithm. The white line surrounding the void represents the convex hull boundary. The yellow points indicate the halo center positions at that slice while the red points represent the halos identified inside the void.

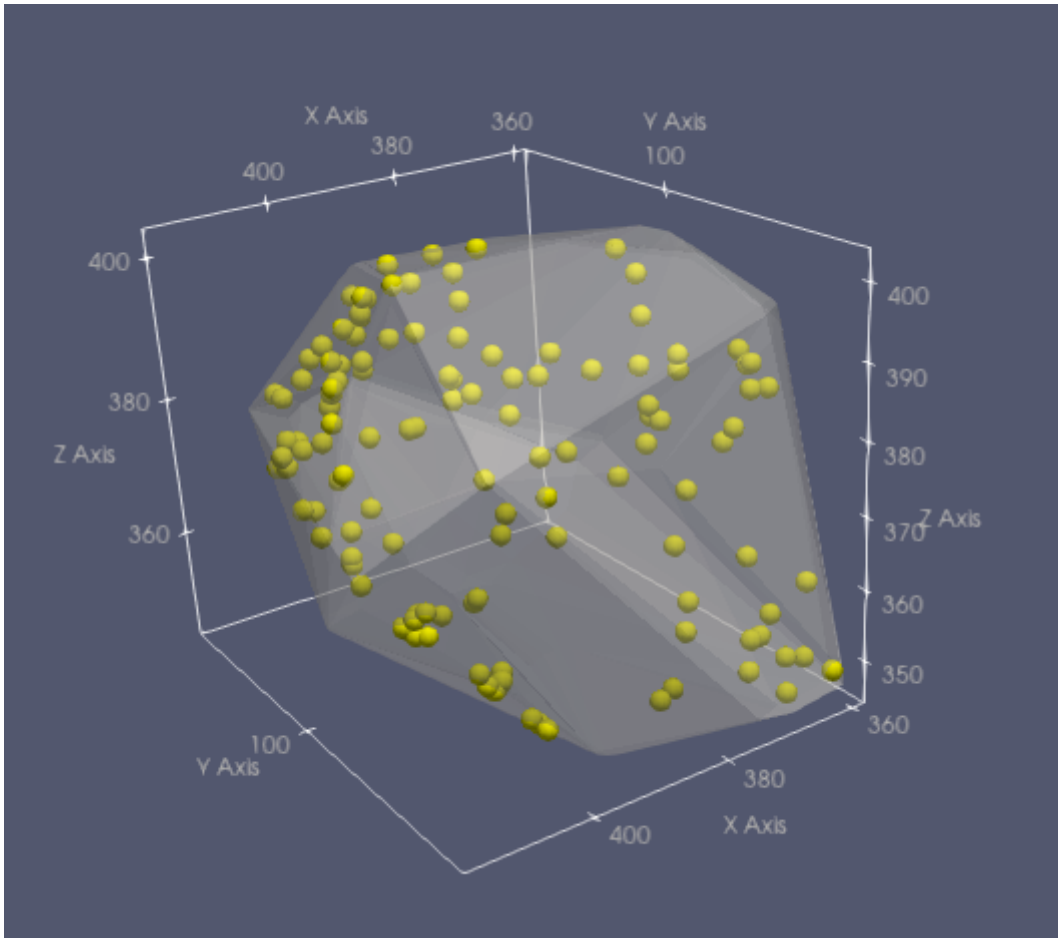

Figure 3.15: 3D perspective of identified halos in an arbitrary watershed void. The yellow spheres (not to scale) indicate the positions of the the halo centers. The translucent polyhedra represents the convex hull of the void.

$$D = min||\mathbf{r}_h - \{\mathbf{r}_b\}|| \tag{3.27}$$

where $||$ is the vector magnitude, $\mathbf{r}_h$ represents the position vector of a halo center, $\{\mathbf{r}_b\}$ represents the set containing the position vectors of all boundary points and D is the minimum distance between the halo center and the boundary points.

In this chapter we have seen the different tools employed to study the effect of the void environment on dark matter halos. In the next chapter, we present our results on the void population in the GADGET-2 simulation. We characterise the voids by their abundance, sizes, shapes and profiles.

Chapter 4

Void population

In this chapter we analyse the properties of the void population identified by the Watershed Void Finder in the GADGET-2 simulation. We first visually inspect the population and assess its abundance. We then define the center of a void, which will be useful in assessing the void profiles and shapes. Afterwards, we investigate the sizes and shapes of voids using the convex hull algorithm and compare those with the standard approaches. Subsequently, we present the radial density and velocity profiles and compare them with the predictions made by the linear theory. We use these results to characterise the void environment in which dark matter halos develop.

4.1 Void abundance

In order to characterise the void environment, we need to assess the statistical properties of voids through a representative sample. Using the WVF algorithm, we found a number of $\approx$ 3600 voids in the GADGET-2 simulation. Figure 4.1 shows a cross section of the density field (left panel), together with the corresponding watershed voids (middle panel). The colours are used to differentiate between voids; they do not correspond to any inherent physical property. Immediately one can notice the variety of sizes and shapes that the voids have. For a 3D representation of voids see top panel of Figure. 4.2 where we show three neighbouring voids. Each volume element has been represented by a sphere for better visualisation.

Looking back at Fig. 4.1 and focusing on the edges of the 2D slice of the central panel, one can notice a discontinuity of the watershed basins that continues on the opposite side: the voids appear split in two (see also bottom panel of Figure. 4.2 for the 3D perspective). This is an effect that results from the periodic boundary conditions of the simulation. Out of the total number of voids, 1000 (27%) are periodic voids. These voids may affect the results regarding shape, density and kinematics. As a consequence, they must be taken into account when analysing the various properties of voids. This can be done by translating the void coordinates towards the middle of the simulation. There, one can compute the desired properties.

Matthijs 2003 showed how the void abundance evolves with time. Using the self-developed multiscale filtering procedure, the author showed that voids reach a maximum at a $\approx = 0.8$. At lower values, the abundance increases exponentially from $a = 0$ while at higher values, the number of voids decreases. This decrease has been associated with void collapse or merging processes. For $a = 1$, the number of voids appears to coincide with our current findings of N $\approx$ 3600.

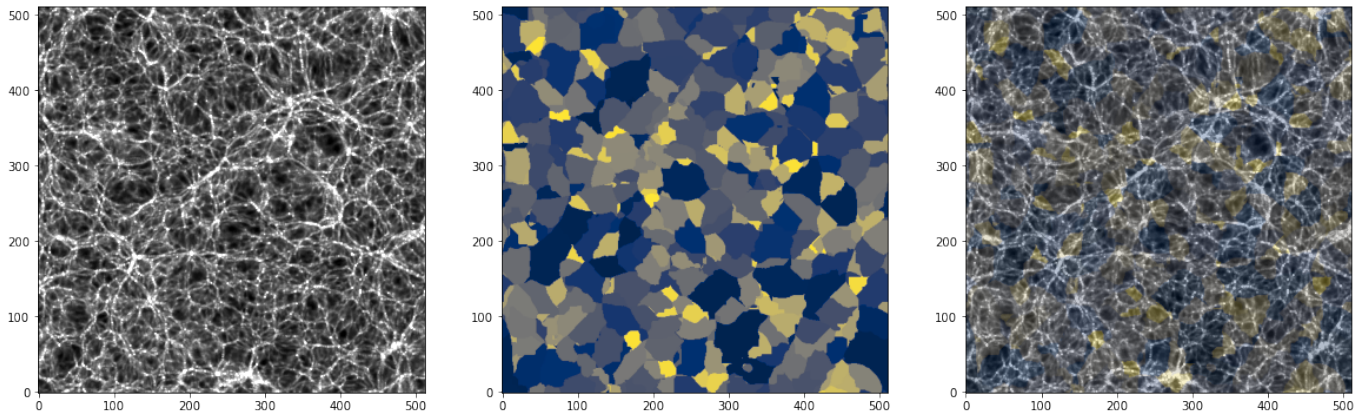

Figure 4.1: Left: Density slice in the simulation volume. Middle: corresponding voids identified with the WVF. The colours are used to differentiate the voids from one another. Right: superposition of the previous two images.

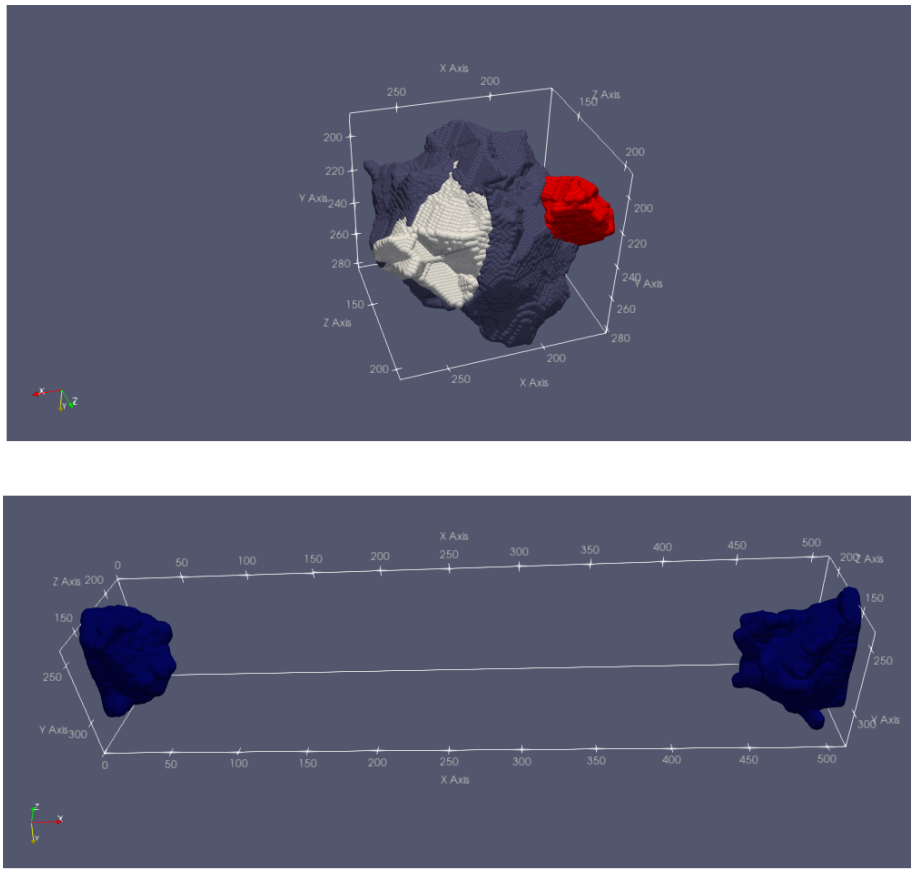

Figure 4.2: Top: A group of three neighbouring watershed voids in the GADGET-2 simulation. Bottom: A periodic watershed void in the GADGET-2 simulation. Due to the periodic boundary conditions of the box, the void appears split in two at the boundaries.

4.2 Void center

Identifying the center of a void is important for investigating various void properties and correlations. We have seen already that voids present a variety of irregular shapes (see also Section 4.4 in this chapter for our results). Due to this, identifying the center of a void may become an ambiguous task. The standard method used (Lavaux and Wandelt 2012; Sutter, Lavaux, Wandelt, et al. 2012) is to compute the volume weighted barycenter defined as:

$$\mathbf{r}_{bc} = \frac{\sum_{i=1}^{N_p} \mathbf{r}_i V_i}{\sum_{i=1}^{N_p} V_i} \tag{4.1}$$

where $\mathbf{r}_i$ is the position of the i-th particle, V_i is the volume of the Voronoi cell and N_p is the number of particles composing the void.

As noted by Nadathur and Hotchkiss 2015, the position $\mathbf{r}_i$ of a cell may in reality be imprecise. A factor responsible for this is the great number of void cells which reside in the overdense boundaries. This will cause the identified void center (Eq. 4.1) to be located far from the point of minimum density, which would represent a better choice as the center according to the authors.

In this work, we use an equivalent definition to that of Eq. 4.1 which is the density weighted center of mass defined as:

$$\mathbf{r}_{cm} = \frac{\sum_{i=1}^{N} \mathbf{r}_i \delta_i}{N} \tag{4.2}$$

where $\mathbf{r}_{cm} = \{\mathrm{x}_{cm}, \mathrm{y}_{cm}, \mathrm{z}_{cm}\}$ are the coordinates of the center of mass, $\mathbf{r}_i = \{\mathrm{x}, \mathrm{y}, \mathrm{z}\}$ are the coordinates of the voxels forming the void and δ_i is the density value at location $\mathbf{r}_i$. The sum runs over N voxels. In principle, these definitions are similar and should not produce different results.

In the later sections of this chapter we will use the center of mass as the origin of the void in computing the sizes, shapes and void profiles. In section 4.6 we will also discuss the dynamic center of a void, which will be useful in computing the velocity profiles.

4.3 Voids sizes

A primary characteristic in defining the environment is the size of voids. As a first approximation, the size of a void can be quantified by its spherical equivalent radius R. This is defined as the radius of a sphere that has the volume equal to the volume of the void. We consider the volume of a void V to be defined as:

$$V = \frac{N_{vv}}{N_{vs}} \times V_s = \frac{N_{vv}}{512^3} \times 300^3 \mathrm{Mpc}^3 \tag{4.3}$$

where N_{vv} is the number of voxels contained in a void, N_{tv} is the total number of voxels in the simulation and V_s is the volume of the simulation box. Then, the equivalent radius R is given by

$$R = \left(\frac{3}{4\pi} V\right)^{1/3} \tag{4.4}$$

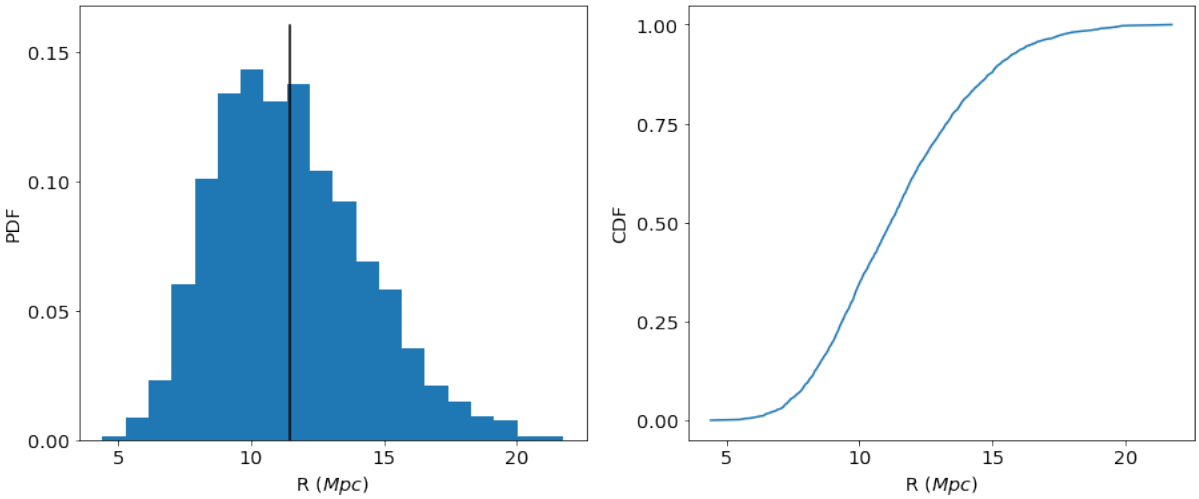

Figure 4.3: *Left*: Probability density of the equivalent void radii. The solid line indicates the average. *Right*: Cumulative distribution function of equivalent void radii.

Fig. 4.3 shows the equivalent radii of the voids in the current simulation. The void population spans an interval in radius between approximately 5 and 22.5 Mpc with an average radius of 11.45 Mpc.

We have seen previously that due to the tidal field generated by the surrounding structure, voids end up with irregular shapes and they can deviate substantially from what it is considered an ideal sphere. As such, we use the convex hull algorithm in order to approximate the lumpy boundaries of the voids. The size of a void can, thus, also be analyzed by computing the radial distance between the center and its boundary. Fig. 4.4 shows the distribution of the boundary-to-center distances of the voids. The first thing to notice is that the distribution spans a larger interval (5-35 Mpc) than the equivalent radius distribution. The average distance is 16.76 Mpc. We will refer to this value as the characteristic size of a void, r_{ch}.

The differences between the two distributions can be accounted by the fact that the convex hull algorithm better approximates the anisotropic shapes of voids while the equivalent radii method computes the radius of a void assuming that the void is spherical.

P. M. Sutter et al. 2012 has compiled a public void catalog using SDSS DR7 main sample (out to z = 0.2) and the luminous red galaxy (out to z = 0.44) sample. They computed the equivalent radii of their void population and found that it spans an interval between 5 to 135 h^{-1} Mpc. The wide interval in radii is explained as a consequence of various effects such as the bias of the brighter galaxies producing larger voids or possible shot noise enhancing void regions. Pan et al. 2012 also studied the distribution of voids using the SDSS DR7 using the VoidFinder algorithm. They found that voids have equivalent radii between 10 and 22 Mpc. In this case, the lack of voids smaller than 10 Mpc can be explained by the absence of a low-redshift sample. Nadathur 2016 has compiled a void catalogue using the Baryon Oscillation Spectroscopic Survey and found that the equivalent radii of their void population peaks at $\approx 35h^{-1}$Mpc. This value is confirmed by the more recent study of Kreisch et al. 2021, who applied the void finder VIDE on the QUIJOTE simulation and compiled the largest catalogue at the moment, containing over a billion voids.

We interpret the present results on the void sizes based on the studies mentioned. Thus, we attribute the differences in size mainly due to the tracer particles used. In this work, we identify voids based on the dark matter particle distribution. The particles trace out the voids much

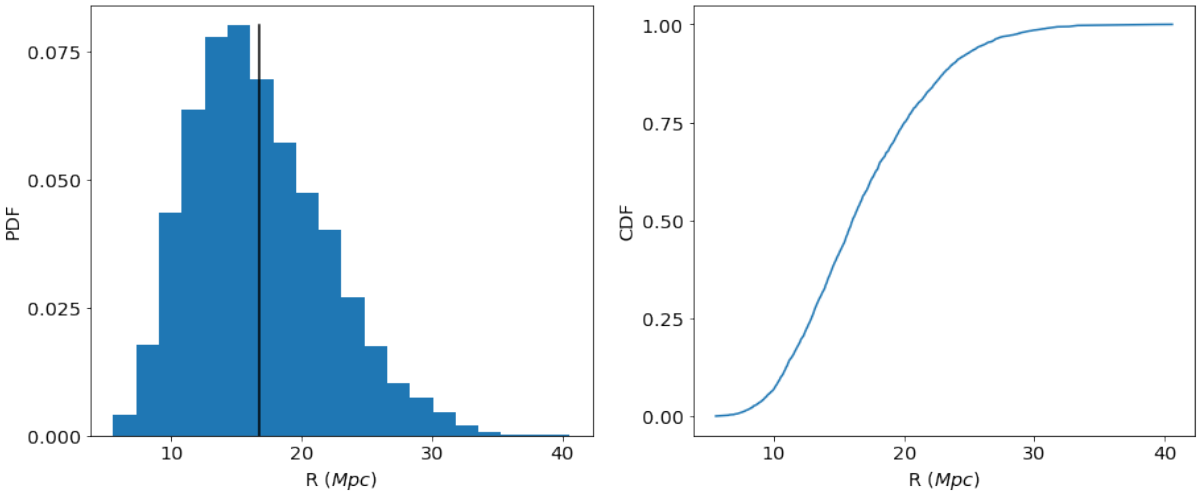

Figure 4.4: *Left*: Probability distribution function of the distances between the void boundaries and their centers. The black dashed / solid lines indicate the median / average boundary-to-center distances respectively. *Right*: Cumulative distribution function of the boundary-to-center distance.

accurately than galaxies (in observations: P. M. Sutter et al. 2012; Pan et al. 2012; Nadathur 2016) or simulations: Kreisch et al. 2021). The reason being that galaxies and halos represent a much sparser population of objects which will lead to voids with larger sizes. Particularly, in the case of Kreisch et al. 2021, the simulation resolution is another reason for the difference observed. Concretely, they report that the lack of small voids in their sample is due to the low resolution at small scales.

We relate now our results to the theoretical predictions from the literature. The 2-barrier excursion set formalism, developed by Sheth and van de Weygaert 2004, has predicted a universal void size distribution. This distribution is sensible to the ratio between the collapse barrier and the void barrier, $\frac{\delta_c}{\delta_v}$. This shows that the probability of voids being crushed by overdensities (recall the void-in-cloud phenomena from Chapter 1.6) increases as the collapse barrier decreases. As a consequence, the size distribution will suffer a cut-off of small voids due to the void collapse processes. By contrast, the population of large voids is not affected by this and only depends upon δ_v. The analytical size estimation found in the 2-barrier formalism is given by:

$$\frac{r_v}{h^{-1}Mpc} \approx 1.7 \times \frac{8}{3^{2/3+n}} \left(\frac{\sigma_8}{0.9} \frac{2.7}{|\delta_v|}) \right) \tag{4.5}$$

where r_v is the size of a void, σ_8 is the rms fluctuation on scales of 8 $h^{-}1$ Mpc in the power spectrum while n is the power spectrum index. For an initial power spectrum $P(k) \propto \mathrm{k}^n$ with n = -1.5, σ_8 = 0.9 and δ_v = -2.81, the authors found that the typical void radius is $\approx 3\ h^{-1}$ Mpc. This is almost an order of magnitude lower than what the present study found. This discrepancy may appear due to the way the definition of a void in a theoretical framework differs from the one in a practical scenario. As noted by Nadathur and Hotchkiss 2015, in the model of Sheth and van de Weygaert 2004, a void represents a non-linear underdense region that has reached shell-crossing. However, in N-body simulations (or redshift survey data) algorithms are used to identify underdense regions in the field. These algorithms do not refer to the shell crossing criterion, which is the main assumption that enters the definition of a void in the theoretical

model. Ideally, one would have to find a way to relate the model predictions with practical results. One solution proposed by Nadathur and Hotchkiss 2015 would be to assume that shell-crossing and void formation develop at smaller density values δ_v than those predicted by the spherical model. By allowing this value to vary, one can permit the inclusion of larger voids via an exponential cut-off. However, further research into the issue is required in order to develop a better agreement.

4.4 Voids shapes

One method to analyse the shapes of voids is to fit them with an ellipsoid. In order to do this, the shape tensor $\mathbf{S}_{ij}$ must be computed:

$$\mathbf{S}_{ij} = -\sum_k x_{ki} x_{kj} \tag{4.6}$$

$$\mathbf{S}_{ii} = -\sum_k \mathbf{x}_k^2 - x_{ki}^2 \tag{4.7}$$

where $\mathbf{x}_k$ is the position of the k-th volume element of a void with respect to the void center of mass (that is $\mathbf{x}_k$ = $\mathbf{r}_k$ - $\mathbf{r}_{cm}$).

The semiaxes of the ellipsoid can be obtained by solving for the eigenvalues of the shape tensor $\mathbf{S}_{ij}$. The eigenvalues must satisfy the condition $a > b > c$. The lengths of the semiaxes of the ellipsoid are thus given by:

$$a^2 = \frac{5}{2N}(b + c - a) \tag{4.8}$$

$$b^2 = \frac{5}{2N}(a + c - b) \tag{4.9}$$

$$c^2 = \frac{5}{2N}(a + b - c) \tag{4.10}$$

where N represents the total number of volume elements comprising the void.

Once the axes have been obtained, the shape of the void ellipsoid can be quantified by computing the ratios $\frac{b}{a}$ and $\frac{c}{a}$. Three cases must be distinguished here. First, if the two ratios are equal to one then we have a sphere: $\frac{b}{a} = \frac{c}{a} = 1$. If the major axis is longer than the intermediate and minor ones, c $\approx$ b < a , than the ellipsoid is prolate. Finally, if the minor axis is smaller than the other two, c < b $\approx a$, we have an oblate ellipsoid.

A plot of the void shapes and the ellipticity distribution for the current void population can be seen in Fig. 4.5. The left panel shows that there are more prolate voids than oblate ones. The average values found for the axes ratios are $\frac{b}{a} \approx 0.73$ and $\frac{c}{a} \approx 0.56$. The right panel shows the ellipticity (ϵ = 1 - $\frac{c}{a}$) probability distribution. The voids appear to have a slightly skewed distribution at $\epsilon > 0.4$. In Fig. 4.6, we also show two examples of voids, a more spherical void with axes ratios of $\frac{b}{a} = 0.94$ and $\frac{c}{a} = 0.91$ and an aspherical one with $\frac{b}{a} = 0.37$ and $\frac{c}{a} = 0.28$. It is clear that these objects deviate quite substantially from ideal geometrical bodies.

Platen, van de Weygaert, and Jones 2008 found that the ellipticity distribution to be skewed at a value higher than $\epsilon > 0.5$. Furthermore, they found the average values of the axes ratios to be $\frac{b}{a} \approx 0.7$ and $\frac{c}{a} \approx 0.49$. Similarly, Shandarin et al. 2006 found average values of $\frac{b}{a} \approx 0.65$ and $\frac{c}{a} \approx 0.45$ respectively. Our results are in good agreement with the previous findings.

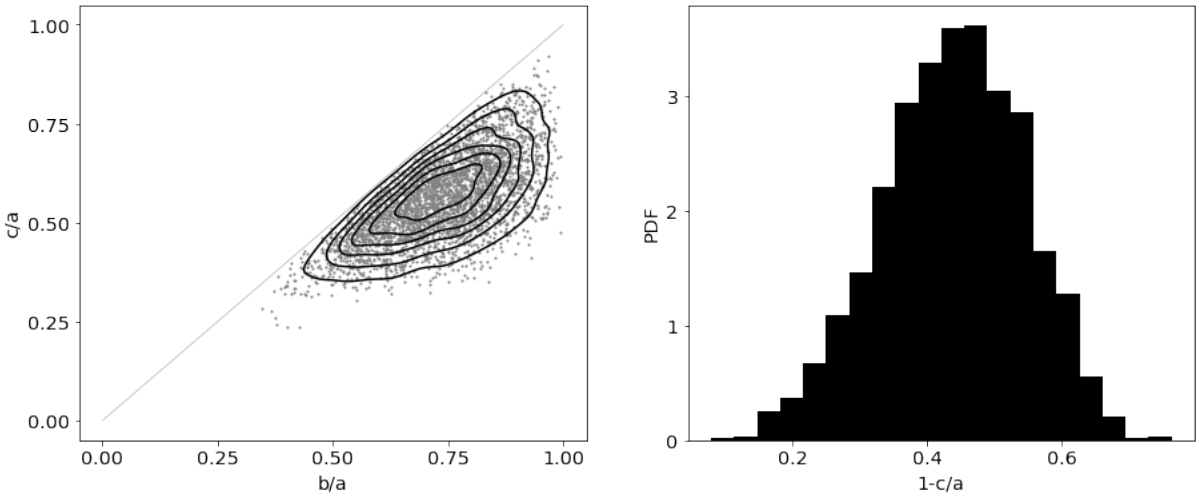

Figure 4.5: Shape characteristics of the void population. *Left*: scatter plot of the axes ratio of the void ellipsoids $\frac{b}{a}$ and $\frac{c}{a}$. The density distribution contour has been superposed in black in order to better visualise the shape tendency. *Right*: Ellipticity distribution of the void ellipsoids.

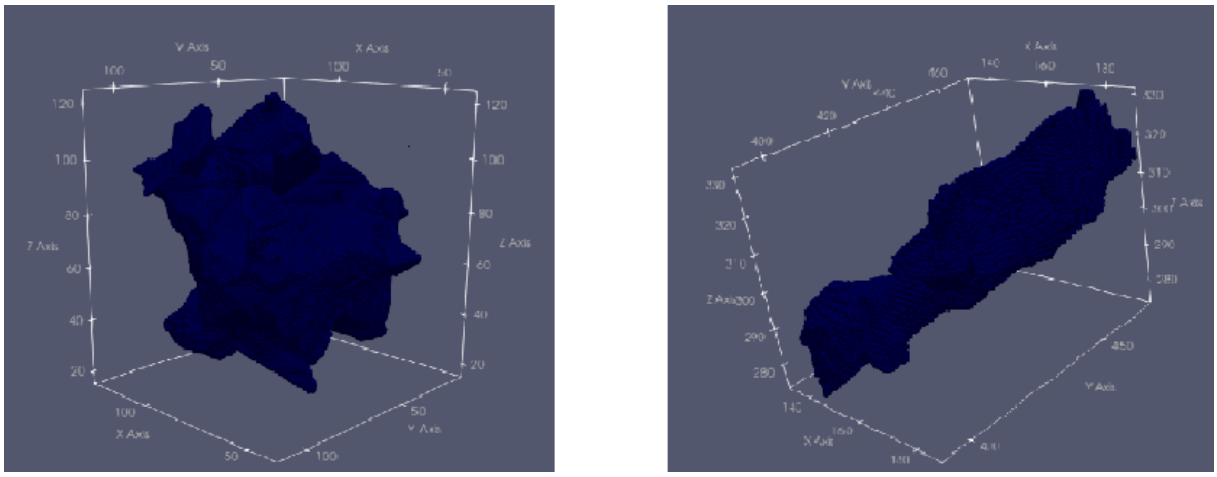

Figure 4.6: Examples of voids in the GADGET-2 simulation. *Left*: A spherical void, with semiaxes ratios of $\frac{b}{a} = 0.96$ and $\frac{c}{a} = 0.92$. *Right*: An elongated void with $\frac{b}{a} = 0.42$ and $\frac{c}{a} = 0.23$.

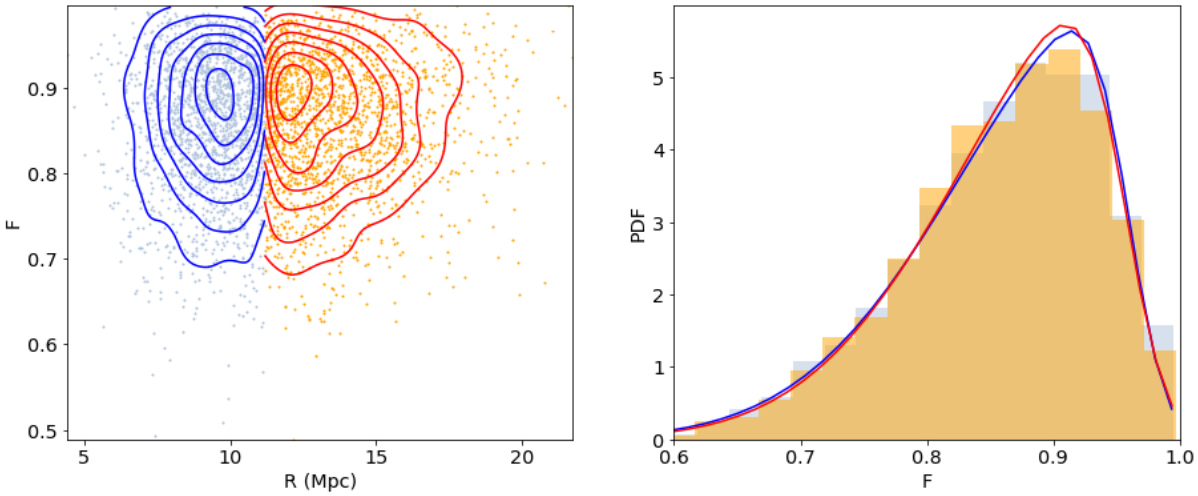

Figure 4.7: *Left*: Form Factor as a function of equivalent radius for small (blue) voids and big (red) voids computed using the ellipsoid approximation. *Right*: Probability distributions of the form factor for the two subpopulations.

We can further analyse the shapes by splitting the void population in half based on the equivalent radius. Thus, we will have a group of small voids (R $<$ 11.17 Mpc) and one of large voids (R $>$ 11.17 Mpc). Keep in mind that this split is arbitrarily made and thus, not motivated by any physical means. The rationale behind it is to investigate the existence of a trend in the void shapes. Once we have done this, we proceed by computing the Form Factor (van de Weygaert 1991), defined as:

$$F = 36\pi \frac{V^2}{A^3} \tag{4.11}$$

where V and A represent the volume and area of the void. A Form Factor equal to one corresponds to a sphere. As an approximation, we can assume V and A to be the volume and area of the void ellipsoid and compute them using the ellipsoid axes previously found. Thus, the volume and area of an ellipsoid are defined to be:

$$V = \frac{4\pi}{3} abc \tag{4.12}$$

$$A = 4\pi \left(\frac{(ab)^{1.6} + (ac)^{1.6} + (bc)^{1.6}}{3} \right)^{\frac{1}{1.6}} \tag{4.13}$$

Fig. 4.7 shows the form factor as a function of equivalent radius. No major differences can be seen for these two groups.

The Form Factor can be recomputed using the area and the volume of the convex hull. Using the boundary-to-center distance, we can again search for a dependence of shape on size (Fig. 4.8). The first thing to notice is that the mean Form Factor has a lower value for both the small and large voids. Furthermore, the large voids appear to have a slightly bigger (but noticeable) Form Factor than the small voids which implies that they have a more spherical shape.

The tendency towards sphericity is in agreement with the evolution of spherical and isolated underdensities (Bertschinger 1985b; van de Weygaert and van Kampen 1993). In reality, voids

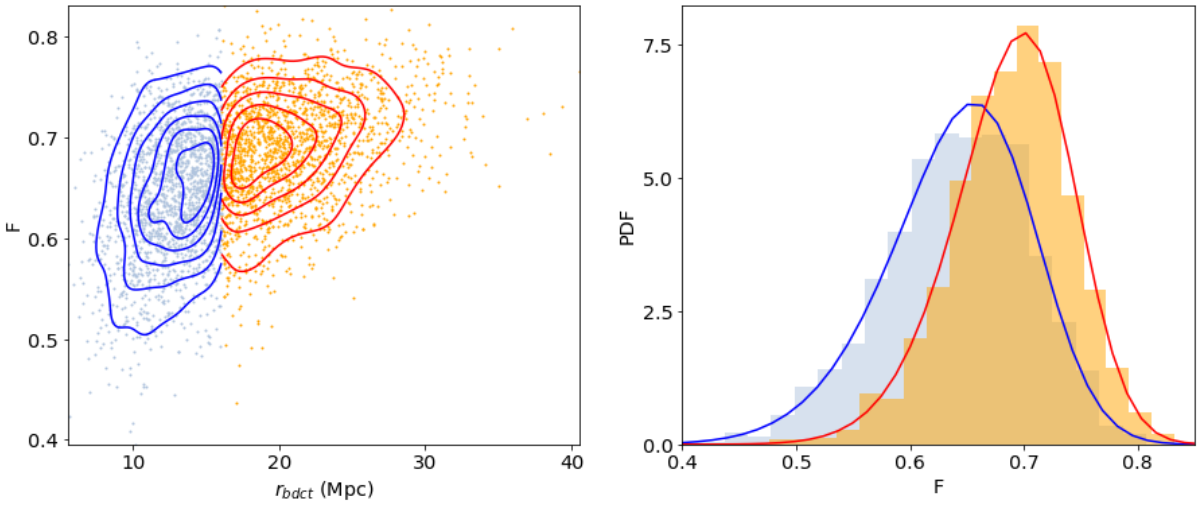

Figure 4.8: *Left*: Form Factor as a function of boundary-to-center distance for small (blue) voids and large (red) voids, computed using the Convex Hull algorithm. *Right*: Probability distributions of the form factor for the two subpopulations.

are not perfectly spherical due to the presence of tidal fields generated by surrounding filaments and clusters which distort their shapes.

4.5 Density profiles

We now focus on the interior matter content of voids by studying their density profiles. The radial density profiles of voids have been obtained by averaging the density values at various radii of concentric shells. The center of the shells is taken to be the center of mass of a void (i.e Eq. 4.2).

Furthermore, we compute the average density contrast $\Delta(r)$ (Eq. 1.2) within radius r:

$$\Delta(r) = \frac{3}{r^3}\sum_{0}^{r} r'^2 \delta(r') dr' \tag{4.14}$$

where $\delta(r')$ is the radial density profile previously discussed. This is useful in determining how the radial density deviates from a spherically symmetric distribution.

Fig. 4.9 shows the average $\delta(r)$ and $\Delta(r)$ for a sample 850 voids. The x axis has been normalized to the characteristic void size $r_{norm} = \frac{r}{r_{ch}}$. The interior of voids ($r_{norm} < 0.5$) is underdense ($\delta < 0$), indicating the absence of matter close to its center. As the radius increases ($r_{norm} > 0.5$), the density slope increases exponentially, indicating that the matter has been pushed towards the boundary where the network of filaments, clusters and walls reside.

The average radial density profile $\delta(r)$ follows closely the density contrast $\Delta(r)$ in the interior of voids. At approximately 1 r_{norm}, a sudden bump appears in profile followed by an exponential increase at a radius of $r_{norm} \approx 1.75$

This result is in agreement with the density evolution of a tophat void (Sheth and van de Weygaert 2004). The bump that appears at a radius $r_{norm} \approx 1$ can be understood by recalling that this is the average radius of a void. This implies that at this location, we will encounter (on the average) the high density boundaries. Voids larger than the characteristic size will show

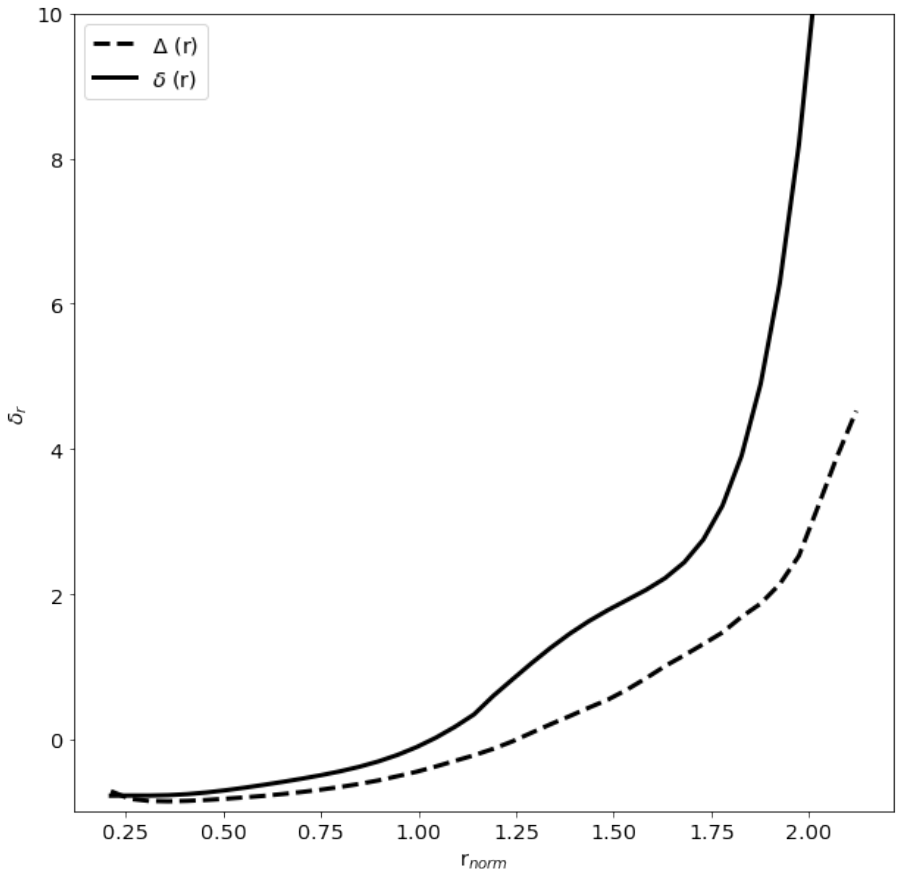

Figure 4.9: Average radial density profile (full line) and density contrast of a sample of voids (N = 850). The radius of the shells have been normalized to the characteristic void size $r_{norm} \approx$ 16.76 Mpc.

even higher density boundaries, as it can be seen in exponential increase past $r_{norm} = 1.50$. The deviation from an ideal exponential can also be an indication of the substructure present within voids (van de Weygaert and van Kampen 1993).

The radial profile represents a first approximation based on the rather spherical shape of voids, although as it was shown in Fig. 4.6, they can deviate substantially from a sphere. A useful method that takes into account the shape of the void has been developed by (Cautun, Cai, and Frenk 2016). In this study, the authors describe the density profile relative to the boundary. They rescale the profiles by the boundary thickness and show that the average profile is independent of the void size.

4.6 Dynamics

Besides the density profiles, understanding the dynamics within voids is also crucial in understanding the void environment.

We present our results on the dynamics of voids in Fig 4.10. The top left panel shows a slice of the density field in which the usual components of the cosmic web can be seen: clusters, filaments and voids. The top right panel shows the corresponding velocity field. The magnitude of the field ranges up to $\approx$ 1300 km/s (yellow) down to $\approx$ 10 km/s (dark blue). The regions with a large velocity magnitude correspond to regions of high density . On the other hand, low velocity values correspond to underdense regions. The stream plot indicates the flow of matter. One can notice that the stream arrows originate in a low density regions and they point towards high density ones. This is an indication of the void's expansion, causing the outflow of matter from within the voids into the surrounding filaments. The bottom panels show the corresponding voids that have been identified with the watershed algorithm.

We would like now to find the location of a dynamical center within voids which we will use to compute our radial velocity profiles. We search for the expansion point which corresponds to the point that has the highest velocity divergence. We expect to find this point at the origin of the streamlines in our plots. To compute the velocity divergence field in our simulation, we make use of the DTFE algorithm (recall Chapter 3.3). The top panels of Fig. 4.11 show cross-sections of the velocity divergence field in the simulation. The yellow region represents a watershed void. Interestingly, we find that the minimum velocity magnitude (blue point) is located at the origin of the outflow stream and not the maximum divergence (red point).

We can better visualise this phenomena by looking at a 3D plot of the void (Fig. 4.13). Both points appear to be located at the void's boundary. The minimum velocity is located at the origin of the velocity stream.

This can be an indication that this void is part of a larger underdensity (or overdensity), hinting at the void hierarchy. Aragon-Calvo and Szalay 2013 has studied the void hierarchy in the velocity field of voids in an N-body simulation. They showed how the velocity field breaks into smaller expanding subdomains, corresponding to smaller voids. This may explain why the void shown here is not an expansion center.

Once we have established the minimum velocity point as a reference, we compute the radial velocity profiles of voids in a similar manner to the radial density profiles. We can further compare the velocity profiles of the voids with the predictions made by the linear theory. In this model, the average radial peculiar velocity $v_{lin}(r)$ is equal to

$$v_{lin} = -\frac{1}{3} H_0 f(\Omega_0) r \Delta(r) \tag{4.15}$$

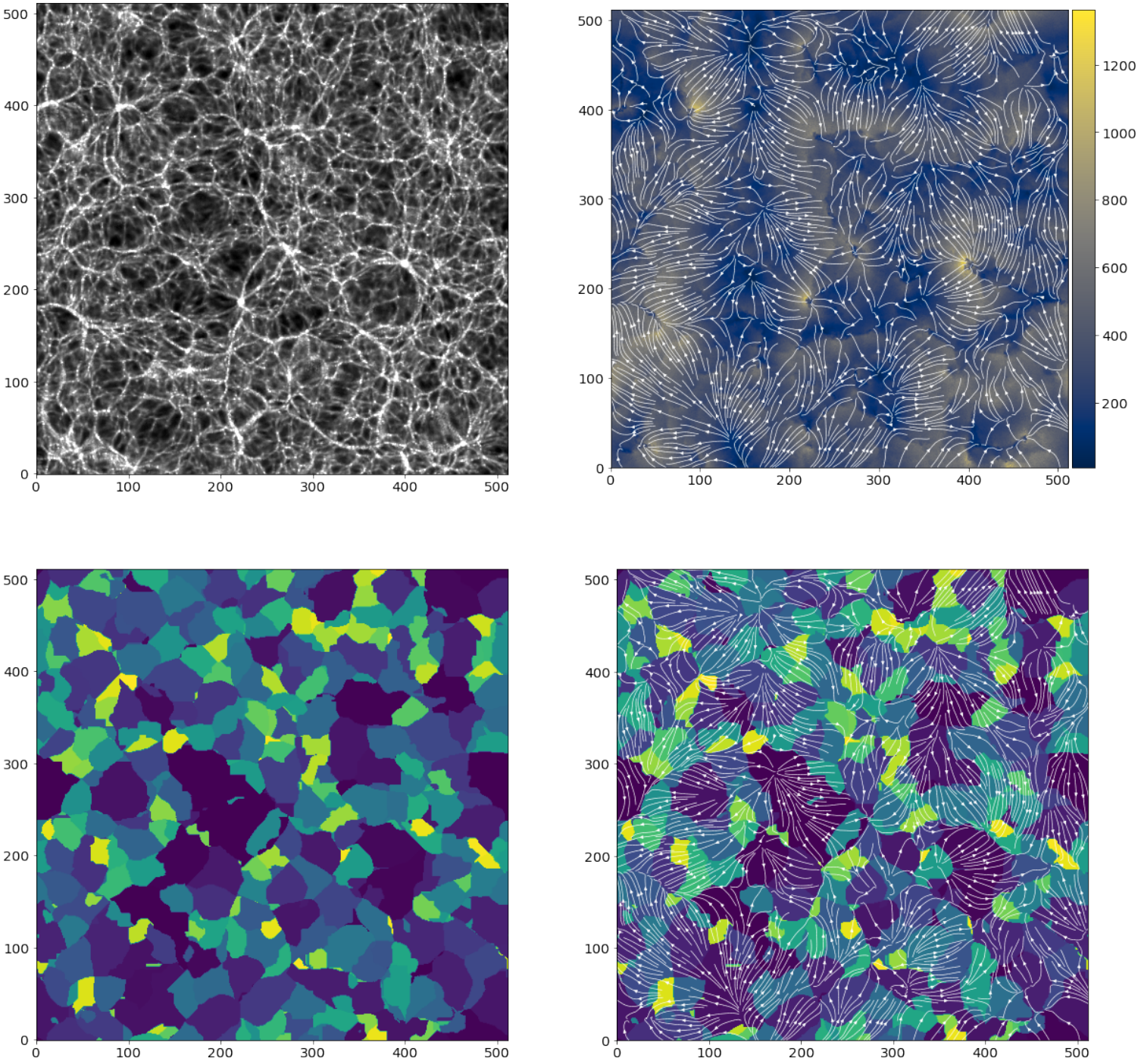

Figure 4.10: Dynamics of voids illustrated. Top left: Slice of density field in the simulation. Top right: corresponding velocity field. The white arrows indicate the flow of matter . Bottom left: corresponding voids identified by the watershed. Bottom right: same as bottom left, the stream of matter has been superposed over the voids to indicate their outflowing nature.

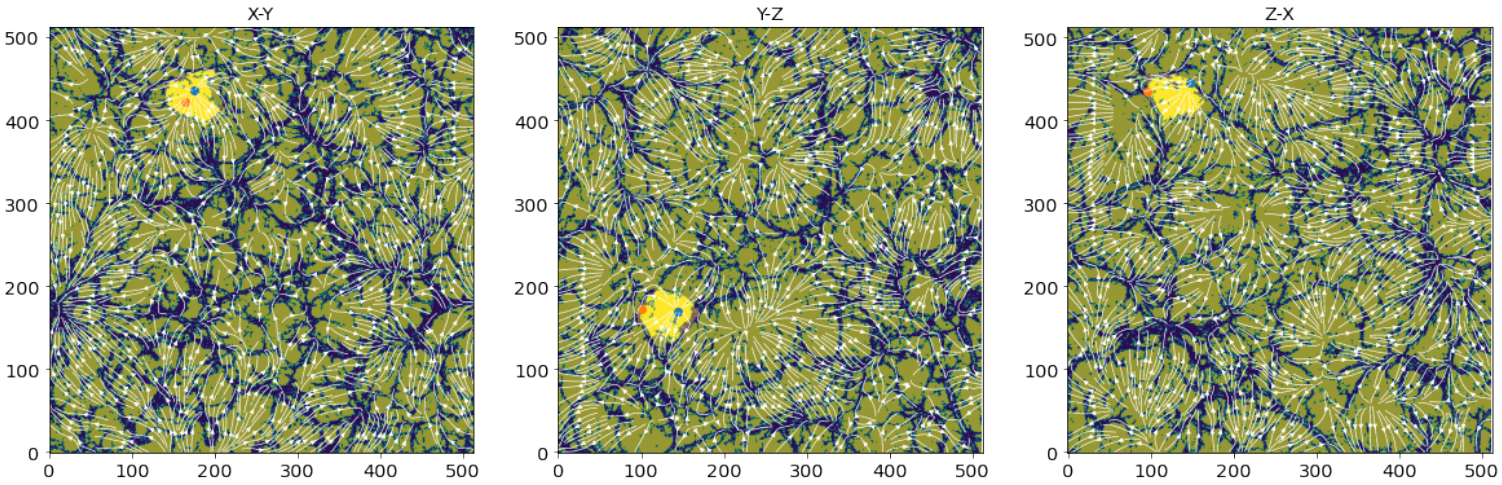

Figure 4.11: Cross sections of the velocity divergence. The green / blue areas represent regions with positive / negative velocity divergence respectively. A watershed void (yellow area) is being shown together with the minimum velocity magnitude value (blue point) and maximum divergence (red point).

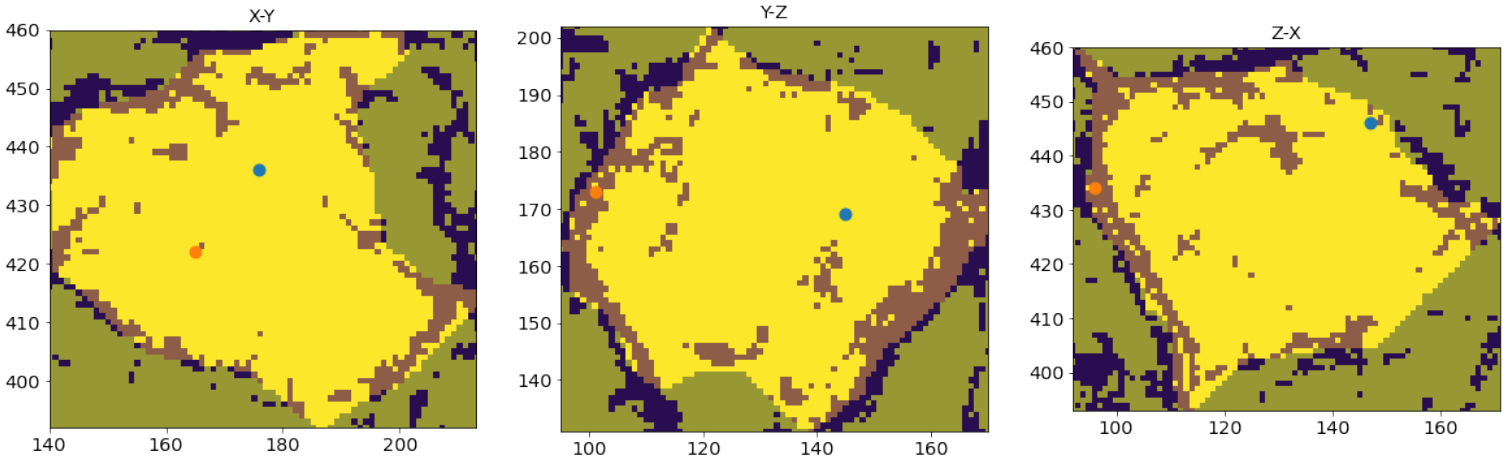

Figure 4.12: Zoom in on the void cross-sections.

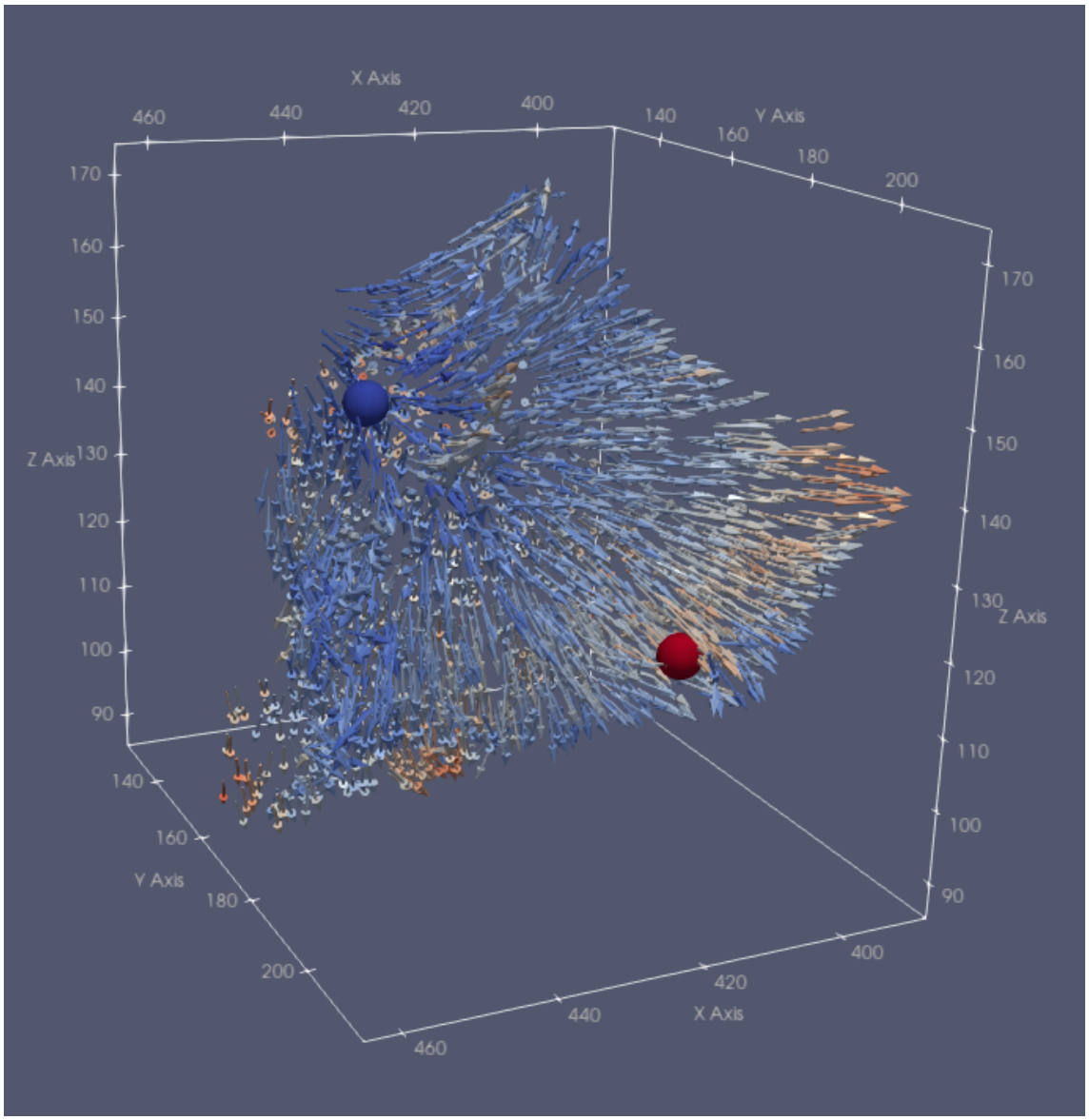

Figure 4.13: Three dimensional velocity stream flow of the watershed void from Fig. 4.6. The blue-red color gradient of the arrows indicate the regions of low/high velocity. The red sphere corresponds to the location of the maximum divergence. The blue sphere indicates the position of the minimum velocity magnitude.

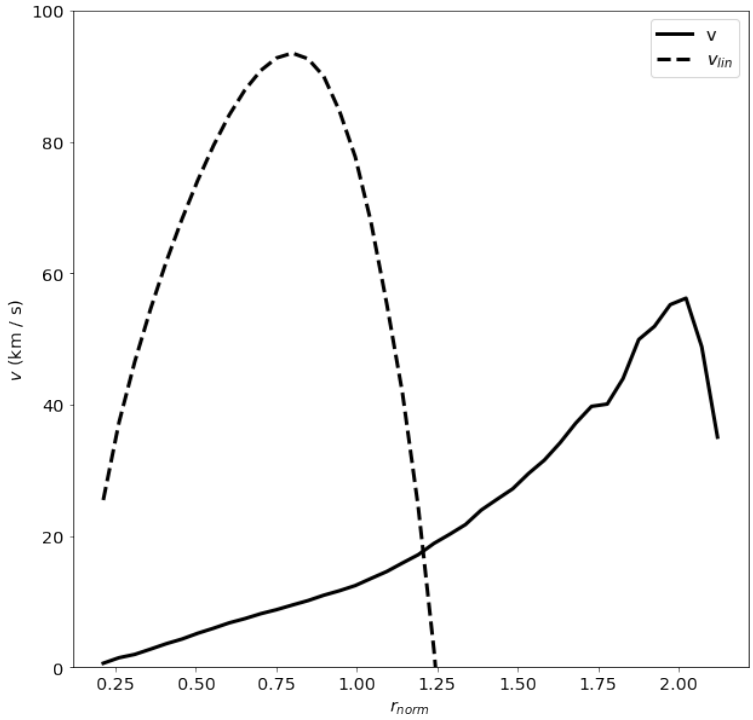

Figure 4.14: Average radial (full line) and linear (dashed line) velocity profiles with respect to the velocity at the center of mass for a sample of voids (N = 850). The radius of the shells have been normalized to the characteristic void size $r_{norm} \approx 16.76$ Mpc.

where $f(\Omega_0) \approx \Omega_0^{\gamma}$ is the velocity function with $\gamma = 0.55$ for the ΛCDM model (Peebles 1980) and $\Delta(r)$ is the average density perturbation at a radius r (Eq. 1.2). Fig. 4.14 shows the average radial and linear velocity profiles for a sample of 850 voids. The radial profile increases linearly up to a distance of $r_{norm} = 1$, in agreement with the nearly flat $\delta(r)$. Beyond this distance, the growth deviates from linearity and achieves a maximum value of 60 km/s after which it starts declining. The linear velocity profile increases much more abruptly and it peaks with a value of ≈ 100 km/s, at a shorter distance from the void center. The mismatch between the two profiles may again suggest the presence of the void hierarchy. However, further studies on this issue are required.

Once we have characterised the void environment, in the next chapter we proceed by discussing the effect that voids have on the properties of dark mater halos.

Chapter 5

Void Halos

In this chapter we investigate the properties of halos identified in the watershed voids. We start by presenting the overall halo population and its abundance. We present the halo mass function, spin and shape parameters and relate these properties to the void's intrinsic characteristics.

5.1 Halo population

The total number of halos identified in the GADGET-2 simulation is 1.185 $\times 10^5$ halos. Our halos have virial masses between $10^{11.8} M_\odot < M_{200c} < 10^{15} M_\odot$ and a number of particles per halo that satisfies $N_{part} > 50$. Fig. 5.1 shows the overall halo population in GADGET-2. Notice how the halos trace the familiar cosmic web components: filaments, nodes and voids. Looking at the right zoom-in panel, one can notice that the halos are located mostly in filaments and clusters. This is to be expected since these are the denser regions which would facilitate the formation of halos in greater number.

The number of halos identified in voids is $\approx 8.8 \times 10^4$ (75% of the total number of halos in the simulation). Fig. 5.2 shows the number of halos as a function of distance from the void's boundary and of distance from the void's center. Consider the distance from the boundary first, r_{bd}, and notice that the majority of halos are located in the boundary's vicinity. As the distance increases, the number experiences an exponential drop. The reason being that we are sampling regions deeper inside voids, where the density decreases exponentially. Looking at the distance from the center, r_{ct}, reveals that this is just the mirror image of the distance from the boundary. This time, smaller values of r correspond to distances closer to the center. The intersection of the two distributions occurs close to the characteristic void size radius (dashed line).

The large percentage of void halos found is due to the Watershed algorithm which identifies the boundaries of voids as high density regions (recall the flooded geological landscape from Chapter 4 in which the basins were separated by ridges). The fraction of halos residing in voids has been found to be 10-11% (Cautun, van de Weygaert, Jones, and Frenk 2014 + private communication). We found a number of 9466 (10.66%) halos residing in voids at a distance from the boundary equal to the characteristic void size (i.e $r_{bd} > r = r_{ch}$). In what follows, we consider these halos to be the representative sample of void halos.

5.2 Halo Mass Function

A quantitative and practical approach in studying the distribution of halos is the halo mass function (HMF). This will help us in assessing the mass contribution of the halos to the population abundance. The HMF is defined as the comoving number density of halos per logarithmic mass

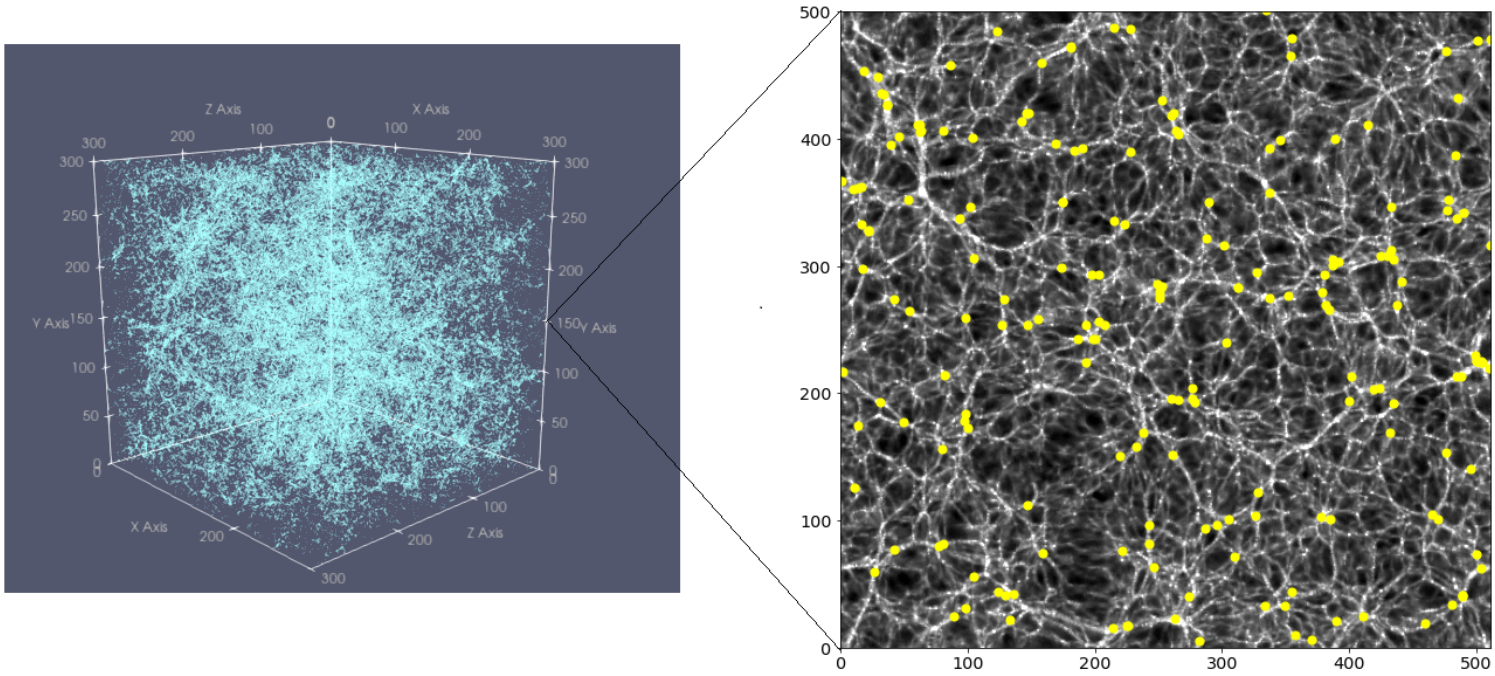

Figure 5.1: Halo population identified by ROCKSTAR in the GADGET-2 simulation. The zoom in shows a cross-section of the density field through the middle of the simulation box. The yellow points show the positions of the halos centers.

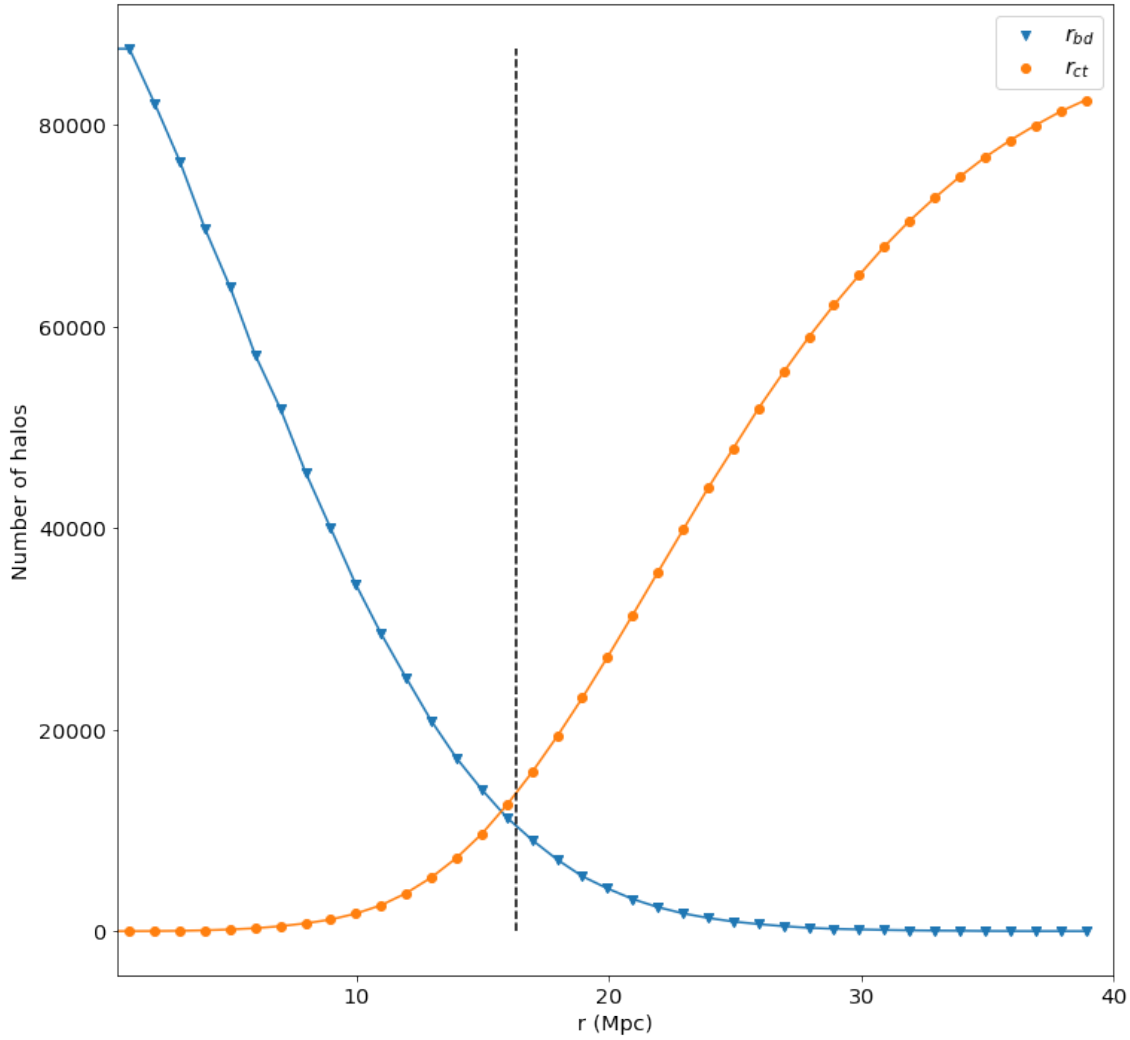

Figure 5.2: The number of halos as a function of distance from: the void boundary (blue, triangles) / void center (orange, circles). The dashed line represents characteristic void size radius.

bin (that is $n(M) = \frac{dn}{dlogM}$) and is characterized by a power-law at low-mass halos followed by an exponential cut-off at more massive ones. Furthermore, the obtained HMF can be fitted with a Shechter function (Schechter 1976) defined as:

$$\phi = \phi^* \left(\frac{M}{M_*}\right)^{\alpha} e^{-\frac{M}{M_*}} \tag{5.1}$$

where M_* is the characteristic mass, α is the faint-end slope and ϕ^* is a normalization factor.

Fig. 5.3 shows the HMF for halos in the overall simulation and for halos located within voids. The halo masses for the overall population spans an interval of three orders of magnitude (between 10^{12} and $10^{15}h^{-1}M_{\odot}$). For the void halos, the HMF suffers a decrease in both the number density and mass, covering only $\approx 10^{12} - 10^{13.3}h^{-1}M_{\odot}$. More than 90% of the halos have a mass of $\approx 10^{12}h^{-1}M_{\odot}$. This is to be expected since the interior regions of voids are underdense and thus, unable to produce halos with large masses.

The most relevant study of the environmental properties of halos in the cosmic web has been performed by Cautun, van de Weygaert, Jones, and Frenk 2014. The authors studied the components of the web through their mass, volume, density distribution and halo population using the NEXUS algorithm. For the halos located in the void environment, they report lower masses than our present findings, with $\approx$ 95 % halos having a mass lower than $10^{11}\ h^{-1}\ M_{\odot}$. However, large discrepancies in regard to the massive halos appear due to the different identification methods. These methods result into a mass range for the void halos between $\approx 10^{10} - 10^{13}h^{-1}M_{\odot}$. These were justified by the use of the NEXUS algorithm (Aragón-Calvo et al. 2007; Cautun, van de Weygaert, and Jones 2013) which is designed to primarily identify nodes, filaments and walls. As a consequence, voids are identified as structures that are *not* nodes, filaments or walls. By contrast, the Watershed Void Finder is specifically designed to identify voids in a given density field.

The study by P. Ganeshaiah Veena et al. 2019 reports a void HMF covering a mass range between ($\approx 10^{10} - 10^{12.8}h^{-1}M_{\odot}$). The lack of low mass halos in our sample may be explained by the fact that the authors use a simulation with a higher resolution. Another reason that can explain the differences is the method used to detect voids and halos. These authors also used the NEXUS algorithm and thus the previous explanation may still apply here.

Metuki, Libeskind, and Hoffman 2016 have also explored the relation between the halo abundance and the cosmic web environment. They show that the halo abundance in voids is lower with respect to the other cosmic web components. This difference has been attributed to the ambient density in the respective environments.

5.3 Halo Shape and Spin

Two other important properties which characterise the halos are the shape and spin parameters. We mentioned previously that the shape quantifies the symmetry of the halo mass distribution and is represented by the principal axes ratios of the halo ellipsoid: $\frac{b}{a}$, $\frac{c}{a}$ and $\frac{c}{b}$.

The shape parameters have been obtained by the Rockstar Halo Finder algorithm (Behroozi, Wechsler, and Wu 2013). The authors computed the mass tensor for particles inside the halo radius:

$$M_{ij} = \frac{1}{N}\sum_{N} x_i x_j \tag{5.2}$$

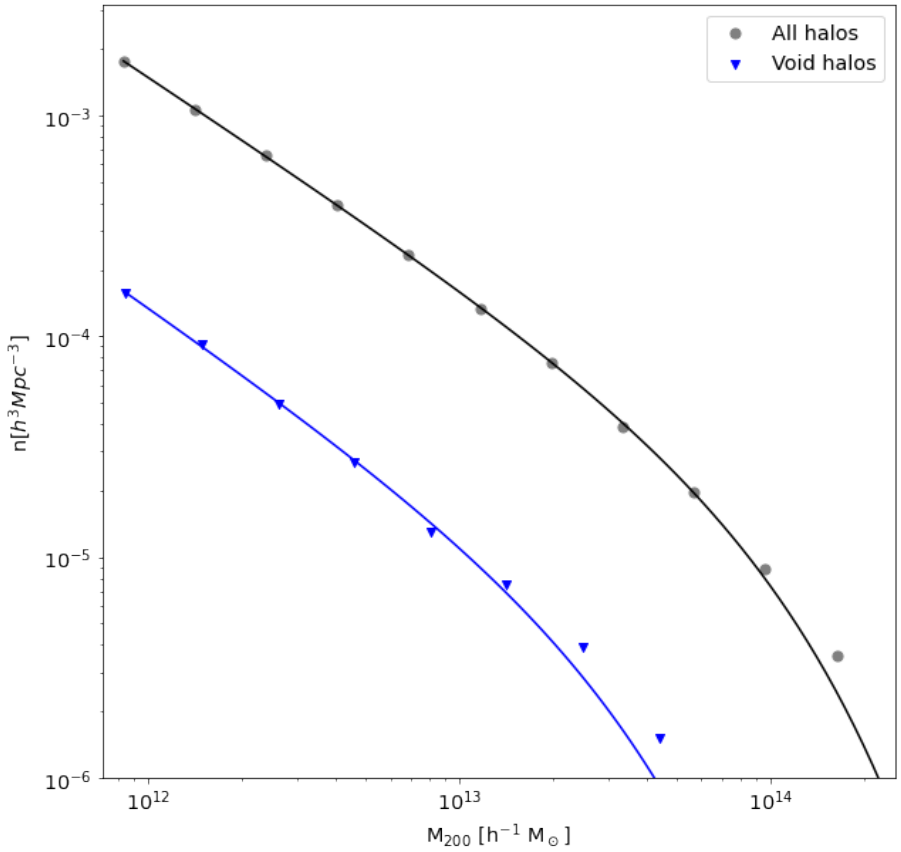

Figure 5.3: Mass function for halos in the overall simulation (grey, circle) and for halos within voids (blue, triangles).

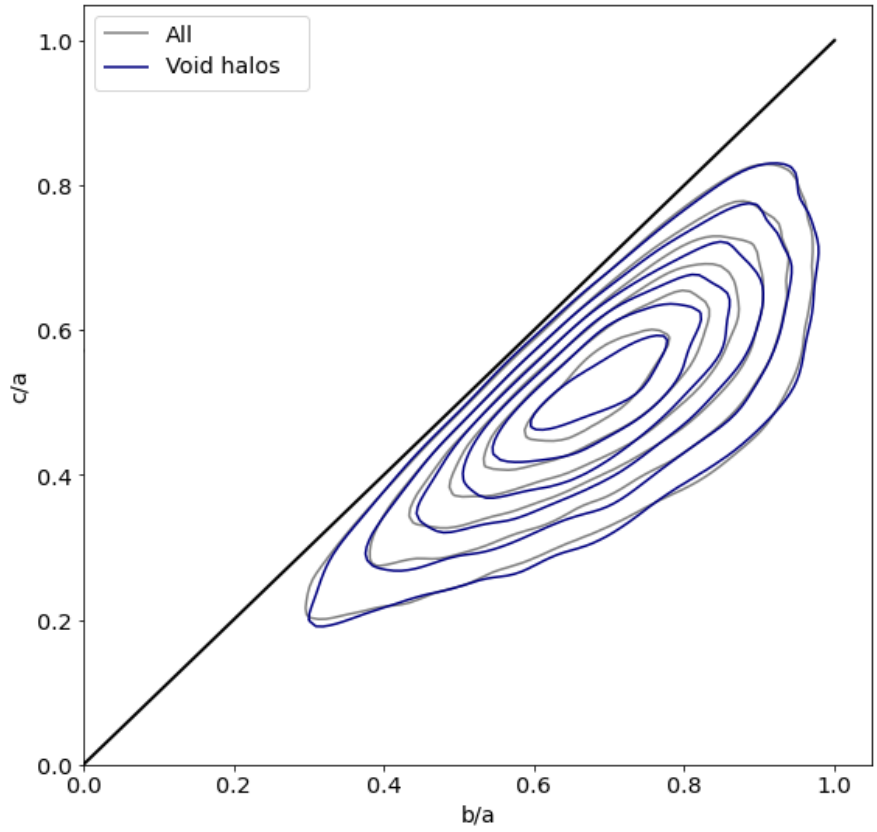

Figure 5.4: Halo shapes distribution for all the halos (gray) and for halos in voids located at the characteristic void size (blue) in the GADGET-2 simulation

where x_i denotes the position of the particle along the i-th coordinate With respect to the halo center of mass. The eigenvalues of this tensor are the squares of the ellipsoid's axes (i.e a^2, b^2, c^2).

In Fig. 5.4 we show the shapes for the void halos (blue) and for the whole halo population (grey). In both cases, the contours correspond to the probability distributions of the axes ratios. The overall halos appear to have a rather prolate shape, with an average $\frac{b}{a}$ and $\frac{c}{a}$ equal to $\approx$ 0.686 and $\approx$ 0.497 respectively. The void halos appears to be slightly displaced, making them more anisotropic, with average axes ratios of $\frac{b}{a} = 0.685$ and $\frac{c}{a}$ =0.493.

The two panels of Fig. 5.5 show the average axes ratios of the void halos at various distances from the void boundary and center. The horizontal, dotted lines indicate the mean values for the overall halo population while the vertical, dashed lines indicate the characteristic void size. Halos located at distances between 0 and 15 Mpc from the boundary (blue, triangles) have lower axes ratio values in comparison with the overall population, indicating that they are more flatten. However, past the value of 15 Mpc, the axes ratios increase again. At distances larger than 20 Mpc, the errors drastically increase due to the limited number of halos near the void center.

Similarly, looking at the distribution starting from the center (orange, circles), at values of $r \approx 0$ Mpc (near the origin of the void) the mean axes ratios present a sudden spike followed by a decrease. This is due to the low number of halos located near the center. Notice that as we increase the radii, the average value starts increasing again until it reaches the average value of the overall population.

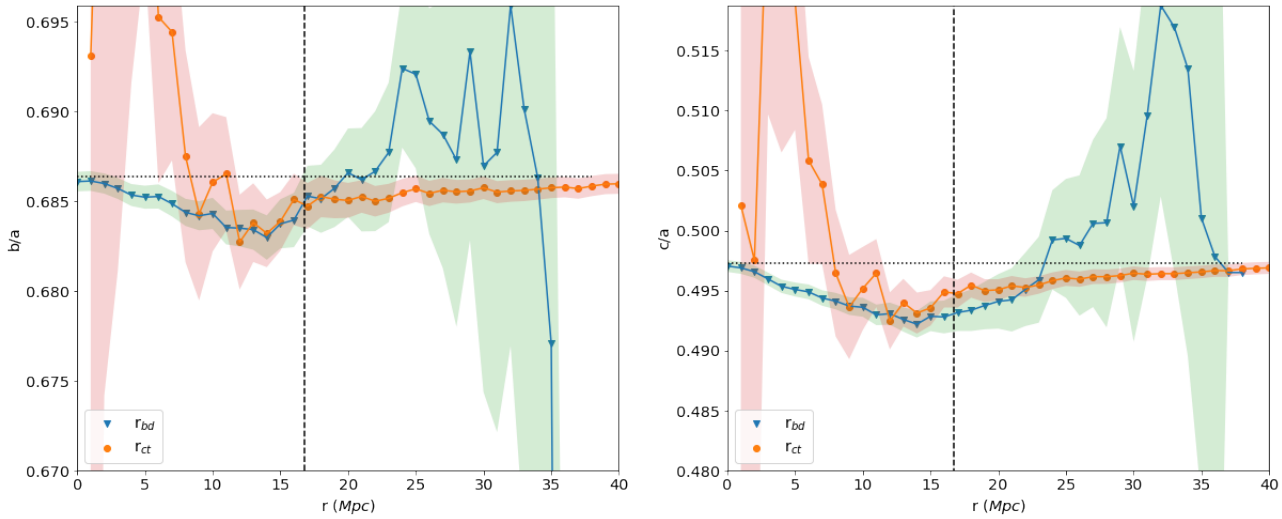

Figure 5.5: Average $\frac{b}{a}$ (left) and $\frac{c}{a}$ (right) axes ratios as a function of distance from the void boundary (blue, triangles) and from the void center (orange, circles). The horizontal, dotted line shows the $\frac{b}{a}$ / $\frac{c}{a}$ for all halos in the simulation. The vertical, dashed line shows the characteristic void size.

Previous studies (Warren et al. 1992; Cole and Lacey 1996; Kasun and Evrard 2005; Bailin and Steinmetz 2005) have found that halos are triaxial ellipsoids, who assume a more prolate shape rather than an oblate one. They are characterised by $0.5 < \frac{c}{a} < 0.75$, in agreement with our results. More recently, Ganeshaiah Veena et al. 2018 used a large sample of halos from the P-Millenium simulation in order to investigate their alignment with respect to the components of the cosmic web. Overall, they report more spherical halos, with the majority having $\frac{b}{a} > 0.9$ and $\frac{c}{a} > 0.8$. A second finding indicates that the average axes ratios for the halos in voids are lower than for the halos located in filaments and walls. Interestingly, given the fact that void halos have, in general, a lower mass we would have expected them to be more spherical, as it was suggested by (Bailin and Steinmetz 2005; Kasun and Evrard 2005).

The second main property of halos is the spin. In Chapter 2 we mentioned that this property is quantified by the Bullock parameter λ defined as:

$$\lambda = \frac{J}{\sqrt{2}MVR} \tag{5.3}$$

where J is the angular momentum within a sphere of radius R containing mass M while V is the circular velocity of a halo at distance R.

Essentially, λ is used to quantify the importance of angular momentum with respect to random motions. As such, high values of λ suggests a halo which is supported by rotation while low values indicate a halo dominated by random motions.

Fig 5.6 shows the spin as a function of the halo mass. The overall halo population is depicted in grey while the void halos in purple. The first thing to notice is that halos with larger masses spin more slowly (in accordance with the conservation of angular momentum). Subsequently, for halos within voids, both the mass and the spin distributions have lower values with respect to the overall halo population.

Fig. 5.7 shows the average spin (left panel) and mass (right panel) values as a function of the boundary / center distances. First of, notice the same systematic, linear decreasing trend on the

first ≈ 15 Mpc for the average spin as a function of distance from the boundary (blue, triangles). Past this value, the distribution starts presenting various spikes, accompanied with larger and larger errors (remember we are sampling deeper regions within the void with a sparser number of halos). Turning to the spin distribution as a function of distance from the center (orange, circles) we notice a similar pattern. At values closer to the origin, we have fewer halos and thus, larger errors associated which manifests as a sudden spike. Once we go further from the center, at larger radii, the spin starts slowly increasing until it meets the overall halo population (dotted, horizontal line).

We stress that this effect is very subtle and only visible when we consider a large number of halos. For example, consider the halos identified in three arbitrary voids (Fig. 5.8). The white clouds of points represent the voids while the spheres show the positions of the halos. The color gradient shows the spin (bluer halos have a lower spin than whiter ones). At a first glance, one can not easily affirm that lower spin halos reside deeper inside the void. We also show the scatter plot of the halo spins as a function of distance from the boundary in Fig. 5.9. An arbitrary separation based on the mean spin value has been made in order to illustrate low spin and high spin halos. The effect of the spin decrease as the distance from the boundary increases is now visible.

A few things to note regarding the fluctuations that appear both in Fig. 5.7 and Fig. 5.5. First off, the spikes that appear closer to the void center are accompanied by large errors. As we mentoned, these are explained through the sparse number of halos that populate the void interiors. Another explanation for the spikes that appear in the spin vs boundary distance distribution may be the following: the convex hull boundary of a void is defined by a limited number of points. If a halo is located at the true void's boundary but there is no convex hull boundary point located there, then the closest hull boundary point to that halo may be located on the opposite side of the void. As such, the distance between that halo and the hull boundary may have a much larger value than in reality. This will also result in a larger value for the properties discussed so far.

Hahn et al. 2007 studied the evolution of dark matter halo properties in different environments and found that, at $z = 0$, the lower mass void halos will spin slower than for halos at the same masses in other environments. This has been further confirmed by Ganeshaiah Veena et al. 2018 who showed that the average spin value for void halos is $\lambda = 0.030$ while for the overall distribution is $\lambda = 0.035$.

In order to understand why the void halos posses a lower spin than the average, we must recall the mechanism by which halos acquire an angular momentum. We have seen in Chapter 2 that the answer lies in the Tidal Torque-Theory (TTT) (Hoyle 1951; Peebles 1969; Heavens and Peacock 1988). The TTT stated that in the linear regime, protogalaxies acquire angular momentum due to torques which are generated by the tidal field of the surrounding large scale structure. As time evolves and the nonlinear regime is reached, the mass contained in halos will extend to larger radii. This effect, coupled with the possibility of collision with other galaxies (halo mergers) will produce an increase in the angular momentum (Robertson et al. 2006). Since mergers are not often encountered in underdense regions, the void halos will posses a lower spin.

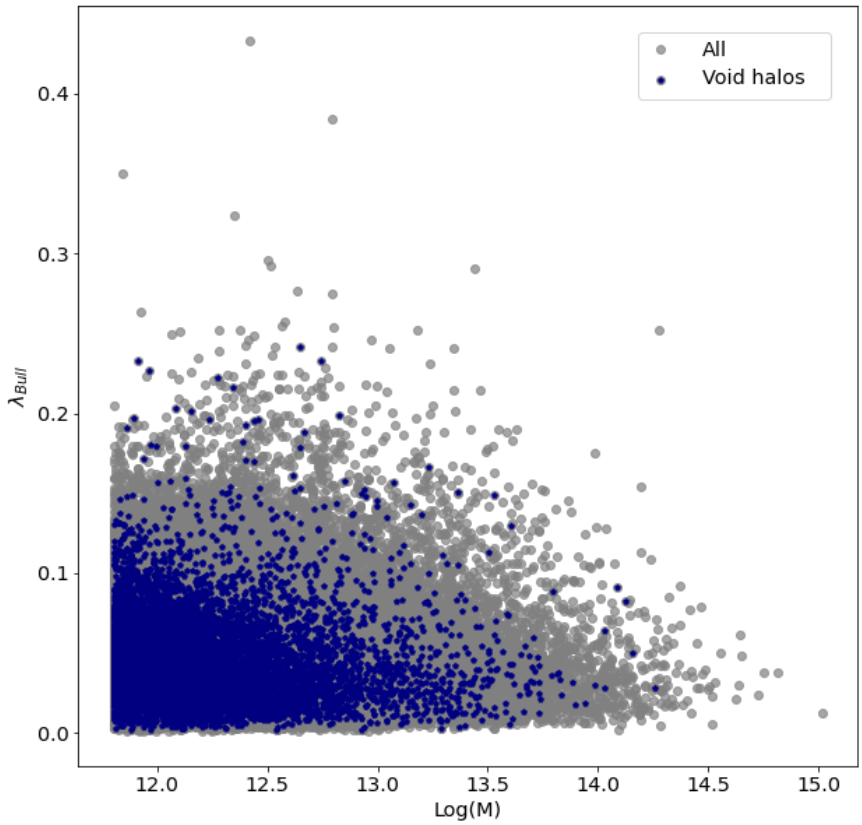

Figure 5.6: Spin distribution as a function of halo mass. The overall halo population is represented in gray while halos located within voids are shown in purple.

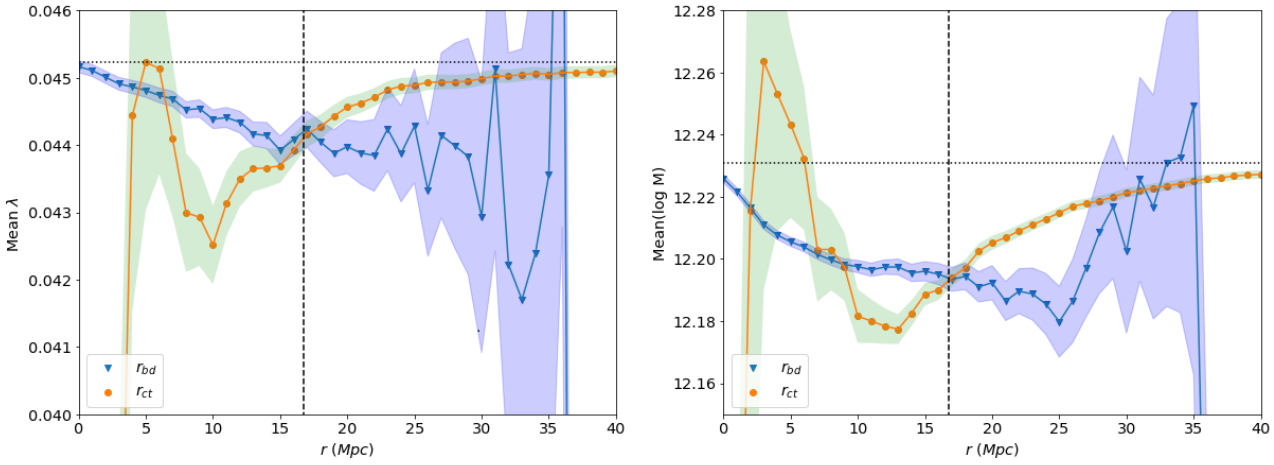

Figure 5.7: Average spin (left) and mass (right) distributions for void halos as a function of the distance from the void boundary (blue, triangles) and from the void center (orange, circles). The horizontal, dotted line shows the average spin / mass values for all halos in the simulation. The vertical, dashed line shows the characteristic void size.

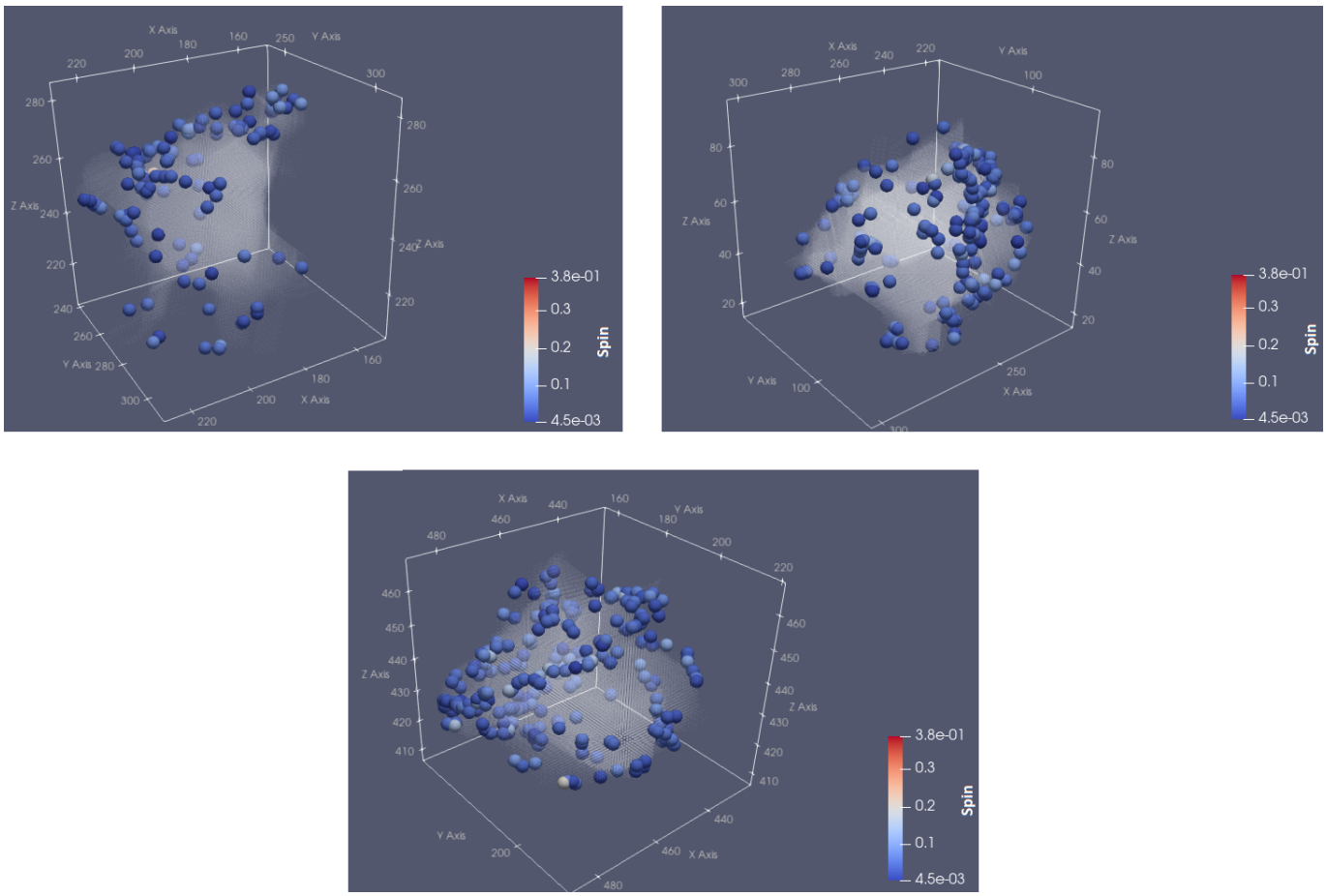

Figure 5.8: 3D perspective of halos inside voids. The void is represented by a cloud of points. The spheres represent the center of halo while the colour gradient corresponds to the spin value.

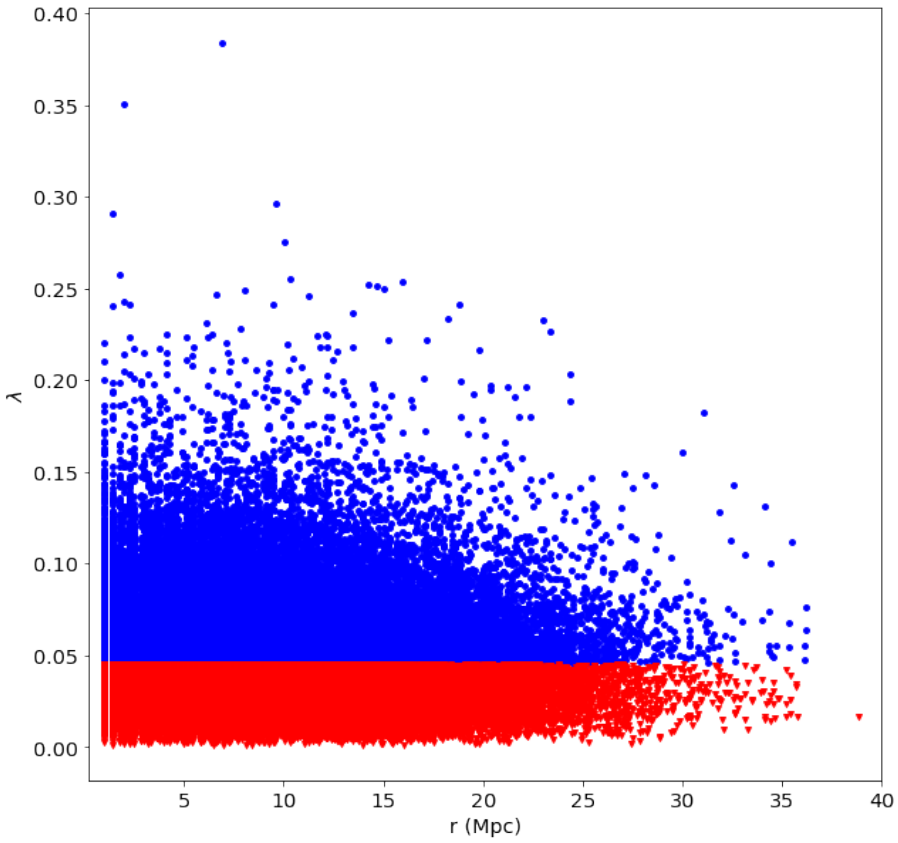

Figure 5.9: Scatter plot of the spin parameter as a function of distance from the boundary for all the halos identified inside voids. The blue points correspond to spin values higher than the average spin in the sample while the red points correspond to lower values.

Chapter 6

Conclusions

Voids are an essential component of the cosmic web. Due to their low density interiors, they represent an ideal environment to study the formation and evolution of dark matter halos - the backbone of galaxy formation. In this thesis we focused on the impact that the void environment has on halo properties.

We used the Watershed Void Finder algorithm to identify voids in the density field of a GADGET-2 simulation. The advantage of this algorithm is that it works directly on the topology of the field and it does not make any a priori assumptions on the geometry of voids. The only parameter input by the user is the radius of the filter. Furthermore, we used the convex hull algorithm in order to approximate the irregular void boundaries which, in turn, allowed us to better investigate the voids sizes and shapes.

The next step in our analysis is the halo identification in the particle distribution. For this, we used the Rockstar Halo Finder which has proved to be efficient in retrieving a variety of halo properties. For the specific identification of halos within voids, we again make use of the convex hull algorithm. This allowed us to study, for the first time, how the halo properties (such as the spin and shape) vary with respect to the distance from the void boundaries.

The characterization of voids as an environment represents a first result of our work. We found that voids have an average size of ≈ 17 Mpc which makes them about two times smaller than the most recent results from N-body simulations. We attributed this to the different tracer particles used. Further on, the shape analysis reveals that voids tend to be more prolate, deviating from a spherical shape. Most importantly, we found that larger voids tend to be more spherical than smaller ones, in agreement with the evolution of spherical, isolated underdensities.

The density profile analysis revealed the internal substructure of the voids: the average interior is described by an underdense, flat profile. As one approaches the boundaries, the density increases exponentially, revealing the presence of high concentrations of galaxy clusters and filaments. The irregularities that appear in the void profiles are a sign of substructure and, in turn, of the void hierarchy.

The void dynamics is also an import issue in their characterisation. The velocity divergence and velocity profiles reveal the expanding nature of voids. They are also an indicator for the void hierarchy with the large voids breaking down into smaller subvoids, each with their own velocity field. Further study is required in order to fully understand the implications of these results

The main purpose of this work was to investigate the properties of the void halos and to relate them to the void environment. To begin with, we showed that the halo abundance decreases exponentially as a function of distance from the void boundary. This is in agreement with the behaviour of the void density profile, which increases exponentially close to the boundary. We select a representative sample of void halos by choosing only the halos that are situated at a

distance from the boundary larger than the characteristic void size . As such, we found that the fraction of halos residing within voids is about $\approx 11\%$ of the total number of halos in the simulation. This selection has been made in order to avoid the potential halos residing on the high density boundary identified by the watershed algorithm. We follow with the computation of the halo mass function. Our results indicate that the void halos are less massive, spanning a mass interval between $\approx 10^{12} - 10^{13.3} h^{-1} M_{\odot}$ and are an order of magnitude less abundant than the overall halo population.

Finally, we analyse the shape and spin parameters. On the average, halos appear to be more prolate, in agreement with the previous findings. We found that void halos appear to be slightly more anisotropic with respect to the overall halos. This is also observable in the downwards trend of the average values of the axes ratios as a function of distance from the void boundary. This indicates that halos in voids are more flatten, contrary to the previous expectations that low mass halos would be more spherical. Regarding the spin, we found that for the same mass, void halos spin more slowly in comparison with the rest of the halos in the simulation. This is further confirmed by the decrease in the average spin as a function of distance from the boundary.

Further studies of this subject should include the use of higher resolution simulations (for example the QUIJOTE (F. Villaescusa-Navarro et al. 2020) or the Illustris simulations (Vogelsberger et al. 2014)), which will allow to probe halos with a wider range in mass and thus allowing the investigation of finer substructure within voids. Worth researching would also be the time evolution of the void halo properties. Furthermore, the convex hull algorithm does not perfectly approximates the boundaries of voids. In tracing out the void boundary, the algorithm may include regions which are not part of the void. An improvement may be seen by using the alpha shape method, a generalisation of the convex hull. Finally, a comparison with observational data might assure a reality check. This might include using mock galaxies as a tracer distribution and then comparing properties of the void galaxies with the galaxies from observations.

Bibliography

[1] M. A. Aragon-Calvo and A. S. Szalay. "The hierarchical structure and dynamics of voids". In: *MNRAS* 428.4 (Feb. 2013), pp. 3409–3424. DOI: 10.1093/mnras/sts281. arXiv: 1203.0248 [astro-ph.CO].

[2] Aragón-Calvo et al. "The multiscale morphology filter: identifying and extracting spatial patterns in the galaxy distribution". In: 474.1 (Oct. 2007), pp. 315–338. DOI: 10.1051/0004-6361:20077880. arXiv: 0705.2072 [astro-ph].

[3] Jeremy Bailin and Matthias Steinmetz. "Internal and External Alignment of the Shapes and Angular Momenta of ΛCDM Halos". In: *ApJ* 627.2 (July 2005), pp. 647–665. DOI: 10.1086/430397. arXiv: astro-ph/0408163 [astro-ph].

[4] C. Bradford Barber, David P. Dobkin, and Hannu Huhdanpaa. "The Quickhull algorithm for convex hulls". In: *ACM TRANSACTIONS ON MATHEMATICAL SOFTWARE* 22.4 (1996), pp. 469–483.

[5] Josh Barnes and Piet Hut. "A hierarchical O(N log N) force-calculation algorithm". In: 324.6096 (Dec. 1986), pp. 446–449. DOI: 10.1038/324446a0.

[6] and Gonzalez-Perez Baugh et al. "Galaxy formation in the Planck Millennium: the atomic hydrogen content of dark matter halos". In: *MNRAS* 483.4 (Mar. 2019), pp. 4922–4937. DOI: 10.1093/mnras/sty3427. arXiv: 1808.08276 [astro-ph.GA].

[7] Adrian E. Bayer et al. "Detecting neutrino mass by combining matter clustering, halos, and voids". In: *arXiv e-prints*, arXiv:2102.05049 (Feb. 2021), arXiv:2102.05049. arXiv: 2102.05049 [astro-ph.CO].

[8] Peter S. Behroozi, Risa H. Wechsler, and Hao-Yi Wu. "The ROCKSTAR Phase-space Temporal Halo Finder and the Velocity Offsets of Cluster Cores". In: *ApJ* 762.2, 109 (Jan. 2013), p. 109. DOI: 10.1088/0004-637X/762/2/109. arXiv: 1110.4372 [astro-ph.CO].

[9] Bernardeau and van de Weygaert. "A new method for accurate estimation of velocity field statistics". In: *MNRAS* 279 (Mar. 1996), p. 693. DOI: 10.1093/mnras/279.2.693. arXiv: astro-ph/9508125 [astro-ph].

[10] E. Bertschinger. "Self-similar secondary infall and accretion in an Einstein-de Sitter universe". In: *ApJS* 58 (May 1985), pp. 39–65. DOI: 10.1086/191028.

[11] E. Bertschinger. "The self-similar evolution of holes in an Einstein-de Sitter universe". In: *ApJS* 58 (May 1985), pp. 1–37. DOI: 10.1086/191027.

[12] B. Beygu et al. "The void galaxy survey: photometry, structure and identity of void galaxies". In: *MNRAS* 464.1 (Jan. 2017), pp. 666–679. DOI: 10.1093/mnras/stw2362. arXiv: 1609.04920 [astro-ph.GA].

[13] G. R. Blumenthal et al. "The Largest Possible Voids". In: *ApJ* 388 (Apr. 1992), p. 234. DOI: 10.1086/171147.

[14] J. R. Bond et al. "Excursion Set Mass Functions for Hierarchical Gaussian Fluctuations". In: *ApJ* 379 (Oct. 1991), p. 440. DOI: 10.1086/170520.

[15] E. G. Patrick Bos et al. "The darkness that shaped the void: dark energy and cosmic voids". In: *MNRAS* 426.1 (Oct. 2012), pp. 440–461. DOI: 10.1111/j.1365-2966.2012.21478.x. arXiv: 1205.4238 [astro-ph.CO].

[16] Boylan-Kolchin et al. "Resolving cosmic structure formation with the Millennium-II Simulation". In: *MNRAS* 398.3 (Sept. 2009), pp. 1150–1164. DOI: 10.1111/j.1365-2966.2009.15191.x. arXiv: 0903.3041 [astro-ph.CO].

[17] E. Branchini et al. "A non-parametric model for the cosmic velocity field". In: *MNRAS* 308.1 (Sept. 1999), pp. 1–28. DOI: 10.1046/j.1365-8711.1999.02514.x. arXiv: astro-ph/9901366 [astro-ph].

[18] J. S. Bullock et al. "A Universal Angular Momentum Profile for Galactic Halos". In: *ApJ* 555.1 (July 2001), pp. 240–257. DOI: 10.1086/321477. arXiv: astro-ph/0011001 [astro-ph].

[19] Cautun, Cai, and Frenk. "The view from the boundary: a new void stacking method". In: *MNRAS* 457.3 (Apr. 2016), pp. 2540–2553. DOI: 10.1093/mnras/stw154. arXiv: 1509.00010 [astro-ph.CO].

[20] Cautun and van de Weygaert. "The DTFE public software: The Delaunay Tessellation Field Estimator code". In: *arXiv e-prints*, arXiv:1105.0370 (May 2011), arXiv:1105.0370. arXiv: 1105.0370 [astro-ph.IM].

[21] Cautun, van de Weygaert, and Jones. "NEXUS: tracing the cosmic web connection". In: *MNRAS* 429.2 (Feb. 2013), pp. 1286–1308. DOI: 10.1093/mnras/sts416. arXiv: 1209.2043 [astro-ph.CO].

[22] Cautun, van de Weygaert, Jones, and Frenk. "Evolution of the cosmic web". In: *MNRAS* 441.4 (July 2014), pp. 2923–2973. DOI: 10.1093/mnras/stu768. arXiv: 1401.7866 [astro-ph.CO].

[23] G. Chincarini and H. J. Rood. "Size of the Coma cluster". In: 257.5524 (Sept. 1975), pp. 294–295. DOI: 10.1038/257294a0.

[24] Colberg, Frazer Pearce, et al. "The Aspen-Amsterdam void finder comparison project". In: *MNRAS* 387.2 (June 2008), pp. 933–944. DOI: 10.1111/j.1365-2966.2008.13307.x. arXiv: 0803.0918 [astro-ph].

[25] Colberg, Sheth, et al. "Voids in a ΛCDM universe". In: *MNRAS* 360.1 (June 2005), pp. 216–226. DOI: 10.1111/j.1365-2966.2005.09064.x. arXiv: astro-ph/0409162 [astro-ph].

[26] Shaun Cole and Cedric Lacey. "The structure of dark matter haloes in hierarchical clustering models". In: *MNRAS* 281 (July 1996), p. 716. DOI: 10.1093/mnras/281.2.716. arXiv: astro-ph/9510147 [astro-ph].

[27] Matthew Colless et al. "The 2dF Galaxy Redshift Survey: Final Data Release". In: *arXiv e-prints*, astro-ph/0306581 (June 2003), astro–ph/0306581. arXiv: astro-ph/0306581 [astro-ph].

[28] V. de Lapparent, Geller, and J. P. Huchra. "A Slice of the Universe". In: *ApJL* 302 (Mar. 1986), p. L1. DOI: 10.1086/184625.

[29] Avishai Dekel. "Dynamics of Cosmic Flows". In: 32 (Jan. 1994), pp. 371–418. DOI: 10.1146/annurev.aa.32.090194.002103. arXiv: astro-ph/9401022 [astro-ph].

[30] Avishai Dekel and Martin J. Rees. "Omega from Velocities in Voids". In: *ApJL* 422 (Feb. 1994), p. L1. DOI: 10.1086/187197. arXiv: astro-ph/9308029 [astro-ph].

[31] DESI Collaboration et al. "The DESI Experiment Part I: Science,Targeting, and Survey Design". In: *arXiv e-prints*, arXiv:1611.00036 (Oct. 2016), arXiv:1611.00036. arXiv: 1611.00036 [astro-ph.IM].

[32] Jürg Diemand, Michael Kuhlen, and Piero Madau. "Early Supersymmetric Cold Dark Matter Substructure". In: *ApJ* 649.1 (Sept. 2006), pp. 1–13. DOI: 10.1086/506377. arXiv: astro-ph/0603250 [astro-ph].

[33] Dressler. "Galaxy morphology in rich clusters: implications for the formation and evolution of galaxies." In: *ApJ* 236 (Mar. 1980), pp. 351–365. DOI: 10.1086/157753.

[34] G. Efstathiou and Jones. "The rotation of galaxies: numerical investigations of the tidal torque theory." In: *MNRAS* 186 (Jan. 1979), pp. 133–144. DOI: 10.1093/mnras/186.2.133.

[35] Efstathiou et al. "Numerical techniques for large cosmological N-body simulations". In: *ApJS* 57 (Feb. 1985), pp. 241–260. DOI: 10.1086/191003.

[36] J. Einasto, M. Joeveer, and E. Saar. "Superclusters and galaxy formation". In: 283.5742 (Jan. 1980), pp. 47–48. DOI: 10.1038/283047a0.

[37] S. M. Faber and David Burstein. "Motions of galaxies in the neighborhood of the Local Group." In: *Large-Scale Motions in the Universe: A Vatican study Week*. Ed. by Vera C. Rubin and George V. Coyne. 1988, pp. 115–167.

[38] Punyakoti Ganeshaiah Veena et al. "The Cosmic Ballet II: spin alignment of galaxies and haloes with large-scale filaments in the EAGLE simulation". In: *MNRAS* 487.2 (Aug. 2019), pp. 1607–1625. DOI: 10.1093/mnras/stz1343. arXiv: 1903.06716 [astro-ph.CO].

[39] Ganeshaiah Veena et al. "The Cosmic Ballet: spin and shape alignments of haloes in the cosmic web". In: *MNRAS* 481.1 (Nov. 2018), pp. 414–438. DOI: 10.1093/mnras/sty2270. arXiv: 1805.00033 [astro-ph.CO].

[40] David M. Goldberg and Michael S. Vogeley. "Simulating Voids". In: *ApJ* 605.1 (Apr. 2004), pp. 1–6. DOI: 10.1086/382143. arXiv: astro-ph/0307191 [astro-ph].

[41] S. A. Gregory and L. A. Thompson. "The Coma/A1367 supercluster and its environs." In: *ApJ* 222 (June 1978), pp. 784–799. DOI: 10.1086/156198.

[42] Norman A. Grogin and Geller. "An Imaging and Spectroscopic Survey of Galaxies within Prominent Nearby Voids. I. The Sample and Luminosity Distribution". In: 118.6 (Dec. 1999), pp. 2561–2580. DOI: 10.1086/301126. arXiv: astro-ph/9910073 [astro-ph].

[43] Norman A. Grogin and Geller. "An Imaging and Spectroscopic Survey of Galaxies within Prominent Nearby Voids. II. Morphologies, Star Formation, and Faint Companions". In: 119.1 (Jan. 2000), pp. 32–43. DOI: 10.1086/301179. arXiv: astro-ph/9910096 [astro-ph].

[44] Gunn and Gott. "On the Infall of Matter Into Clusters of Galaxies and Some Effects on Their Evolution". In: *ApJ* 176 (Aug. 1972), p. 1. DOI: 10.1086/151605.

[45] Mélanie Habouzit et al. "Properties of simulated galaxies and supermassive black holes in cosmic voids". In: *MNRAS* 493.1 (Mar. 2020), pp. 899–921. DOI: 10.1093/mnras/staa219. arXiv: 1912.06662 [astro-ph.GA].

[46] Oliver Hahn et al. "The evolution of dark matter halo properties in clusters, filaments, sheets and voids". In: *MNRAS* 381.1 (Oct. 2007), pp. 41–51. DOI: 10.1111/j.1365-2966.2007.12249.x. arXiv: 0704.2595 [astro-ph].

[47] Alan Heavens and John Peacock. "Tidal torques and local density maxima". In: *MNRAS* 232 (May 1988), pp. 339–360. DOI: 10.1093/mnras/232.2.339.

[48] Hellwing, Cautun, et al. "Caught in the cosmic web: Environmental effect on halo concentrations, shape, and spin". In: 103.6, 063517 (Mar. 2021), p. 063517. DOI: 10.1103/PhysRevD.103.063517. arXiv: 2011.08840 [astro-ph.CO].

[49] Hellwing, Frenk, et al. "The Copernicus Complexio: a high-resolution view of the small-scale Universe". In: *MNRAS* 457.4 (Apr. 2016), pp. 3492–3509. DOI: 10.1093/mnras/stw214. arXiv: 1505.06436 [astro-ph.CO].

[50] Hoffman and J. Shaham. "On the origin of the voids in the galaxy distribution". In: *ApJL* 262 (Nov. 1982), pp. L23–L26. DOI: 10.1086/183904.

[51] Erik Holmberg. "On the Clustering Tendencies among the Nebulae. II. a Study of Encounters Between Laboratory Models of Stellar Systems by a New Integration Procedure." In: *ApJ* 94 (Nov. 1941), p. 385. DOI: 10.1086/144344.

[52] Hoyle. "The Origin of the Rotations of the Galaxies". In: *Problems of Cosmical Aerodynamics*. Jan. 1951, p. 195.

[53] Hoyle and Michael S. Vogeley. "Voids in the Two-Degree Field Galaxy Redshift Survey". In: *ApJ* 607.2 (June 2004), pp. 751–764. DOI: 10.1086/386279. arXiv: astro-ph/0312533 [astro-ph].

[54] Edwin Hubble. "A Relation between Distance and Radial Velocity among Extra-Galactic Nebulae". In: *Proceedings of the National Academy of Science* 15.3 (Mar. 1929), pp. 168–173. DOI: 10.1073/pnas.15.3.168.

[55] V. Icke. "Voids and filaments". In: *MNRAS* 206 (Jan. 1984), 1P–3P. DOI: 10.1093/mnras/206.1.1P.

[56] N. Jarosik et al. "Seven-year Wilkinson Microwave Anisotropy Probe (WMAP) Observations: Sky Maps, Systematic Errors, and Basic Results". In: *ApJS* 192.2, 14 (Feb. 2011), p. 14. DOI: 10.1088/0067-0049/192/2/14. arXiv: 1001.4744 [astro-ph.CO].

[57] S. F. Kasun and A. E. Evrard. "Shapes and Alignments of Galaxy Cluster Halos". In: *ApJ* 629.2 (Aug. 2005), pp. 781–790. DOI: 10.1086/430811. arXiv: astro-ph/0408056 [astro-ph].

[58] Kirshner et al. "A million cubic megaparsec void in Bootes ?" In: *ApJL* 248 (Sept. 1981), pp. L57–L60. DOI: 10.1086/183623.

[59] Kirshner et al. "A Survey of the Bootes Void". In: *ApJ* 314 (Mar. 1987), p. 493. DOI: 10.1086/165080.

[60] Anatoly Klypin et al. "Galaxies in N-Body Simulations: Overcoming the Overmerging Problem". In: *ApJ* 516.2 (May 1999), pp. 530–551. DOI: 10.1086/307122. arXiv: astro-ph/9708191 [astro-ph].

[61] Alexander Knebe et al. "Haloes gone MAD: The Halo-Finder Comparison Project". In: *MNRAS* 415.3 (Aug. 2011), pp. 2293–2318. DOI: 10.1111/j.1365-2966.2011.18858.x. arXiv: 1104.0949 [astro-ph.CO].

[62] Steffen R. Knollmann and Alexander Knebe. "AHF: Amiga's Halo Finder". In: *ApJS* 182.2 (June 2009), pp. 608–624. DOI: 10.1088/0067-0049/182/2/608. arXiv: 0904.3662 [astro-ph.CO].

[63] Kreckel, Platen, M. A. Aragón-Calvo, et al. "Only the Lonely: H I Imaging of Void Galaxies". In: 141.1, 4 (Jan. 2011), p. 4. DOI: 10.1088/0004-6256/141/1/4. arXiv: 1008.4616 [astro-ph.CO].

[64] Kreckel, Platen, Aragón-Calvo, et al. "The Void Galaxy Survey: Optical Properties and H I Morphology and Kinematics". In: 144.1, 16 (July 2012), p. 16. DOI: 10.1088/0004-6256/144/1/16. arXiv: 1204.5185 [astro-ph.CO].

[65] Christina D. Kreisch et al. "The GIGANTES dataset: precision cosmology from voids in the machine learning era". In: *arXiv e-prints*, arXiv:2107.02304 (July 2021), arXiv:2107.02304. arXiv: 2107.02304 [astro-ph.CO].

[66] Lavaux and Wandelt. "Precision Cosmography with Stacked Voids". In: *ApJ* 754.2, 109 (Aug. 2012), p. 109. DOI: 10.1088/0004-637X/754/2/109. arXiv: 1110.0345 [astro-ph.CO].

[67] M. Maciejewski et al. "Phase-space structures - II. Hierarchical Structure Finder". In: *MNRAS* 396.3 (July 2009), pp. 1329–1348. DOI: 10.1111/j.1365-2966.2009.14825.x. arXiv: 0812.0288 [astro-ph].

[68] Elena Massara et al. "Voids in massive neutrino cosmologies". In: 2015.11, 018 (Nov. 2015), p. 018. DOI: 10.1088/1475-7516/2015/11/018. arXiv: 1506.03088 [astro-ph.CO].

[69] Dries Matthijs. "A hierarchy of voids". MA thesis. the Netherlands: Rijksuniversiteit Groningen, 2003.

[70] Ofer Metuki, Noam I. Libeskind, and Hoffman. "The abundance and environment of dark matter haloes". In: *MNRAS* 460.1 (July 2016), pp. 297–303. DOI: 10.1093/mnras/stw979. arXiv: 1606.01514 [astro-ph.GA].

[71] Houjun Mo, Frank C. van den Bosch, and White. *Galaxy Formation and Evolution*. 2010.

[72] Nadathur. "Testing cosmology with a catalogue of voids in the BOSS galaxy surveys". In: *MNRAS* 461.1 (Sept. 2016), pp. 358–370. DOI: 10.1093/mnras/stw1340. arXiv: 1602.04752 [astro-ph.CO].

[73] Nadathur and Hotchkiss. "The nature of voids - I. Watershed void finders and their connection with theoretical models". In: *MNRAS* 454.2 (Dec. 2015), pp. 2228–2241. DOI: 10.1093/mnras/stv2131. arXiv: 1504.06510 [astro-ph.CO].

[74] Navarro, Frenk, and White. "The Structure of Cold Dark Matter Halos". In: *ApJ* 462 (May 1996), p. 563. DOI: 10.1086/177173. arXiv: astro-ph/9508025 [astro-ph].

[75] Mark C. Neyrinck. "ZOBOV: a parameter-free void-finding algorithm". In: *MNRAS* 386.4 (June 2008), pp. 2101–2109. DOI: 10.1111/j.1365-2966.2008.13180.x. arXiv: 0712.3049 [astro-ph].

[76] Oemler. "The Systematic Properties of Clusters of Galaxies. Photometry of 15 Clusters". In: *ApJ* 194 (Nov. 1974), pp. 1–20. DOI: 10.1086/153216.

[77] Danny C. Pan et al. "Cosmic voids in Sloan Digital Sky Survey Data Release 7". In: *MNRAS* 421.2 (Apr. 2012), pp. 926–934. DOI: 10.1111/j.1365-2966.2011.20197.x. arXiv: 1103.4156 [astro-ph.CO].

[78] Divya Pandey, Kanak Saha, and Ananta C. Pradhan. "The Ultraviolet Deep Imaging Survey of Galaxies in the Bootes Void I: catalog, color-magnitude relations and star formation". In: *arXiv e-prints*, arXiv:2107.01774 (July 2021), arXiv:2107.01774. arXiv: 2107.01774 [astro-ph.GA].

[79] Daeseong Park and Jounghun Lee. "Void Ellipticity Distribution as a Probe of Cosmology". In: 98.8, 081301 (Feb. 2007), p. 081301. DOI: 10.1103/PhysRevLett.98.081301. arXiv: astro-ph/0610520 [astro-ph].

[80] P. J. E. Peebles. "Origin of the Angular Momentum of Galaxies". In: *ApJ* 155 (Feb. 1969), p. 393. DOI: 10.1086/149876.

[81] P. J. E. Peebles. *The large-scale structure of the universe*. 1980.

[82] P. J. E. Peebles. "The Void Phenomenon". In: *ApJ* 557.2 (Aug. 2001), pp. 495–504. DOI: 10.1086/322254. arXiv: astro-ph/0101127 [astro-ph].

[83] A. A. Penzias and R. W. Wilson. "A Measurement of Excess Antenna Temperature at 4080 Mc/s." In: *ApJ* 142 (July 1965), pp. 419–421. DOI: 10.1086/148307.

[84] Planck Collaboration et al. "Planck 2018 results. VI. Cosmological parameters". In: 641, A6 (Sept. 2020), A6. DOI: 10.1051/0004-6361/201833910. arXiv: 1807.06209 [astro-ph.CO].

[85] S. Planelles and V. Quilis. "ASOHF: a new adaptive spherical overdensity halo finder". In: 519, A94 (Sept. 2010), A94. DOI: 10.1051/0004-6361/201014214. arXiv: 1006.3205 [astro-ph.CO].

[86] Platen. "A void perspective of the Cosmic Web". PhD thesis. University of Groningen, Nov. 2009.

[87] Platen, van de Weygaert, and Jones. "A cosmic watershed: the WVF void detection technique". In: *MNRAS* 380.2 (Sept. 2007), pp. 551–570. DOI: 10.1111/j.1365-2966.2007.12125.x. arXiv: 0706.2788 [astro-ph].

[88] Platen, van de Weygaert, and Jones. "Alignment of voids in the cosmic web". In: *MNRAS* 387.1 (June 2008), pp. 128–136. DOI: 10.1111/j.1365-2966.2008.13019.x. arXiv: 0711.2480 [astro-ph].

[89] Platen, van de Weygaert, Jones, et al. "Structural analysis of the SDSS Cosmic Web - I. Non-linear density field reconstructions". In: *MNRAS* 416.4 (Oct. 2011), pp. 2494–2526. DOI: 10.1111/j.1365-2966.2011.18905.x. arXiv: 1107.1488 [astro-ph.CO].

[90] Giorgia Pollina et al. "Cosmic voids in coupled dark energy cosmologies: the impact of halo bias". In: *MNRAS* 455.3 (Jan. 2016), pp. 3075–3085. DOI: 10.1093/mnras/stv2503. arXiv: 1506.08831 [astro-ph.CO].

[91] William H. Press and Schechter. "Formation of Galaxies and Clusters of Galaxies by Self-Similar Gravitational Condensation". In: *ApJ* 187 (Feb. 1974), pp. 425–438. DOI: 10.1086/152650.

[92] Eniko Regos and Geller. "The Evolution of Void-filled Cosmological Structures". In: *ApJ* 377 (Aug. 1991), p. 14. DOI: 10.1086/170332.

[93] E. Ricciardelli et al. "The star formation activity in cosmic voids". In: *MNRAS* 445.4 (Dec. 2014), pp. 4045–4054. DOI: 10.1093/mnras/stu2061. arXiv: 1410.0023 [astro-ph.GA].

[94] Brant Robertson et al. "A Merger-driven Scenario for Cosmological Disk Galaxy Formation". In: *ApJ* 645.2 (July 2006), pp. 986–1000. DOI: 10.1086/504412. arXiv: astro-ph/0503369 [astro-ph].

[95] Romano-Dıaz and van de Weygaert. "Delaunay Tessellation Field Estimator analysis of the PSCz local Universe: density field and cosmic flow". In: *MNRAS* 382.1 (Nov. 2007), pp. 2–28. DOI: 10.1111/j.1365-2966.2007.12190.x.

[96] Barbara S. Ryden and Adrian L. Melott. "Voids in Real Space and in Redshift Space". In: *ApJ* 470 (Oct. 1996), p. 160. DOI: 10.1086/177857. arXiv: astro-ph/9510108 [astro-ph].

[97] W. E. Schaap. "DTFE: the Delaunay Tessellation Field Estimator". PhD thesis. Kapteyn Astronomical Institute, Jan. 2007.

[98] W. E. Schaap and van de Weygaert. "Continuous fields and discrete samples: reconstruction through Delaunay tessellations". In: 363 (Nov. 2000), pp. L29–L32. arXiv: astro-ph/0011007 [astro-ph].

[99] Schechter. "An analytic expression for the luminosity function for galaxies." In: *ApJ* 203 (Jan. 1976), pp. 297–306. DOI: 10.1086/154079.

[100] Schechter. "Mass-to-light ratios for elliptical galaxies." In: 85 (July 1980), pp. 801–811. DOI: 10.1086/112742.

[101] Nico Schuster et al. "The bias of cosmic voids in the presence of massive neutrinos". In: 2019.12, 055 (Dec. 2019), p. 055. DOI: 10.1088/1475-7516/2019/12/055. arXiv: 1905.00436 [astro-ph.CO].

[102] Sergei Shandarin et al. "Shapes and sizes of voids in the Lambda cold dark matter universe: excursion set approach". In: *MNRAS* 367.4 (Apr. 2006), pp. 1629–1640. DOI: 10.1111/j.1365-2966.2006.10062.x. arXiv: astro-ph/0509858 [astro-ph].

[103] Sheth and van de Weygaert. "A hierarchy of voids: much ado about nothing". In: *MNRAS* 350.2 (May 2004), pp. 517–538. DOI: 10.1111/j.1365-2966.2004.07661.x. arXiv: astro-ph/0311260 [astro-ph].

[104] Springel. "The cosmological simulation code GADGET-2". In: *MNRAS* 364.4 (Dec. 2005), pp. 1105–1134. DOI: 10.1111/j.1365-2966.2005.09655.x. arXiv: astro-ph/0505010 [astro-ph].

[105] Springel, Pakmor, et al. "Simulating cosmic structure formation with the GADGET-4 code". In: *MNRAS* 506.2 (Sept. 2021), pp. 2871–2949. DOI: 10.1093/mnras/stab1855. arXiv: 2010.03567 [astro-ph.IM].

[106] V. Springel et al. "The Aquarius Project: the subhaloes of galactic haloes". In: *MNRAS* 391.4 (Dec. 2008), pp. 1685–1711. DOI: 10.1111/j.1365-2966.2008.14066.x. arXiv: 0809.0898 [astro-ph].

[107] Springel, White, Jenkins, et al. "Simulations of the formation, evolution and clustering of galaxies and quasars". In: 435.7042 (June 2005), pp. 629–636. DOI: 10.1038/nature03597. arXiv: astro-ph/0504097 [astro-ph].

[108] Springel, White, Tormen, et al. "Populating a cluster of galaxies - I. Results at [formmu2]z=0". In: *MNRAS* 328.3 (Dec. 2001), pp. 726–750. DOI: 10.1046/j.1365-8711.2001.04912.x. arXiv: astro-ph/0012055 [astro-ph].

[109] Springel, Yoshida, and White. "GADGET: a code for collisionless and gasdynamical cosmological simulations". In: 6.2 (Apr. 2001), pp. 79–117. DOI: 10.1016/S1384-1076(01)00042-2. arXiv: astro-ph/0003162 [astro-ph].

[110] Sutter, Lavaux, Hamaus, et al. "VIDE: The Void IDentification and Examination toolkit". In: *Astronomy and Computing* 9 (Mar. 2015), pp. 1–9. DOI: 10.1016/j.ascom.2014.10.002. arXiv: 1406.1191 [astro-ph.CO].

[111] Sutter, Lavaux, Wandelt, et al. "A First Application of the Alcock-Paczynski Test to Stacked Cosmic Voids". In: *ApJ* 761.2, 187 (Dec. 2012), p. 187. DOI: 10.1088/0004-637X/761/2/187. arXiv: 1208.1058 [astro-ph.CO].

[112] P. M. Sutter et al. "A Public Void Catalog from the SDSS DR7 Galaxy Redshift Surveys Based on the Watershed Transform". In: *ApJ* 761.1, 44 (Dec. 2012), p. 44. DOI: 10.1088/0004-637X/761/1/44. arXiv: 1207.2524 [astro-ph.CO].

[113] Max Tegmark et al. "The Three-Dimensional Power Spectrum of Galaxies from the Sloan Digital Sky Survey". In: *ApJ* 606.2 (May 2004), pp. 702–740. DOI: 10.1086/382125. arXiv: astro-ph/0310725 [astro-ph].

[114] R. Brent Tully et al. "The Laniakea supercluster of galaxies". In: *Nature* 513.7516 (Sept. 2014), pp. 71–73. ISSN: 1476-4687. DOI: 10.1038/nature13674. URL: http://dx.doi.org/10.1038/nature13674.

[115] van de Weygaert. "Voids and the geometry of large scale structure". PhD thesis. -, Sept. 1991.

[116] van de Weygaert and Platen. "Cosmic Voids: Structure, Dynamics and Galaxies". In: *International Journal of Modern Physics Conference Series*. Vol. 1. International Journal of Modern Physics Conference Series. Jan. 2011, pp. 41–66. DOI: 10.1142/S2010194511000092. arXiv: 0912.2997 [astro-ph.CO].

[117] van de Weygaert and Schaap. "The Cosmic Web: Geometric Analysis". In: *Data Analysis in Cosmology*. Ed. by V. J. Martınez et al. Vol. 665. 2009, pp. 291–413. DOI: 10.1007/978-3-540-44767-2_11.

[118] van de Weygaert and E. van Kampen. "Voids in Gravitational Instability Scenarios - Part One - Global Density and Velocity Fields in an Einstein - De-Sitter Universe". In: *MNRAS* 263 (July 1993), p. 481. DOI: 10.1093/mnras/263.2.481.

[119] Giovanni Verza et al. "The void size function in dynamical dark energy cosmologies". In: 2019.12, 040 (Dec. 2019), p. 040. DOI: 10.1088/1475-7516/2019/12/040. arXiv: 1906.00409 [astro-ph.CO].

[120] Francisco Villaescusa-Navarro et al. "The Quijote Simulations". In: *ApJS* 250.1, 2 (Sept. 2020), p. 2. DOI: 10.3847/1538-4365/ab9d82. arXiv: 1909.05273 [astro-ph.CO].

[121] Villaescusa-Navarro et al. "Neutrino signatures on the high-transmission regions of the Lyman α forest". In: *MNRAS* 431.4 (June 2013), pp. 3670–3677. DOI: 10.1093/mnras/stt452. arXiv: 1106.2543 [astro-ph.CO].

[122] Mark Vogelsberger et al. "Introducing the Illustris Project: simulating the coevolution of dark and visible matter in the Universe". In: *MNRAS* 444.2 (Oct. 2014), pp. 1518–1547. DOI: 10.1093/mnras/stu1536. arXiv: 1405.2921 [astro-ph.CO].

[123] Michael S. Warren et al. "Dark Halos Formed via Dissipationless Collapse. I. Shapes and Alignment of Angular Momentum". In: *ApJ* 399 (Nov. 1992), p. 405. DOI: 10.1086/171937.

[124] Wojtak, Devon Powell, and Tom Abel. "Voids in cosmological simulations over cosmic time". In: *MNRAS* 458.4 (June 2016), pp. 4431–4442. DOI: 10.1093/mnras/stw615. arXiv: 1602.08541 [astro-ph.CO].

[125] Y. B. Zel'Dovich. "Reprint of 1970A&A.....5...84Z. Gravitational instability: an approximate theory for large density perturbations." In: 500 (Mar. 1970), pp. 13–18.